Balanced Correlation Receivers with Applications to Precision Radiometry

David Douglas Bordenave
Simmershofen, Germany; Camp Zama, Japan

B.S. Physics; Astronomy, University of Washington, 2016
M.S. Astronomy, University of Virginia, 2018

A Dissertation Presented to the
Graduate Faculty of the
University of Virginia
in Candidacy for the Degree of
Doctor of Philosophy

Department of Astronomy

University of Virginia
May 2024

Committee Members:
Richard F. Bradley
Bradley R. Johnson
Remy Indebetouw
Arthur W. Lichtenberger
Jack Singal

© Copyright by
David Douglas Bordenave
All rights reserved
April 23, 2024

Abstract

This thesis is focused on the development of novel polarimetric techniques and radio receiver designs for precision radiometry applied to 21 cm cosmology and mapping of the radio synchrotron background. The work is organized around two overarching projects, the cosmic twilight polarimeter and the GBT 310 MHz Absolute Mapping project. The astrophysical context for these experiments will be introduced in Chapter 1, where I present a brief history of the universe, including the formation of the first stars and galaxies, the nature of the low-frequency radio sky, and the basics of radio receivers.

In Chapter 2, I describe experimental work on the dynamically induced polarization effect initially proposed by my predecessor, Bang Nhan. This polarimetric approach is intended to reduce the beam-weighted foreground degeneracy typical in global 21 cm experiments by using the polarization leakage of the antenna to provide extra information on the anisotropic component of the sky. I provide a mathematical description of the antenna polarization leakage and associated dynamically induced polarization using the Mueller matrix representation, which intuitively shows how the instrument responds to arbitrarily polarized light from areas of the sky. I created a series of observation simulations using antenna beam models and the all-sky Haslam map, including atmospheric propagation effects and physical perturbations to the system. These simulations were then compared with experimental data provided by a repurposed PAPER antenna and receiver system that I deployed at Green Bank Observatory from fall 2019 to spring 2020. These observations qualitatively agree with simulations, but large deviations exist that may suggest missing contributions from sky polarization, propagation or instrumental effects.

In Chapter 3, I present the theory of operation for a novel type of radiometer, a Balanced Correlation Receiver (BCR), that virtually eliminates all measurement offset biases and gain instability ($1/f$ noise). The BCR accomplishes this through a unique digital synthesis method for forming the antenna beam directly from cross-correlations between the balanced outputs of the feed, thereby avoiding any directly shared circuitry between the feed points of the antenna and the receiver (e.g., baluns, transmission lines, power splitters and hybrids) that could introduce common-mode noise. I derive how different dipole beams can be formed from combinations of auto and cross-correlations of redundant-in-polarization e-field probes (e.g., the two monopole arms of a dipole). Additionally, I extend this analysis to the cross-dipole and apply digital polarization synthesis methods to derive the full-stokes polarization response and sensitivity for a BCR and limitations thereof. This approach is essential for the planned 310 MHz Sky Map and is the theoretical basis of the GBT310 instrument in Chapter 4.

In Chapter 4, I motivate the need for a new low-frequency sky map with absolute, zero-level calibration as the primary goal and which requires the Green Bank Telescope and a custom-built receiver. I present the scientific utility of such a new map, planned mapping strategy for the initially awarded NSF grant (PI – Jack Singal) and observational requirements for the custom instrument, the GBT 310 MHz receiver that employs the balanced correlation architecture from Chapter 3. The instrument development for the GBT310 includes the design, construction, lab testing, calibration and field commissioning of all critical sub-systems: the feed, frontend receiver module, data acquisition, monitoring and control, and system software. Finally, I present current results from the ground commission and testing of the GBT310 in preparation for first-light on the GBT.

Finally, Chapter 6 provides a summary of the key results and related future work. Additionally, the appendices contain detailed information about the design and specification of GBT310 components.

Acknowledgements

I couldn't have made it this far without the support of my family, friends, mentors, and colleagues.

First, to my parents who encouraged my curiosity and who both figuratively and literally gave me the tools to explore the unknown.

To Rich Bradley – Thanks for guiding me through my journey of learning the art and science of building instruments. Also, for being patient with me as I was reinventing the wheel(s) or getting stuck in the weeds.

To my fellow research colleagues – Bang and Krishna, thanks for all the help and encouragement throughout the years.

To the NRAO/CDL staff – Pat, Tod, Art, Greg, and everyone at the machine shop. Thanks for letting me bother you with questions, fabricating parts for me, and teaching me valuable practical skills.

To the GBO staff – Steve, Bob, Laura, Jonah, JD, Ray, and many others that assisted me in testing the GBT310 and carrying the feed around.

To the NRAO NRDZ/ASM Team – Chris, Kevin, Randy, Bert, thanks for your understanding and giving me the time I needed to finish my research. Also, for introducing me to new and exciting technical challenges to think about!

To past mentors – Michiel Brentjens and Richard Fallows, thanks for inducting me to the Department of Creative Telescope Abuse (I really didn't mean to break LOFAR that one time ...)

Finally, to all my friends and fellow grad students – I won't even attempt to list everyone for fear of accidentally forgetting a name. Thanks for all the good times, help and support over the past several years.

Table of Contents

List of Figures

List of Tables

Chapter 1

Introduction

"The story so far:
In the beginning the Universe was
created. This has made a lot of
people very angry and been widely
regarded as a bad move."

Douglas Adams, The Restaurant at
the End of the Universe

1.1 Cosmic Origins

About 13.8 billion years ago, the Universe emerged from an extremely hot and dense state, the so-called Big Bang. Immediately following this event, the infant Universe began to rapidly expand, cooling down in the process. During this period, critical milestones and phase transitions occurred that established the physical properties of our observable Universe. Within mere fractions of a second, the Universe cooled sufficiently for neutrons and protons to condense out of the soup of quarks and gluons (elementary particles). Over the next 10 seconds to 20 minutes, the remaining "light elements" were produced through nuclear fusion, forming ^{4}He, D, ^{3}He and ^{7}Li (in decreasing order of abundance), in a process referred to as *Big Bang Nucleosynthesis* (Coc & Vangioni, 2017). The Universe at this point was a fully ionized plasma of mostly hydrogen and helium, optically opaque to an observer due to the strong coupling of photons to matter via Thomson Scattering off free electrons.

It would take another 380,000 years after the Big Bang for the Universe to be sufficiently cool and expand such that the ions and electrons combined to form neutral atoms, the Epoch of Recombination. At this point, photons decoupled from matter, and left behind an electrically neutral and optically transparent Universe. The photons were emitted from this "surface of last scattering" with $T_\gamma \approx 3000$ K and are what we now observe as the 2.726 K *Cosmic Microwave Background* (CMB; Planck Collaboration et al. (2016)). In the fading afterglow of the CMB, large-scale structures began to form due to gravitational collapse, seeded by small density perturbations imparted during inflation at the earliest moments of the Big Bang. However, it would take another few 100s of millions of years for the primordial matter to cool and condense sufficiently such that the first stars and galaxies could form, leaving the Universe in a period known as the *Dark Ages*.

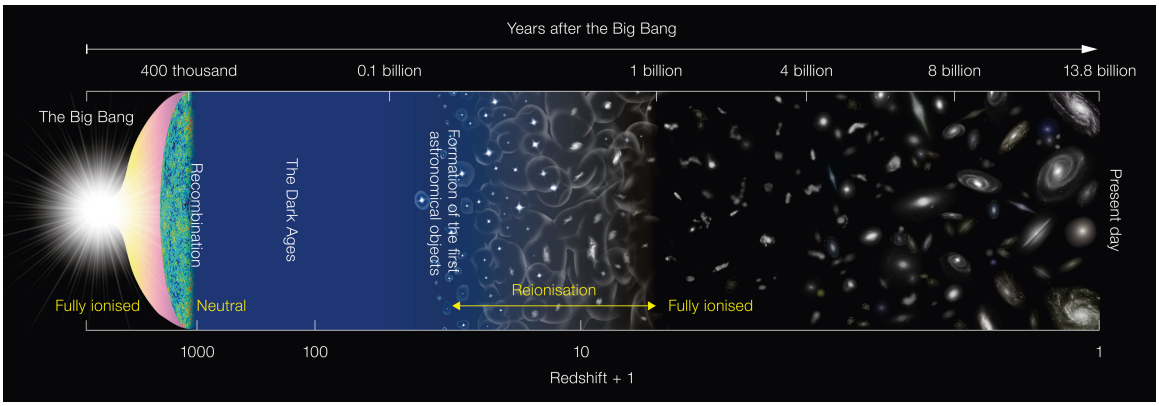

Figure 1.1: A summarized history of the Universe from the Big Bang to the present day (credit: NAOJ)

1.2 The First Stars and Galaxies

During the cosmic Dark Ages, the relatively featureless early Universe began to fragment and collapse into the large-scale structures we now observe as the Cosmic Web. According to the current leading cosmological model, Λ-CDM, which includes the contribution of Dark Energy (Λ) and *cold dark matter* (CDM), the evolution of the Universe during this era was then dominated by matter and gravity. Numerical simulations and observations have shown that the primordial medium, then composed of mostly hydrogen and helium, concentrated first into sheets, then filaments, and

eventually into dense clumps within the filaments. Within these clumps formed the first protogalaxies, the initial building blocks of the galaxies we observe today, and in them the first stars (also known as population III). The life and eventual death of these first luminous objects started the process that enriched the Universe with heavy elements and the eventual reionization of the *intergalactic medium* (IGM). However, the how and when of this first round of star formation are poorly understood since the initial conditions are vastly different from those we can currently observe.

The Dark Ages are difficult to observe because of a lack of visible sources, which was due to the enormous optical depth (or opacity) for the high-energy[1] optical spectral lines associated with stellar activity (e.g., Lyman-α). This optical depth was due to the absorption by neutral atoms in the IGM. Instead, alternate methods have been proposed that indirectly study these objects by observing the thermal evolution of their environment (the IGM) using neutral atomic hydrogen (HI) as a tracer. HI is an essential fuel for star formation, but is also able to emit a signal itself, the 21 cm line. This spectral line is produced by the spin-flip (or hyperfine) transition due to a difference in energy between parallel and anti-parallel alignments of the quantum spin of the proton and electron (see Figure 1.2).

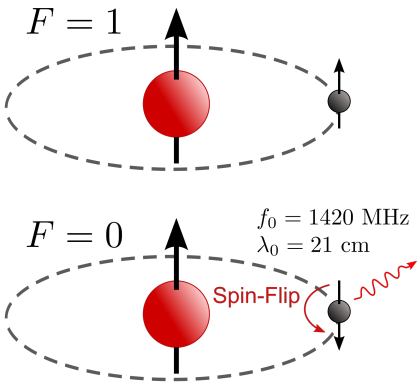

Figure 1.2: Shown is a cartoon of the hyperfine levels of neutral atomic hydrogen (or HI). When the atom is in the parallel (or higher-energy) state, it will spontaneously decay to the preferred anti-parallel (or lower-energy) state via the hyperfine transitions by emitting a photon with a wavelength of 21 cm.

The 21 cm hydrogen line is dependent on the physical state of the emitting gas, including the local temperature, density, and radiation field. Because it is also a weak and low-energy transition, it is minimally absorbed over the entirety of the observable universe (i.e., post-CMB), making it an ideal thermometer for studying the early low-temperature IGM. Additionally, because of the accelerating expansion

[1] In this context high-energy refers to ionizing radiation, including UV (Ultra-Violet) and higher energy light

of the Universe, electromagnetic radiation will appear to increase in wavelength the further away it is emitted from an observer, due to the relativistic Doppler effect or cosmological *redshift* ($\lambda_{obs}/\lambda_{emit} = (1+z)$). Thus, redshift provides a way to observe the Universe as a function of time, by measuring the 21 cm signal over a range of wavelengths.

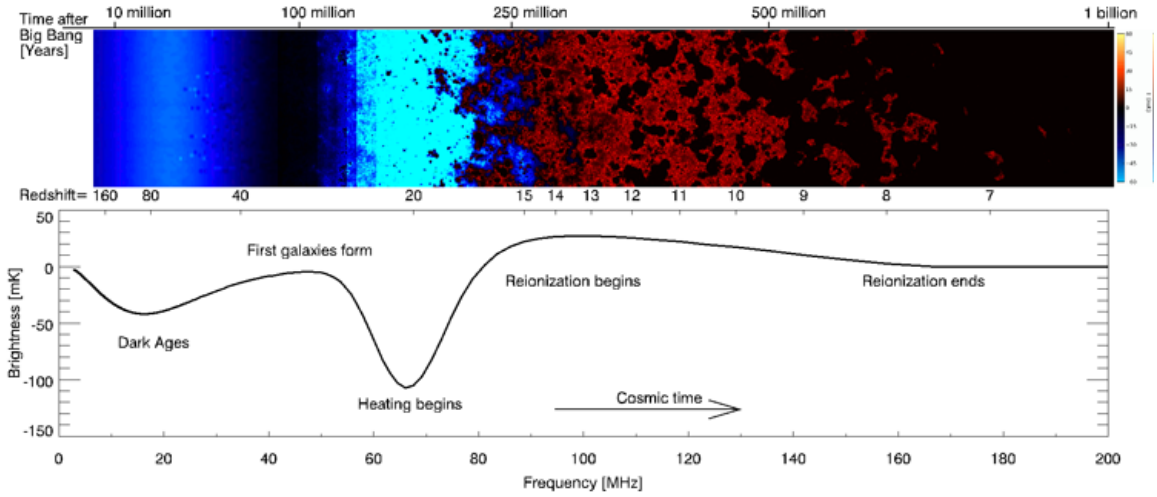

Figure 1.3: A cartoon of the spatial (top panel) and sky-averaged (bottom panel) 21-cm signal (credit: Pritchard, J. https://pritchardjr.github.io/research.html)

Figure 1.3 shows the characteristic absorption and emission features of the expected sky-averaged 21 cm signal relative to the CMB radiation. There are five critical turning points (or local extrema) in this signal that are dependent on the cosmological and physical processes that govern the growth of structure during the Dark Ages through to the eventual *Epoch of Reionization* (EoR) (Harker et al., 2012). The first local minimum occurs during the Dark Ages, when the collisional coupling of the 21 cm spin-temperature and kinetic temperature of the gas becomes inefficient and begins to heat up due to the formation of the first luminuous sources. This is followed by a peak that occurs when coupling of the 21 cm spin-temperature to the emitted Lyman-α (UV-light) from the first stars becomes effective via the Wouthuysen–Field effect (Wouthuysen, 1952). The subsequent cooling of the 21-cm signal is eventually halted at the following minimum during the Cosmic Dawn, when X-ray heating becomes effective due to the first accreting black holes. This transitions into the EoR, where a maximum in the 21 cm signal occurs when heating has saturated and then begins to decrease due to the expansion of the universe and reionization

reduces the availability of HI in the IGM. Finally, the last turining point occurs at the end of the EoR, when the 21 cm signal approaches zero as a majority of the HI in the IGM is reionized.

There are significant challenges for observing this signal in practice due to the 13 billion years of intervening structure formation between the signal and us, the observer. Because the signal was emitted during the first billion years of the Universe, the 21 cm (or 1420 MHz) spectral line signal would be observed as a smooth continuous spectra spanning 42-1.5 m (or $\sim 5 - 200$ MHz) due to redshifting. This frequency range coincides with the strong and highly anisotropic galactic synchrotron foreground (to be discussed in the following section: see Figure 1.4) that is 4-6 orders of magnitude greater than the expected global 21 cm amplitude of $T_{21cm} \sim 100$ mK. Furthermore, at these low-frequencies, instruments are typically limited to wide-beam dipole arrays (for power spectrum measurements) or single dipoles (for global sky-averaged measurements) that are sensitive to most of the sky. At these low-frequencies, radio observations are hindered by a wide variety of adverse effects including: ionospheric propagation effects, mutual coupling of the instrument to the environment, and contamination from anthropogenic Radio Frequency Interference (RFI) complicating the picture. To date, the 21 cm signal remains elusive, with recent experiments such as EDGES (Bowman et al., 2018), SARAS (Singh et al., 2018), HERA (DeBoer et al., 2017), and LOFAR (Mertens et al., 2020) that have yet to produce independently verifiable detections. This highlights the extreme precision, accuracy, and stability required to measure this faint signal, which places significant importance on understanding the instrument, calibrations, and modeling of all intervening physical processes that could influence the signal (see Chapter 2).

1.3 The Radio Continuum Sky

The first stars and protogalaxies, as well as the subsequent hierarchical growth of structure, produced the wealth of astrophysical objects, environments, and phenomena we can observe in the present day. With the exception of dark matter and dark energy, the contents of the Universe can be directly studied through the light[2] that these sources emit over the entire electromagnetic spectrum. Astronomers typically

[2]Now also including gravitational waves, and fundamental particles

study the intensity of light as a function of wavelength (or spectrum) to infer the local properties of astrophysical sources based on our understanding of the physical emission mechanisms. With each new spectral window, more information about the Universe can be uncovered.

The low-frequency radio continuum emission from the sky is one such spectral window (see Figure 1.4), and it provides a unique probe for understanding and constraining most Galactic and extragalactic phenomena that manifest in diffuse radio emission. There are three general mechanisms that produce continuum[3] emission in radio sources: thermal black-body radiation, thermal emission from ionized gas (or free-free emission), and synchrotron emission. Of particular interest is the radio synchrotron radiation, a form of non-thermal emission that is due to relativistic electrons gyrating in the weak interstellar magnetic fields, rather than from thermal excitiation (Pacholczyk (1970); Figure 1.5). Synchrotron radiation follows a steep power-law spectrum ($T_B \propto \nu^{-\beta}$ with $\beta \sim 2-3$) that increases towards lower frequencies, while in this limit the thermal radation follows the Reighly-Jeans Law ($T_B \propto \nu^2$) which has the opposite behavior. Thus, synchrotron radiation will generally dominate the total radio emission from astronomical sources compared to the thermal radiation. This makes synchrotron emission an ideal probe for studying cosmic-ray propagation (Orlando, 2018), magnetic field structure in the Galaxy (Sun et al., 2008), the composition of the interstellar medium (Nguyen et al., 2018), and the cosmic microwave background (Planck Collaboration et al., 2016). It is also useful for supernova and pulsar searches (Surnis et al., 2018), as part of multiwavelength studies of Galactic phenomena (Kogut et al., 2011), 21 cm cosmology (Bowman et al., 2018), and more.

Thus, large-area, absolutely calibrated, zero-level[4] maps of the diffuse low-frequency radio emission are vital to our understanding of not only Galactic but also many extragalactic and cosmological phenomena. However, the last full-sky, high-resolution, absolutely calibrated, zero-level radio map at MHz frequencies was produced in the 1980s (see Chapter 4).

[3]Producing a continuous spectrum over a range of wavelength rather than spectral lines

[4]Absolute and zero-level calibration refer to measurements taken on an absolute measurement scale rather than a differential or relative scale

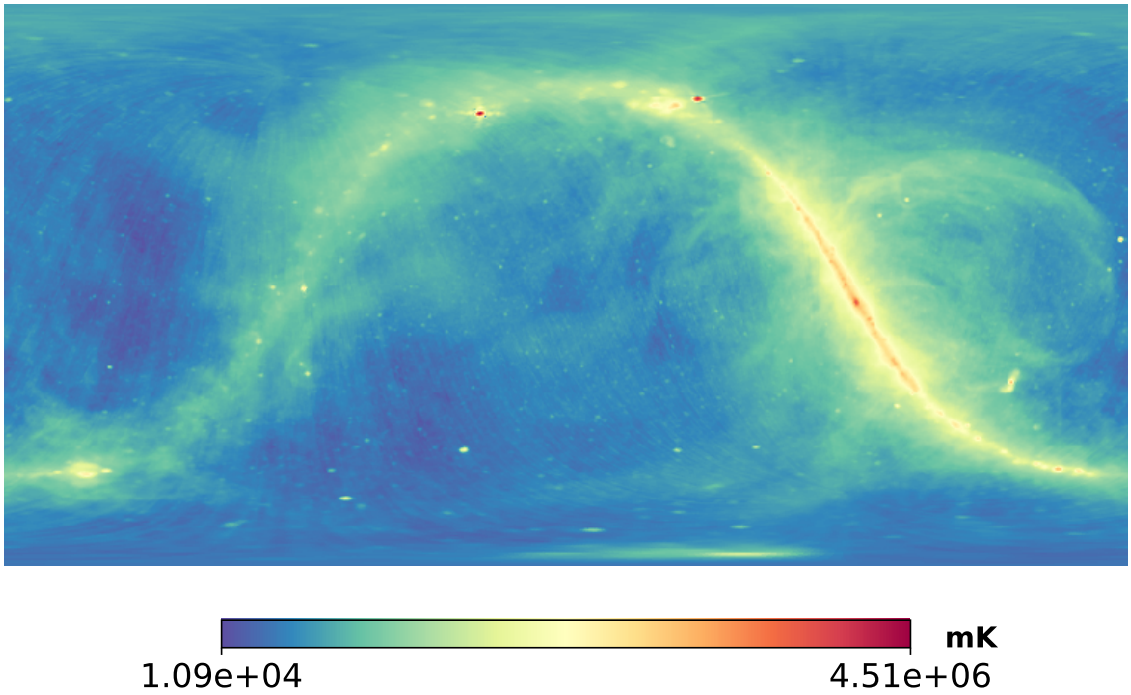

Figure 1.4: The Haslam 408 MHz Map in equatorial coordinates (Haslam et al., 1982).

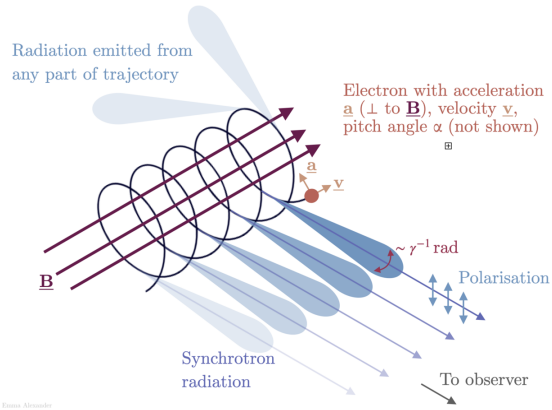

Figure 1.5: Cartoon of the Synchrotron radiation mechanism (credit: Emma Alexander `https://emmaalexander.github.io/resources.html`)

1.4 Astronomy Beyond the Visible Spectrum

The field of astronomy is arguably the first science systematically studied and practiced by humans. However, for most of that history, astronomy had been limited to a tiny fraction of the electromagnetic spectrum: the visible light that we can see with our eyes. This remained the status quo until the 20th century, when scientific and technological advancements allowed us to build and make use of detectors and telescopes that are sensitive to wavelengths across the entire spectrum. This led to a boom of astronomical discoveries and the creation of entire sub-fields of astronomy.

A further limitation is that the atmosphere absorbs most wavelengths of light. However, we are fortunately allowed two relatively wide "windows" from the surface of the Earth. The "optical window" is the most familiar, which spans 0.3 μm to 1 μm covering the Near-UV and Visible light, along with some clear bands of the Near-IR from 1 μm to 24 μm. The second is the "radio window" that spans roughly 30 m to 0.3 m (10 MHz to 1 THz respectively) (Pacholczyk, 1970). Above the optical window, the higher-energy X-rays and γ-rays are strongly absorbed by atomic and nuclear absorption, respectively. Between the optical and radio bands, molecular bands dominate the absorption of infrared radiation. Finally, below the radio window, the ionosphere becomes reflective due to the ionospheric electron density (Kelley, 2009).

Radio astronomy was born in 1932 with Karl Jansky's serendipitous detection of radio noise from the Milky Way as he was studying intermittent static sources of radio interference for transatlantic telephone transmission (Jansky, 1933). However, due to the difference in wavelength, radio observations are much less intuitive than optical observations, for which one can take direct images and count individual photons. Instead, radio telescopes typically collect radio waves from a patch on the sky with an antenna (a resonant structure on the scale of the wavelength) that converts the electromagnetic waves (in the form of photons) into alternating currents that are then amplified by radio-receivers and recorded. Naturally, such measurements provide only a single pixel view of the world, and to make radio images, one must either scan a single beam across the sky or use interferometry and synthesis imaging. This latter option uses multiple spatially separated radio telescopes to form an image by measuring the amplitude and phase over many points across the wavefront produced by an astrophysical object.

The technology of the radiometers used on radio telescopes has been steadily perfected over the decades since Jansky, but it still follows the same general design. The two most common types of receivers used in radio astronomy are coherent, superheterodyne receivers that retain the phase of the input signal, and bolometers that convert EM energy into heat. The sensitive front-end electronics are typically cooled down to cryogenic temperatures (often < 5 K) to reduce the contribution of self-generated thermal noise in the low-noise amplifiers and mixers (used for translating high-frequency (RF) signals down to intermediate frequencies (IF) that are easier to amplify, distribute, and record), and the detector itself in the case of bolometers. Advancements in receiver technology have greatly improved the sensitivity of modern radio telescopes, enabling them to see more distant and fainter astronomical sources. However, there are yet more improvements to be made, especially in methods for combating receiver instability (see Chapters 3 and 4).

Chapter 2

Dynamically Induced Polarization

2.1 Introduction

The redshifted 21-cm hyperfine transition of neutral atomic hydrogen (HI) provides a direct probe to the thermal evolution of the intergalactic medium (IGM) during the formation of the first bound objects and structures in the high-z Universe. This period is split into three general epochs: (1) the Dark Ages between Recombination ($z \sim 1100$) to $\sim 380,000$ yr after the Big Bang to the formation of the first bound/luminous objects at the start of (2) the Cosmic Dawn ($z \sim 30$), to the begining of net-reionization of the IGM at the start of (3) the Epoch of Reionization (EoR) ($z \sim 15$), through to the eventual full reionization of the IGM ($z \sim 6$) about 1 Gyr after the Big Bang (Madau et al., 1997; Furlanetto, 2006; Barkana, 2016; Pritchard & Loeb, 2010).

Experiments attempting to measure the redshifted 21-cm signal fall into two general categories. The first type are measurements of the angular power spectrum that track the spatial evolution of ionization bubbles in the IGM during the EoR using interferometers. Examples of such experiments include both purpose-built instruments such as PAPER (Parsons et al., 2010) and HERA (DeBoer et al., 2017), but also general-purpose telescopes like the MWA (Bowman et al., 2013) and LOFAR (van Haarlem et al., 2013). The other category consists of global, sky-averaged (monopole) measurements that track the spatially averaged evolution of the diffuse IGM using single or compact arrays of dipoles. Global experiments include EDGES I & II (Bowman et al., 2008; Bowman & Rogers, 2010; Monsalve et al., 2017; Bowman et al.,

2018), SARAS 1, 2, 3 (Patra et al., 2013; Singh et al., 2017; Jishnu Nambissan et al., 2021), BIGHORNS (Sokolowski et al., 2015), LEDA (Greenhill & LEDA Collaboration, 2015), SCI-HI (Voytek et al., 2014), and PRIzM (Philip et al., 2019).

However, the low-frequency ($\nu \lesssim 250$ MHz) measurements required to observe the 21-cm signal are extremely sensitive to instrumental and systematic errors, along with strong contamination by Galactic synchrotron emission and terrestrial radio frequency interference (RFI). While the predicted 21-cm signal is on the order of tens to hundreds of mK (Furlanetto, 2006; Mirocha et al., 2017), the radio synchrotron foreground has, on average, more than 4 orders of magnitude greater brightness temperature ($T_B \sim 10^3 - 10^4$ K;Kraus & Tiuri (1966)). Although the foreground emission is expected to be spectrally smooth (Kogut, 2012), the frequency-dependence of the antenna (or beam-chromaticity) can corrupt the foreground and complicate signal extraction due to degeneracies of the beam-weighting and spectral features of the 21-cm signal (Bernardi et al., 2015).

To date there have been no independently verified detections of the 21-cm signal beyond the result from EDGES II (Bowman et al., 2018) that detected an absorption feature centered about 78 MHz. However, there has been concern in the greater community as to whether this feature is real, because the reported signal depth from EDGES was greater by a factor of ~ 5 than theories predicted, which would point towards exotic physics during the early Universe. Alternatively, the reported signal may be a byproduct of instrumental artifacts (such as resonant modes in the ground plane; Bradley et al., 2019) or from calibration errors (Hills et al., 2018) that could readily produce false absoptions features. Additionally, evidence from the SARAS3 group has indicated a non-detection of the signal using an intrinsically different receiver and antenna design, which further puts into question the nature of the detected signal (Singh et al., 2021).

The ongoing observational and signal extraction challenges for global 21-cm experiments has motivated the continued development of new observational techniques to maximize unique information and constraining power. The inclusion of polarimetric data (e.g., from a crossed dipole) was proposed by Nhan et al. (2017, 2019) to provide further information due to the net-polarization induced by the foreground spatial anisotropy through the polarization leakage terms. The rotation of the Earth would sweep the antenna beam through the sky, thereby creating a characteristic, time-dependent modulation pattern in the observed Stokes parameters. This would

be due to only foreground sources since the 21-cm signal is expected to be spatially isotropic (on scales greater than 2°; Bittner & Loeb, 2011).

This polarimetric approach was further developed with the High-Band Cosmic Twilight Polarimeter (HB-CTP), an experiment to measure the long-term characteristics of the Dynamically Induced Polarization (DIP) effect predicted in wide-beam dipole measurements of the sky at 170 MHz. The instrument was designed for expediency, and thus made use of existing antenna and receiver hardware from the PAPER project (Parsons et al., 2010). The initial site prep and test observations were done by Ellie White (NRAO summer student) with Bang Nhan during the summer of 2019. Following the prelimiary results, I deployed a long-term and better characterized instrument from Fall 2019 to Spring 2020.

The outline for this chapter is as follows: Section 2.2 provides theoretical derivation of the dynamically induced polarization method and extension to the Mueller formalism, Section 2.3 provides details on the construction, operation, and calibration of the instrument, Section 2.4 presents the observed data and simulated models, and Section 2.5 summarizes findings and future improvements.

2.2 Dynamically Induced Polarization

2.2.1 Stokes Antenna Temperature

To motivate the use of dynamically induced polarization, we shall first consider how a typical radiometer sees the Universe at radio wavelengths. The eye of a radiometer, a device used to measure electromagnetic radiant flux, is the detector or antenna. An antenna is a radiative structure that can efficiently transform electromagnetic radiation into observable voltage and currents. This transformation can be quantified by a few important performance parameters: the radiation pattern $F(\theta, \varphi)$ from which the directivity, gain, and beamwidth can be derived, polarization (linear, circular, or elliptical), impedance at the antenna terminals, and frequency bandwidth.

The radiation pattern defines the angular variation of the radiation around an antenna typically considered in the far-field limit ($L >> \lambda$). The pattern may be directive, (characterized by having one or more distinct beams) or omni-directional (characterized by uniform radiation in one plane). However, these radiation patterns tend to be complicated for all but the simplest radiating systems, which feature

additional back/side-lobes that may cause sensitivity to signals away from the primary direction of interest. As a consequence, the perceived antenna temperature for a non-uniform radiation or source distribution can be mathematically described by

$$T_A = \frac{1}{\Omega_A} \int_0^{\pi} \int_0^{2\pi} T(\theta, \varphi) P_n(\theta, \varphi) d\Omega \tag{2.1}$$

where T_A is the observed antenna temperature, Ω_A the effectice antenna solid angle, $T(\theta, \varphi)$ the source temperature distribution, $P_n(\theta, \varphi)$ the normalized antenna response function, and $d\Omega = \sin\theta d\theta d\phi$ (Kraus & Tiuri, 1966). Thus, the antenna forms an interface between the Universe and the receiver, which cannot be readily disentangled from one another when the source distribution and/or beam patterns vary significantly over the field of view.

We may expand on the general antenna temperature for a radiometer to include the polarized nature of light. To do this we shall utilize the Jones and Mueller calculus commonly found in optical texts (Born & Wolf, 2019) to handle coherent (polarized) and partially-coherent (depolarized) light, respectively. We first introduce the 2×2 Jones matrix that describes the transformation of coherent light through a medium or optical element in the path of an incident wave.

$$\boldsymbol{e'} = \boldsymbol{J}\boldsymbol{e} = \begin{pmatrix} J_{AA} & J_{AB} \\ J_{BA} & J_{BB} \end{pmatrix} \begin{pmatrix} e_A \\ e_B \end{pmatrix} \tag{2.2}$$

where $\boldsymbol{e}$ and $\boldsymbol{e'}$ are the input and output electric field pair in an orthogonal basis (e.g., x-y linear or right/left-circular), while $\boldsymbol{J}$ is the feed response towards the direction of the incident wave, in general a complex unitless value.

For a dual-polarized antenna and assuming quasi-monochromatic conditions, $\boldsymbol{J}$ may be written as

$$\boldsymbol{J}(\theta, \phi; \nu) = \begin{pmatrix} |D_{\theta x}| e^{i\delta_{\theta x}} & |D_{\phi y}| e^{i\delta_{\phi y}} \\ |D_{\theta y}| e^{i\delta_{\theta x}} & |D_{\phi y}| e^{i\delta_{\phi y}} \end{pmatrix} \tag{2.3}$$

where $|D|$ and δ are the magnitude and phase of the θ and ϕ components of the farfield directivity pattern, each explicitly dependent on $(\theta, \phi; \nu)$. In case the $\hat{\theta} - \hat{\phi}$ basis is aligned with the linear E-field reference basis $\hat{x} - \hat{y}$, we can consider the the diagonal terms in the aforementioned Jones matrix as the co-polarization beam patterns while the off-diagonal terms are the cross-polarization beam patterns.

While the Jones matrix formulation is appropriate to treat coherent and polarized light, it is ill-suited to handle depolarization and unpolarized light. Instead we must consider the coherency vector (or equivalently the coherency matrix Born & Wolf, 2019; Hamaker et al., 1996):

$$\bar{\boldsymbol{e}} = \langle e_A \otimes e_B^* \rangle = \begin{pmatrix} \langle e_{Ax} e_{Bx}^* \rangle \\ \langle e_{Ax} e_{By}^* \rangle \\ \langle e_{Ay} e_{Bx}^* \rangle \\ \langle e_{Ay} e_{By}^* \rangle \end{pmatrix} \tag{2.4}$$

where the operator $\otimes$ denotes the "outer product" and subscripts A and B identify different antennas. The coherency vector contains the total intensities in the x and y directions, along with the complex correlation terms that describe the mutual "degree of coherence" that provide information on the polarization state of the light. Combining Equations 2.2 and 2.4 provides us with a general expression for capturing the effects of an optical system via their respective Jones matrix on the incident light:

$$\bar{\boldsymbol{e}} = \langle (\boldsymbol{J}_A \boldsymbol{e}_A) \otimes (\boldsymbol{J}_B \boldsymbol{e}_B)^* \rangle = (\boldsymbol{J}_A \otimes \boldsymbol{J}_B^*) \langle \boldsymbol{e}_A \otimes \boldsymbol{e}_B^* \rangle \tag{2.5}$$

where $(\boldsymbol{J} \otimes \boldsymbol{J}^*)$ forms a 4×4 coherency vector operator. A customary representation of polarized light is in terms of the Stokes vector (I,Q,U,V), an abstraction of the coherency vector space. For example, in a Cartesian basis the transformation of a coherency vector in $\hat{x} - \hat{y}$ to Stokes parameters is

$$\bar{\boldsymbol{e}}^S = \begin{pmatrix} I \\ Q \\ U \\ V \end{pmatrix} = \boldsymbol{A} \bar{\boldsymbol{e}}^+ = \begin{pmatrix} 1 & 0 & 0 & 1 \\ 1 & 0 & 0 & -1 \\ 0 & 1 & 1 & 0 \\ 0 & -i & i & 0 \end{pmatrix} \begin{pmatrix} \langle e_{Ax} e_{Bx}^* \rangle \\ \langle e_{Ax} e_{By}^* \rangle \\ \langle e_{Ay} e_{Bx}^* \rangle \\ \langle e_{Ay} e_{By}^* \rangle \end{pmatrix} \tag{2.6}$$

. Similarly, we may convert the 4×4 coherency vector operator into the Stokes system by pre- and post- multiplying by $\boldsymbol{A}$ and $\boldsymbol{A}^{-1}$, respectively, which results in the Mueller matrix:

$$\boldsymbol{M}(\theta, \phi; \nu) = \boldsymbol{A}\boldsymbol{N}(\boldsymbol{J} \otimes \boldsymbol{J})\boldsymbol{A}^{-1}. \tag{2.7}$$

A Mueller matrix describes how a Stokes vector is transformed by a medium or optical element in terms of total intensity and three polarization terms (Piepmeier

et al., 2008). To ensure that the coherency vector operator is normalized we include a normalization matrix:

$$\boldsymbol{N} = \begin{pmatrix} N_{11} & 0 & 0 & o \\ 0 & N_{22} & 0 & 0 \\ 0 & 0 & N_{33} & 0 \\ 0 & 0 & 0 & N_{44} \end{pmatrix} \tag{2.8}$$

where elements are defined as

$$N_{11} = \left(\int (J_{11} J_{11}^* + J_{12} J_{12}^*) d\Omega \right)^{-1} \tag{2.9}$$

$$N_{44} = \left(\int (J_{21} J_{21}^* + J_{22} J_{22}^*) d\Omega \right)^{-1} \tag{2.10}$$

$$N_{22} = N_{33} = \sqrt{N_{11} N_{44}}. \tag{2.11}$$

$$\tag{2.12}$$

By determining the Mueller matrix representation of an antenna, the full Stokes antenna temperature can be determined by

$$\boldsymbol{s}_{obs}(\nu) = \int_0^{\pi} \int_0^{2\pi} \boldsymbol{M}(\theta, \phi; \nu) \boldsymbol{s}_{sky}(\theta, \phi; \nu) d\Omega \tag{2.13}$$

where $\boldsymbol{s_{sky}}(\theta, \phi; \nu)$ is a Stokes vector angular source distribution, while $\boldsymbol{s}_{obs}(\nu)$ is the integrated, beam-weighted Stokes vector observed by the antenna. This equation is similar to Equation 2.1, and is equivalent in the case of purely unpolarized light. Following this approach, we have computed the Mueller matrix representation in Figure 2.1 for the PAPER antenna used in this experiment.

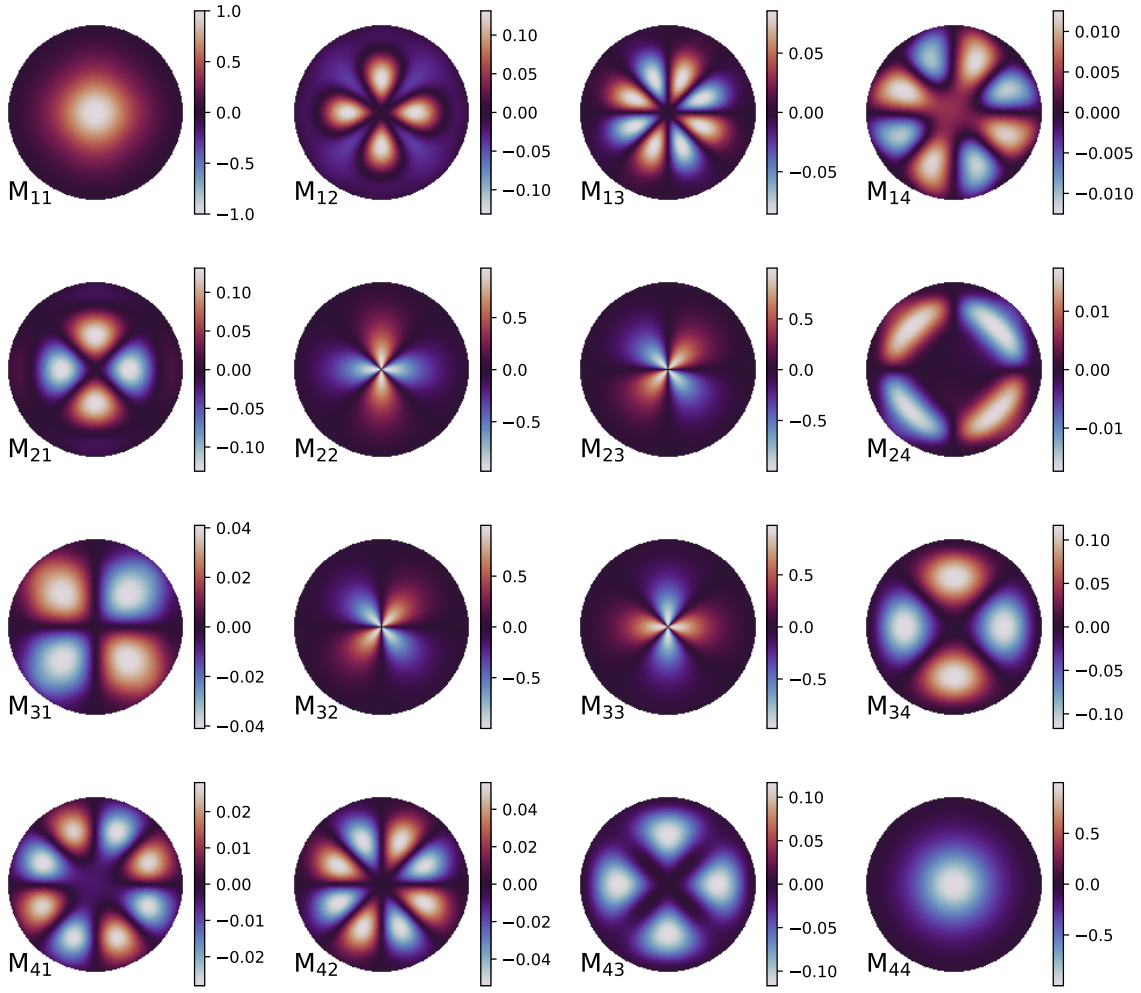

Figure 2.1: Mueller Matrix representation of the PAPER antenna. The 4×4 grid of maps in orthonormal projection is centered on the optical-axis of the antenna and covers the forward hemisphere. The main diagonal represents the idealized response of the optical system to an incident Stokes vector, while the off-diagonal elements quantify polarization leakage or mixing between polarization states.

2.2.2 A Non-Invertible Problem

Polarization leakage is a result of mechanical or electrical imperfections in an optical or radiating system that can be quantified by the off-diagonal terms in the Mueller

Matrix (Piepmeier et al., 2008). This causes polarization information from the incident signal to 'leak' or mix into different polarization components for the outgoing signal. In practice, this mixing of polarization states is an undesired side-effect that needs to be corrected by determining the leakage terms through the observation of known (un)polarized sources and then performing empirical calibrations. However, such corrections may only be applied if the beam pattern subtends a small solid angle such that Equation (2.13) approximates the linear equation:

$$\boldsymbol{s}_{obs}(\nu) \approx \boldsymbol{M}(\nu)\boldsymbol{s}_{sky}(\nu) \tag{2.14}$$

where both $\boldsymbol{M}(\nu)$ and $\boldsymbol{s}_{sky}(\nu)$ are effectively constant. This Mueller matrix is generally invertible, and therefore the sky Stokes vector can be solved:

$$\boldsymbol{s}_{sky}(\nu) \approx \boldsymbol{M}^{-1}(\nu)\boldsymbol{s_{obs}}(\nu) \tag{2.15}$$

For antennas with extended beams, Equation (2.13) will represent a non-invertible process (i.e., there is no unique relationship between input and output). This is generally the case for global 21-cm or other all-sky averaged measurements using low-frequency antennas, and thus, the antenna beam patterns cannot be disentangled from the source distribution and must be treated as a whole for such observations. This presents a major experimental challenge for global 21-cm experiments, since both the antenna and sky are difficult to constrain to the required precision to be sensitive to the faint background signal.

To quantify this problem, consider a Stokes source distribution composed of a foreground component and an arbitrary 21-cm signal component that is spatially isotropic and unpolarized:

$$\boldsymbol{s}_{sky}(\theta, \phi; \nu) = \boldsymbol{s}_{fg}(\theta, \phi; \nu) + s^{I}_{sig}(\nu)\hat{\boldsymbol{e}}_{\boldsymbol{I}} \tag{2.16}$$

where $\hat{\boldsymbol{e}}_{\boldsymbol{I}}$ is the Stokes I unit vector. We can relate the combined source distribution to the observed Stokes vector by substituting the above expression into Equation (2.13):

$$\boldsymbol{s}_{obs}(\nu) = \int_0^{\pi}\int_0^{2\pi} \boldsymbol{M}(\theta, \phi; \nu)[\boldsymbol{s}_{fg}(\theta, \phi; \nu) + s^{I}_{sig}(\nu)\hat{\boldsymbol{e}}_{\boldsymbol{I}}]d\Omega \tag{2.17}$$

Separating and moving the constant terms out of the integrals gives us the expanded

form:

$$\boldsymbol{s}_{obs}(\nu) = \int_0^{\pi}\int_0^{2\pi} \boldsymbol{M}(\theta,\phi;\nu)\boldsymbol{s}_{fg}(\theta,\phi;\nu)d\Omega + s_{sig}(\nu)\int_0^{\pi}\int_0^{2\pi} \boldsymbol{M}(\theta,\phi;\nu)\hat{\boldsymbol{e}}_{\boldsymbol{I}}d\Omega \quad (2.18)$$

We may further simplify this expression by recognizing that, by construction, the surface integral of $\boldsymbol{M}(\theta,\phi;\nu)\hat{\boldsymbol{e}}_{\boldsymbol{I}}$ is equal to $\hat{\boldsymbol{e}}_{\boldsymbol{I}}$ due to the normalization given in Equation (2.7). Thus, we can write the observed stokes antenna temperature as

$$\boldsymbol{s}_{obs}(\nu) = s_{sig}(\nu)\hat{\boldsymbol{e}}_{\boldsymbol{I}} + \int_0^{\pi}\int_0^{2\pi} \boldsymbol{M}(\theta,\phi;\nu)\boldsymbol{s}_{fg}(\theta,\phi;\nu)d\Omega \quad (2.19)$$

This highlights the general observational problem in 21-cm experiments, as the second term on the RHS results from a complicated and degenerate product of two spatially and frequency dependent quantities. Furthermore, the beam-weighted foreground is 4-5 orders of magnitude greater than that of the first background signal term that has an expected peak amplitude of ~ 100 mK. Thus, the beam-weighted foreground must be known to a precision of 1 part in $10^5 - 10^6$ in order to subtract out the term. However, this is generally not possible due to many compounding instrumental, observational, and systematic effects.

Although the beam-weighted foreground is a degenerate quantity, it can be constrained by a priori knowledge on each component that is physically or observationally motivated. An example of such a method uses an ensemble of physically motivated models that describe all physical processes that characterize the antenna beam response and foreground. This ensemble model contains a finite span of possible realizations of the Universe from which modes or eigenvectors can be determined via Singular Value Decomposition. These modes characterize the variation of the combined system with respect to observable quantities (e.g., time, frequency, polarization). In principle, if the ensemble model is complete such that it contains all physically relevant processes, then the observations can be reconstructed as a linear combination of the modeled eigen-modes (Tauscher et al., 2018b,a; Rapetti et al., 2020; Tauscher et al., 2020).

2.2.3 Signal Variations Due to Dynamic Polarization Leakage

To disentangle the complicated and degenerate beam-weighted foreground, we must consider the variations not just over frequency, but also over time, polarization, and orientation. We motivate this assumption by first considering an observation that takes an instantaneous snapshot of the total power, beam-weighted sky over a range of frequencies. Since all terms in Equation (2.19) are frequency dependent, the 21-cm signal will be degenerate with the beam-weigthed foreground as well. However, if we consider taking multiple snapshots over frequency and time, we can resolve a time-variable total power that is modulated by the rotation of the Earth with a period of 24 sidereal hours. Because we expect that the global 21-cm signal is spatially homogeneous and isotropic on the angular size of the beam, the time variations on the observed dynamic total power spectrum will be due to the product of the beam and the spatial anisotropic component of the foreground alone. Thus, we can qualitatively associate time variable eigen-modes to be only dependent on the beam and foreground.

As we have shown in section 2.2.1, antennas will in practice have polarization leakage. The off-diagonal terms in the Mueller matrix (see Figure 2.1) will cause the observed Stokes components to be a mixture of all components of the incident Stokes vector. We can generally expect the global 21-cm signal to be unpolarized (Bittner & Loeb, 2011), however the dominant radiation at frequencies of 10-100s of MHz is synchrotron radiation, the emission of relativistic electrons spiraling in magnetic fields that can be highly polarized (Pacholczyk, 1970). However, observations from the Westerbork Synthesis Radio Telescope (WSRT) show only weak polarized synchrotron emission on arcminute-scales that is not expected to be a major contaminant (Bernardi et al., 2009, 2010). Additionally, Faraday rotation due to the Earth's ionosphere can further randomize the observable polarization over time. Thus, we can therefore approximate that the observable foreground sky is largely unpolarized. If we extend our hypothetical observation to take measurements over time, frequency, and polarization, it becomes sensitive to the relative orientation of the anistropy with respect to the antenna, thereby further breaking degeneracies in the beam-weighted foreground term.

To illustrate the effects of such dynamic polarization measurements, we can construct a set of total power source distributions with different rotational symmetries and sample them with the first column of the Mueller matrix as shown in Figure 2.1.

The source distribution is then rotated about the optical axis of the antenna and summed via Equation 2.13. Figure 2.2 shows that a non-zero polarized response can only be suppressed for Stokes Q and U with a source distribution that is at least a multiple of 4-fold rotational symmetry, while for Stokes V at least a multiple of 8-fold rotational symmetry is required. Conversely, any source distributions that do not follow these symmetry rules will excite a non-zero polarization response, thereby providing information on the relative alignment of the spatial structure of the foreground with respect to the antenna.

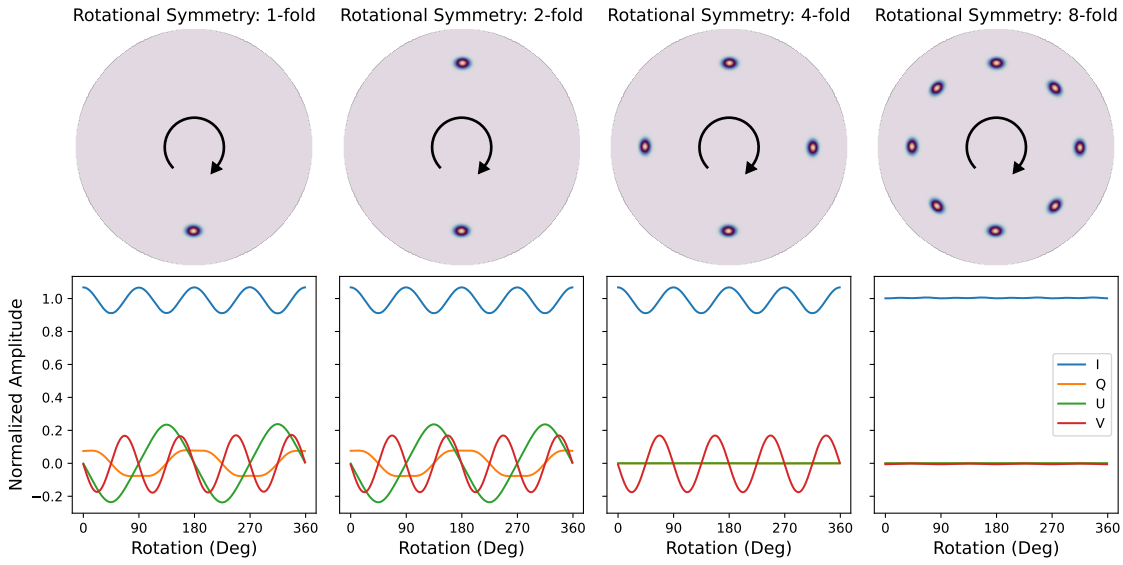

Figure 2.2: Shown are the normalized polarization responses of a real antenna beam to a set of rotationally symmetrical foreground distributions. Because of the cross-dipole construction of the studied antenna, the polarization leakage of unpolarized to polarized will generally have a quadrupole or octupole like spatial response. Thus, if a total power source distribution matches the symmetry of the polarization leakage, no net polarization is excited.

2.3 Experimental Design

To detect the Dynamically Induced Polarization a simple experimental receiver was designed for polarimetric measurements of the sky with a low-frequency crossed-dipole appropriate for similar cosmological 21 cm experiments. Due to the significant instrumental relatede effects for such experiments, it is important to consider the

nature of the instrument as part of the greater measurements system which ultimately defines the polarization response of the receiver. The relevant system components (see Figure 2.3) will be discussed in the following section.

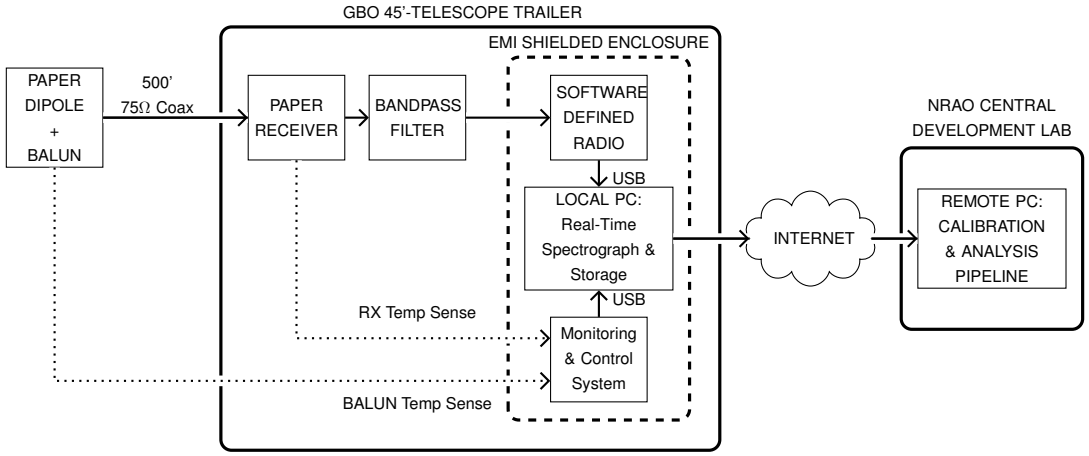

Figure 2.3: Block Diagram of the HB-CTP experiment

2.3.1 RF Frontend Receiver System

For expediency, the RF Frontend Receiver System made significant use of existing and tested hardware left over from the development of the Precision Array for Probing the Epoch of Reionization (PAPER; Parsons et al., 2010). The critical components are considered in the order that the signal takes through the system. The first element is a dual-polarized, sleeved dipole antenna (or feed). The dipole elements are made from thinwall copper tubing that lie between two circular aluminum plates, or sleeves, that create a dual-resonant structure optimized to broaden the operating range of the antenna to 120-170 MHz. The feed is paired with a 2×2m wire-mesh groundscreen and 45° angled planar reflectors that create a trough reflector to increase the gain of the antenna (reducing ground pickup).

The second element is the the PAPER BALUN, which is integrated into the dipole assembly of the feed. This BALUN, short for "BALanced to UNbalanced," is operating as a pseudo-differential amplifier that amplifies each arm of the dipole before combining with a 180°-hybrid junction to form the dipole beam. This pre-amplification helps maximize noise performance since it avoids the ohmic losses before the amplifers, compared to typical balun configurations used at these frequencies (e.g.,

via transformers, or hybrids). Additionally, the significant gain at the antenna allows it to function like a "line-driver," minimizing loss of signal-to-noise from cable losses between the feed and the receiver module.

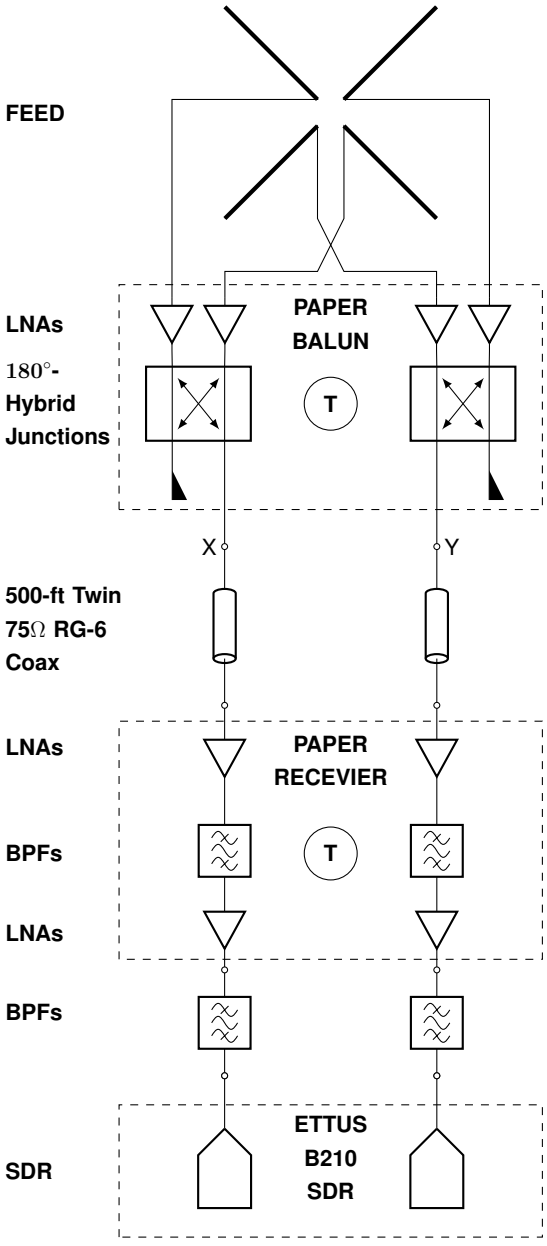

(a) RF System Block Diagram

(b) PAPER Feed/Antenna

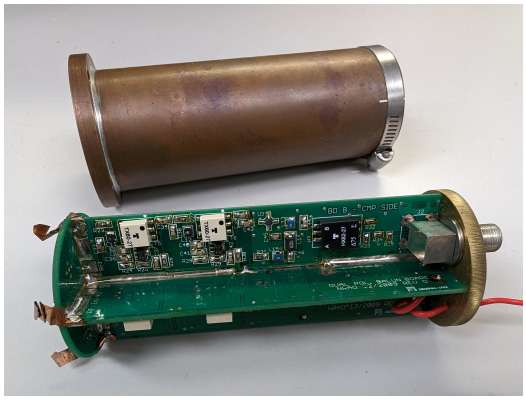

(c) PAPER Balun

(d) PAPER Receiver Module

Figure 2.4: HB-CTP RF system diagram along with individual highlighted components

The next element is the PAPER Receiver Module that conditions the signal before entering the data acquisition system and spectrograph. This includes an impedance tranformation from the 75Ω transmission impedance to 50Ω typically used for general lab and RF equipment. Additionally, the module has further gain stages, for a total gain of ∼60dB, to compensate for potential cable losses, thus boosting the signal to a high enough level to be effectively digitized. Finally, the module also includes a bandpass filter (130-185 MHz) to suppress potentially strong out-of-band interference such as FM radio at 87.5-108 MHz and digital TV (54-88 MHz and 174-216 MHz).

The final element of the frontend receiver system is a pair of tunable narrow bandpass filters to help further suppress strong radio interference and act as an additional anti-aliasing filter before the Software Defined Radio (SDR).

2.3.2 Digital Backend Receiver System

We developed a digital backend receiver system to acquire, process, and record the analog signals produced by the RF frontend in real-time. This system was composed of three functional sub-systems: a dual channel Software Defined Radio (SDR), a microcontroller-based monitoring and control system, and a spectrograph running on a standard desktop computer. Using commerically available hardware allowed for rapid-prototyping with a primary focus on the design and implementation of the instrument software. The design decisions and development are summarized for each sub-system within the rest of this section.

Software Defined Radio

A software defined radio, as the name suggests, is a device whose signal processing functions are implemented in software rather than conventional analog hardware (e.g., filters, mixers, modulators/demodulators, etc). These devices enable highly flexible and configurable RF transceiver systems that are well suited for communications and RF prototyping. As such, they typically feature a direct conversion (quadrature sampling) architecture used to separate the upper and lower sidebands during analog up/down-conversion. This approach both removes the need for a tunable RF filter used to suppress the image, as in the case for a conventional superheterodyne receiver, but also is effectively required for nearly all common-signal modulation schemes used for communications today (Sklar, 2009). However, some drawbacks of SDRs should

be noted for measurement and laboratory applications due to their generic design. In practice, compared to a superheterodyne receiver, a direct-conversion architecture will have both less sideband rejection than a physical image rejection filter, and more contamination from the LO and low-frequency noise because these components are mixed down to the DC component in the center of the IF band, rather than above or below. Fortunately, for our simple continuum measurements, we can largely ignore these risks.

We used the Ettus Research B210, a two-channel SDR with continuous coverage over 70 MHz - 6 GHz, to digitize the band-limited signal at the end of the RF frontend. This radio was mainly chosen because it is easy to interface over USB3 and supported the two phase-coherent (simultaneously sampled) receiver chains required for polarimetery. An additional factor was its compatibility with the open-source `GNU Radio` software development toolkit that greatly sped up development time. For our simple experiment, the radio was configured using a `GNU Radio` script to implement two receiver channels, each with a center frequency of 169 MHz and 10 MHz of bandwidth with no additional receiver gain. The quadrature (I/Q or complex valued) voltages for the two channels were interleaved and streamed using a TCP server.

Monitoring and Control System

Next is the custom built Monitoring and Control System (MCS), which was used to track the physical temperature of the PAPER balun and Receiver module and critical for calibration purposes. The physical state of these modules was measured with a pair of Texas Instruments LM135 precision temperature sensors, which functionally operate as a zener diode whose breakdown voltage is directly proportional to the sensor temperature ($V_{out} = 10mV/°K$). These sensors were attached to metal tabs and mounted onto the balun and receiver for good thermal contact (as seen in Figure 2.7b) and attached to the MCS using shielded twisted pair cabling. The MCS itself was implemented using a STMicroelectronics NUCLEO-L432KC development board and an external Microchip Technology MCP3304 analog-to-digital converter to measure the sensor voltages. The MCS was programmed to continuously read and average the two sensor voltages over an integration period of ≈ 2.5 seconds, and then stream the derived temperatures over USB-Serial to the backend computer for further processing and storage.

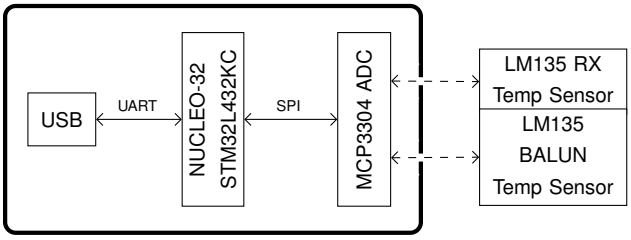

(a) HB-CTP MCS Block Diagram

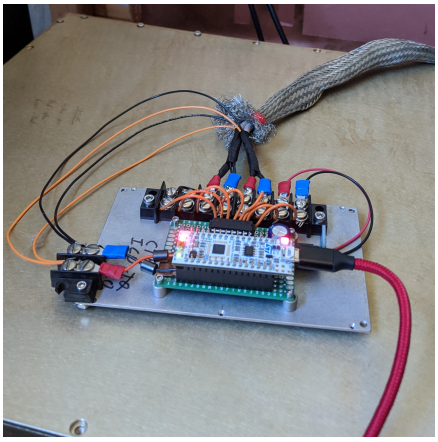

(b) HB-CTP MCS in the field

Figure 2.5: The HB-CTP Monitoring and Control system

Spectrograph

The final component of the Digital Backend is the core software application, encompasing the real-time spectrograph that processes the raw data produced by the SDR and MCS. The spectrograph performs a number of critical signal processing tasks including: transforming the complex voltage timeseries into spectra for both polarizations, computing the auto and cross-power spectra, and finally producing the averaged power spectra and Spectral Kurtosis estimator (Nita & Gary, 2010) per integration period. The program was written in C++ and operated on a standard desktop computer (with an Intel i7-8700 3.2GHz 6c/12t CPU and 16GB of RAM), co-located with the SDR and MCS in a shielded enclosure to prevent RFI/EMI at the site.

The primary design challenges for the spectrograph were stability and sustained data throughput to process about 160 MBps (or $\sim$ 14TB per day) of streaming I/Q data produced by the SDR. To ensure program and memory safety, all data structures and buffers were instantiated at startup and reused throughout the execution of the program, therefore providing memory safety. Additionally, custom fixed-size circular buffers were used to safely pass data frames from producer to consumer threads to ensure safety in case of processing time variations. These circular buffers are used to regulate the transport of packetized data to and from a thread-pool of FX engines that perform the digital signal processing. Each of the identical FX threads uses a 16-

tap Polyphase Filter Bank (PFB) channelizer implemented with the FFTW3 (Frigo & Johnson, 2005) and FFTW++ libraries with a windowed-sinc filter to minimize spectral leakage. The instantaneous voltage spectra are then cross-correlated and integrated over time, during which the Spectral Kurtosis (Nita & Gary, 2010) is computed for each frequency channel.

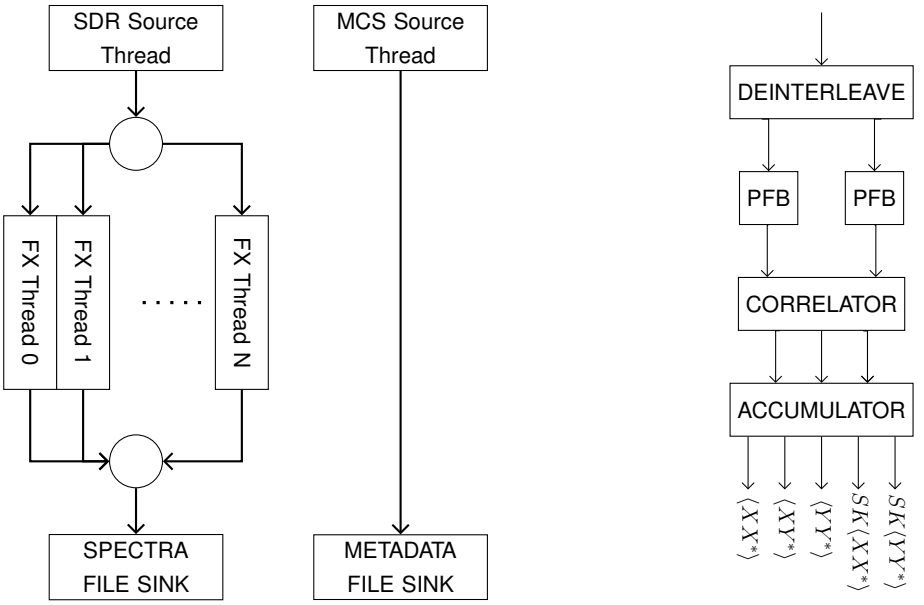

(a) HB-CTP Software Diagram (b) FX Thread

Figure 2.6: HB-CTP Software Diagram

Parameter	Value
Input Bandwidth	10 MHz
FFT Size	8192
Channel Resolution	1.22 kHz
PFB Filter	16-Tap Windowed Sinc
Integration Time	6.5s

Table 2.1: HB-CTP Spectrograph Specifications

2.3.3 Calibration

Because the RF frontend made use of existing hardware that was not designed for absolute measurements, we had to rely on alternative calibration methods to account

for large scale variation in receiver gain. These large gain fluctuations were generally correlated with the physical temperature of the electrical device, especially active components such as Transistors (Massobrio & Antognetti, 1993). Thus, we used the physical device temperature as a proxy measurement of the instrument state using a lab calibrated "black-box" model of the RF receiver system dependent on temperature.

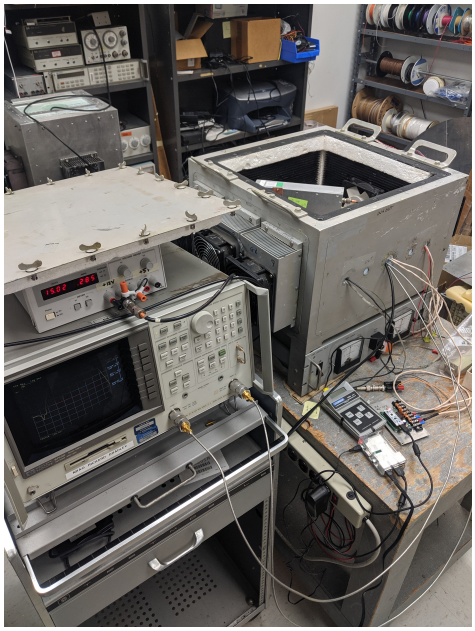

(a) Calibration test setup with HP 8753D VNA

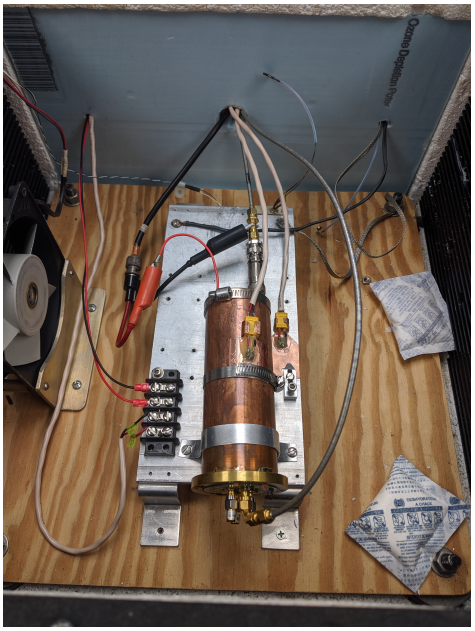

(b) Closeup of PAPER balun in Temperature Controlled Box.

Figure 2.7: Calibration of HB-CTP RF Components

Creating the instrument model involved individually characterizing each component of the RF signal path using scattering parameters (or S-parameters) measured with a Vector Network Analyzer (VNA). These scattering parameters quantify the complex-valued reflection and transmission characteristics of a steady-state and linear N-port network. These S-parameters can also be readily cascaded together (using ABCD-parameters) to form a larger network (Pozar, 2012). While the passive devices, such as the tunable filers and coax cables, were measured at ambient room temperature as they are only weakly sensitive to temperature (or difficult to measure in the field, such as the buried coax cables between the antenna and receiver). The active components, the PAPER balun and receiver modules, were fitted with temperature sensors and measured with 5 points over a temperature range of $16^\circ - 32^\circ$

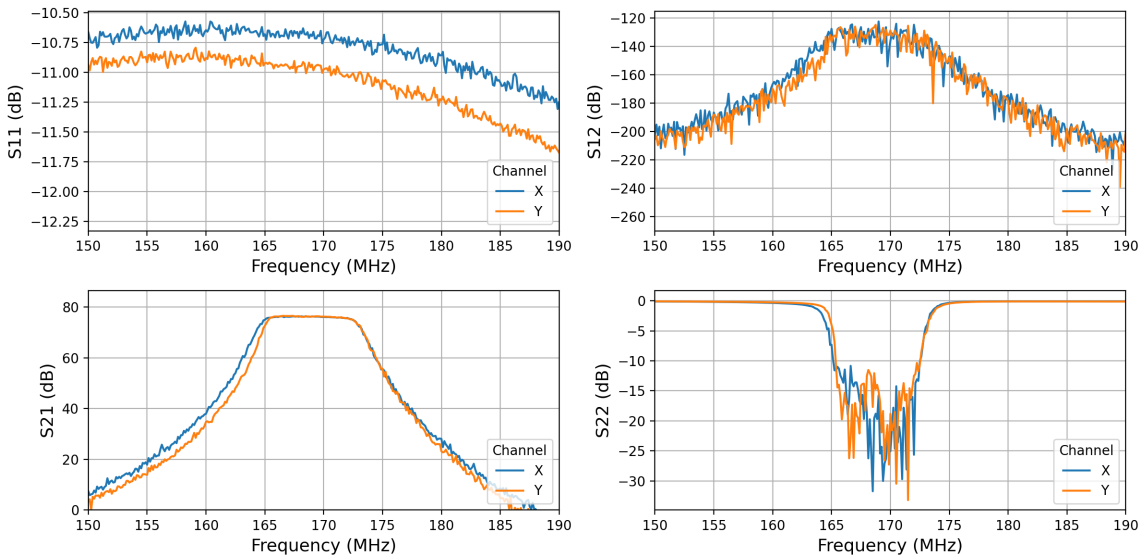

Figure 2.8: HB-CTP Cascaded S-parameters

Celsius using a temperature controlled box (see Figure 2.7).

Using standard microwave network theory, the effective gain (or S21), of the cascaded networks was computed for all available combinations of balun versus receiver module temperatures for both channels (see Figure 2.8 and 2.9). The resulant gain was then fit to a 3-dimensional hypersurface of polynomials parameterized in frequency, balun, and receiver temperature with the following form:

$$\begin{aligned} \boldsymbol{G}(T_{rx}, T_{balun}, \nu) = c_0 \\ &+ c_1 T_{rx} + c_2 T_{rx}^2 \\ &+ c_3 T_{balun} + c_4 T_{balun}^2 \\ &+ c_5 \nu + c_6 \nu^2 + c_7 \nu^3 + c_8 \nu^6 \end{aligned} \tag{2.20}$$

The resultant gain model for both channels is shown in Figure 2.9 at 170 MHz. The last part of the instrument model is the noise temperature of the first element, which effectively establishes the noise performance of the system (Friis, 1944). Using a Noise Figure Analyzer (NFA) the noise temperature of the balun was measured for both channels and a first order polynomial was fit only over frequency (assuming no temperature dependence), as shown in Figure 2.10.

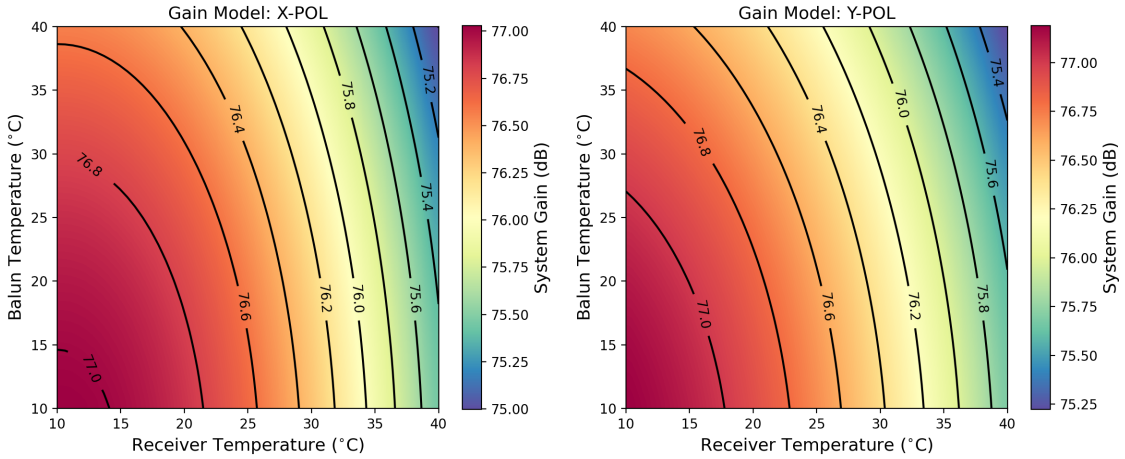

Figure 2.9: HB-CTP Gain vs. Balun and Receiver Temperature at 170 MHz

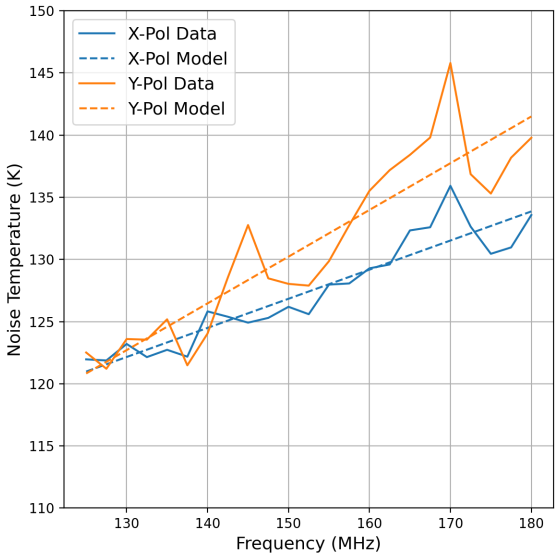

Figure 2.10: HB-CTP Noise Temperature

2.3.4 RFI Mitigation and Excision

Radio Frequency and Electromagnetic Interference, or RFI/EMI, is a key challenge facing radio measurements, especially in the increasingly crowded RF spectrum. The biggest concern of RFI is potential damage to the sensitive receiver or down-stream systems. To measure very faint signals, radio receivers need significant gain or amplification (upwards of $\sim$100 dB or a factor of 10^{10}). At large input power levels, an amplifier may be operating beyond its linear range, thereby creating harmonics and intermodulation products as the amplifier begins to "compress." Furthermore, due to the finite gain-bandwidth product of amplifiers, strong interferers may cause the whole passband to compress and reduce the overall signal level across itself. A real example of this broad-band compression can be observed as the horizontal dips in power accross frequency that are caused by a strong out-of-band signal, shown in the waterfall plots of Figure 2.11. In the worst case, applying an input signal beyond the designed limits of amplifiers, mixers, analog-to-digital converters, or other sensitive devices, may physically damage or even destroy the device. These concerns must be addressed in hardware (e.g., filters, power limiters, amplifier design, etc.) or by minimizing the likelihood of interception of strong RFI signals (e.g., steering the primary beam and sidelobes away from known strong interference).

While physical damage to a receiver can be generally avoided, an insidious problem remains: low to moderate power inference in the targeted frequency band. In practice, these signals cannot be removed in hardware without also removing or disturbing the underlying signal. While analog/digital notch-filters can prevent strong and persistent signals (e.g., 50/60Hz AC or AM/FM radio) from corrupting measurements of the adjacent spectrum, it is not a scalable or appropriate solution for narrow-band or time/frequency variable RFI. Therefore, it is preferable to not alter the main passband of the receiver and instead, identify and excise RFI in post-processing of the data using empirical or statistical flagging methods.

One such method is the Spectral Kurtosis Estimator described by Nita & Gary (2010), a descriptor of how heavy-tailed or light-tailed a distribution is relative to a normal distribution. Because RFI is associated with man-made devices, these signals will contain some form of information, intentional or incidental. Modulations in time, amplitude, phase, and frequency give rise to patterns within the signal such that successive measurements will have some temporal correlation (samples are dependent

on the prior value), while samples produced by a noise-like Gaussian process will remain independent and uncorrelated. Therefore, information containing signals will also generally have a distribution of samples that deviate from a normal distribution and can be tested using the Spectral Kurtosis:

$$\widehat{SK} = \frac{M+1}{M-1}\left(\frac{MS_2}{S_1^2} - 1\right) \tag{2.21}$$

where M is the number of samples and S_1 and S_2 are defined as

$$S_1 = \sum_{i=1}^{M} P_i, \quad S_2 = \sum_{i=1}^{M} P_i^2 \tag{2.22}$$

The expectation value of the Spectral Kurtosis for a normal distribution will be E[SK(...)]=1, where values above 1 will have lighter tails and values below 1 will have heavier tails. Thus, potentially RFI-contaminated data can be identified by setting allowed upper and lower thresholds about the expectation value of the spectral kurtosis for Gaussian noise. Data falling outside of this range are then flagged as likely RFI. Because this is an empirical approach, the set threashold must be tuned to the data to prevent excessive or insufficient flagging.

We made use of all of these methods in the design and operation of the experiment to mitigate the risk of harmful interference. While much of the hardware could not be modified to prevent out-of-band noise from entering the system, we used tunable, narrow-band filters between the PAPER receiver module and SDRs to restrict the input bandwidth and reduce the risk of damage from strong out-of-band interference as well as to reduce aliasing. Additionally, the spectrograph will simultaneously accumulate both the auto/cross-power spectra (S_1) and the square of the auto-correlations S_2 over the integration period, such that the Spectral Kurtosis can be estimated for the two polarizations. An example of these data are shown in the bottom two subplots of Figure 2.11. From the collected data, we have selected a symmetric range of $\widehat{\mathrm{SK}} = 1 \pm 0.05$ to be valid data. The outlying data was then excised so that the final coarse frequncy and time binning operations would be minimally contaminated.

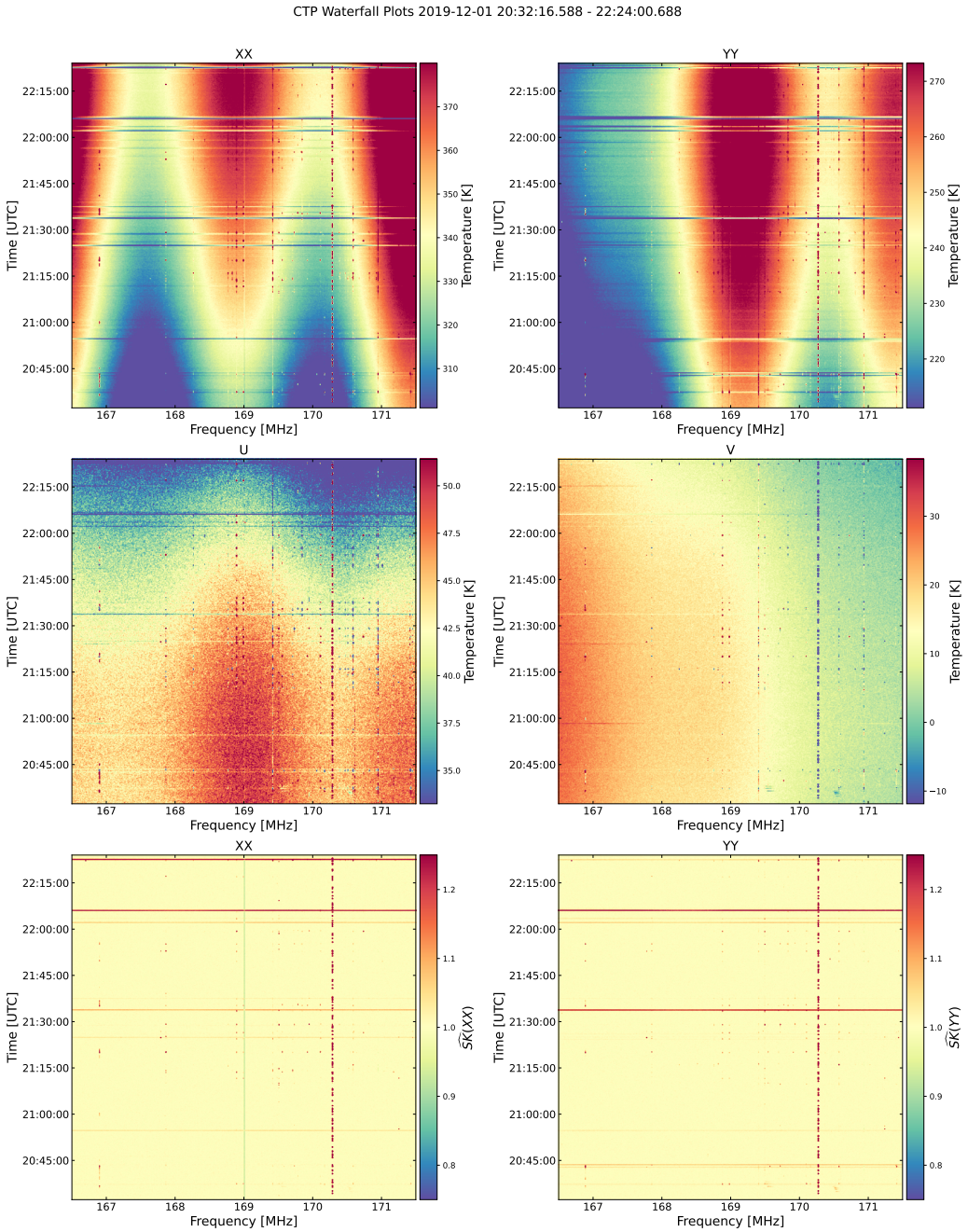

Figure 2.11: Shown are waterfall plots of the calibrated auto (XX, YY) and cross power (Stokes U, V) spectra in terms of effective brightness temperature. A smooth continuum can be observed along with in-band interference (narrow-band features variable in time), alongside compression events due to strong interference saturating the amplifiers (wide-band features variable in time). Also shown is the concurrent Spectral Kurtosis Estimate, which shows similar RFI feature as in the spectral data.

2.3.5 Data Reduction Pipeline

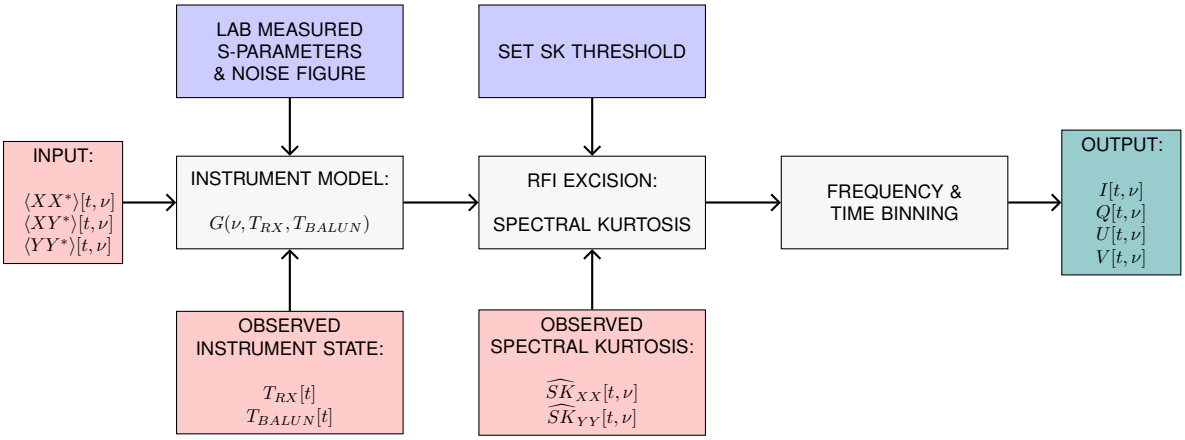

Figure 2.12: HB-CTP Calibration and Data Reduction Pipeline

The data reduction pipeline was a set of completely automated scripts that continuously calibrated and reduced batches of raw data to produce the final science data and diagnostics plots.

1. Calibration of raw spectra data using the estimated instrument state from temperature sensor data (see Section 2.3.3).
2. First RFI excision using a cut for spectral kurtosis $\widehat{\mathrm{SK}} = 1 \pm 0.05$ (see Section 2.3.4).
3. Frequency binning of central 5 MHz into 16 bins (BW $\sim$ 312.5 kHz).
4. Saving of calibrated data to an intermediate HDF5 file.
5. Calculation of Local Sideral Time (LST).
6. Second RFI/outlier cut with sigma clipping ($\sigma \leqslant 3$) when time binning each sidereal day into 128 bins ($t \sim 11$ min).
7. Calculation of Stokes antenna temperatures of binned data using Equations 2.23 (see Section 3.2.3).
8. Saving of completely processed data to reduced HDF5 file.
9. (Optional) Correction of data by fitting an instrument gain correction/imbalance model using simulations as the reference.

$$
\begin{aligned}
\langle T_I \rangle_{\nu,t} &= \frac{1}{k_B \Delta\nu}\left[\frac{\langle v_x v_x^* \rangle}{G_x} + \frac{\langle v_y v_y^* \rangle}{G_y}\right] - T_{n,x} - T_{n,y} \text{ (K)} \\
\langle T_Q \rangle_{\nu,t} &= \frac{1}{k_B \Delta\nu}\left[\frac{\langle v_x v_x^* \rangle}{G_x} - \frac{\langle v_y v_y^* \rangle}{G_y}\right] - T_{n,x} + T_{n,y} \text{ (K)} \\
\langle T_U \rangle_{\nu,t} &= \frac{2}{k_B \Delta\nu}\mathrm{Re}\left[\frac{\langle v_x v_y^* \rangle}{\sqrt{G_x G_y}}\right] \text{ (K)} \\
\langle T_V \rangle_{\nu,t} &= \frac{2}{k_B \Delta\nu}\mathrm{Im}\left[\frac{\langle v_x v_y^* \rangle}{\sqrt{G_x G_y}}\right] \text{ (K)}
\end{aligned}
\tag{2.23}
$$

2.4 Results and Analysis

2.4.1 Observation Simulations

Physically realistic simulations are vital for determining the characteristic dynamical variations in the observed signal. These models must not only include information about foregrounds (e.g., using reference sky maps), but also how the sky changes as a function of frequency (e.g., as a power law with spectral index β), along with any relevant propagation effects that can distort or alter the signal before it finally reaches the instrument with its own specific response characteristics. For this experiment, we primarily considered terrestrial effects on a mock 21-cm experiment, including ionospheric/tropospheric absorption and refraction and horizon obstructions.

These effects can be treated numerically using the mathematical formalism discussed in Section 2.2, along with the Mueller matrix representation of the PAPER antenna. In general, we can model an observation with the following equation to find the time and frequency dependent Stokes antenna temperature:

$$
\langle T_A \rangle_{\nu,t} = \int_0^{\pi}\int_0^{2\pi} \boldsymbol{M}(\theta,\phi;\nu)\tilde{s}_{sky}(\theta,\phi;\nu,t)\hat{\boldsymbol{e}}_{\boldsymbol{I}} d\Omega \tag{2.24}
$$

where the distorted sky Stokes vector $\tilde{s}_{sky}$ is,

$$
\tilde{s}_{sky}(\theta,\phi;\nu,t) = \begin{cases} D_\nu\big(T_{408}(\theta,\phi,t)\big[\frac{\nu}{408\,\mathrm{MHz}}\big]^{-\beta(\theta,\phi)}\big)A(\theta,\phi,\nu) & \\ \quad +E(\theta,\phi,\nu) & \text{for } \theta < \theta_{horizon} \\ T_g & \text{for } \theta > \theta_{horizon} \end{cases} \tag{2.25}
$$

where $D_\nu(...)$ is the frequency and pointing dependent distortion function due to refraction in the ionosphere and troposphere, T_{408} is the 408 MHz Haslam Map (Haslam et al., 1981) scaled by a spectral index β that may be position dependent, $A(\theta, \phi, \nu)$ and $E(\theta, \phi, \nu)$ are the frequency and pointing dependent absorption and emission, respectively, and T_g is the brightness temperature of the ground ($T_g \sim 300$K).

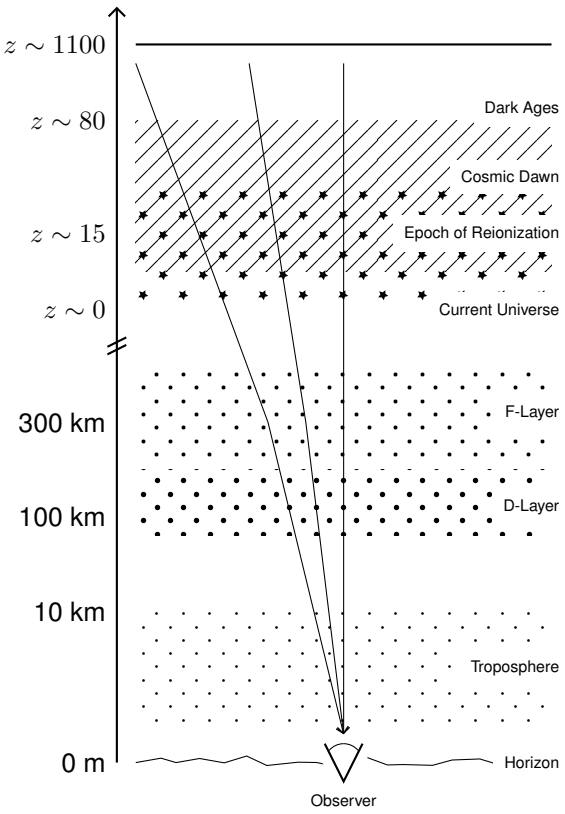

Figure 2.13: Cartoon diagram of model layers traversed by the global cosmological 21-cm signal to the detector.

Ionospheric Effects

The ionosphere corresponds to the partially ionized layers of the Earth's upper atmosphere (50-1000 km) that form an important interface relevant to the propagation of radio waves (Budden, 1988). The ionosphere is excited by solar activity via photoionization from high-energy photons (UV and higher) and flares, as well as high-energy particles in the solar wind that get trapped by the Earth's magnetosphere (especially towards the high-latitude regions; Kelley, 2009). This causes the ionosphere to be stratified yet highly dynamical and time-variable (on the order of few minutes) due

to plasma instabilities and turbulence driven by the solar wind buffeting the magnetosphere, along with the differential irradiation by the Sun (Kelley, 2009). This generally leads the day-time ionospheric layers to be enhanced in their number density of ions and with more distinct layers compared to the night-time ionosphere that is roughly a factor of 10 reduced, as ionized species quickly recombine to form neutral species (Kelley, 2009).

The ionosphere will, in practice, influence the propagation of high-frequency radio waves in five primary ways: refraction, absorption, emission, Faraday rotation, and scintillation (Datta et al., 2016; Budden, 1988). The refraction due to the ionosphere is primarily due to the extended F-layer ($h \sim 300$ km), which has the highest electron density and forms a spherical lense (Budden, 1988; Vedantham et al., 2014). Well above the plasma frequency ($\nu_p \sim 15$ MHz), the refractive index is given by (Bailey, 1948; Evans & Hagfors, 1968; Budden, 1988; Datta et al., 2016):

$$\eta^2(\nu, t) = 1 - \left(\frac{\nu_p(t)}{\nu}\right)\left[1 - \left(\frac{h - h_m}{d}\right)^2\right] \tag{2.26}$$

where h is the altitude, h_m is the altitude with peak electron density in the F-layer, and d is the scale length. However, the propagation of radio waves at frequencies closer to the cutoff is significantly distorted and would generally require numerical ray-tracing simulations to predict (see Figure 2.15). However, due to refraction, sources below the line-of-sight horizon can become visible.

Absorption in the ionosphere is due to the interaction of radio waves and the free electrons, heavier ions predominantly in the D-layer ($h \sim 80$ km) of the ionosphere (Kelley, 2009; Budden, 1988). The energy of the radio wave is converted to heat and electromagnetic noise of the ionospheric medium and depends on the collisional coupling of the ions and neutral species. Following Evans & Hagfors (1968), the total D-layer absorption can be expressed as

$$\begin{aligned} L_{dB}(\nu, n_e) &= \frac{1.16 \times 10^{-6}}{\nu^2} \int n_e \nu_c ds \quad [dB] \\ L_{dB}(\nu, TEC_D) &= \frac{1.16 \times 10^{-6}}{\nu^2} \nu_c \mathrm{TEC}_D \quad [dB] \end{aligned} \tag{2.27}$$

where ν_c is the mean collision frequency and TEC_e is the total electron column depth at the given slant angle through the ionosphere (Evans & Hagfors, 1968; Boithias,

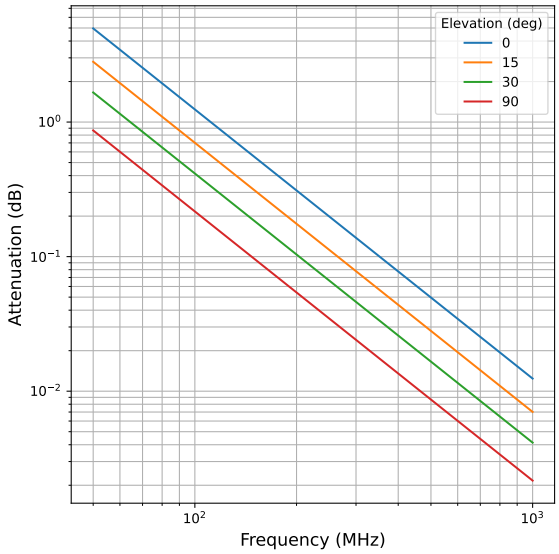

Figure 2.14: Approximate day-time Ionospheric Absorption. Value for night-time will be a factor of 10-30 less. Based on (Boithias, 1987)

1987) (see Figure 2.14). Directly related to the absorption is the emission which is given by

$$\begin{aligned} L_{dB}(\nu, TEC_D) &= 10log_{10}(1 - \tau(\nu, \mathrm{TEC}_D)) \\ E(\nu, \tau) &= \langle T_e \rangle \tau(\nu, \mathrm{TEC}_D) \end{aligned} \tag{2.28}$$

where T_e is the mean electron temperature in the D-layer and τ is the optical depth related to the total electron content (Datta et al., 2016; Pawsey et al., 1951; Steiger & Warwick, 1961).

Because the ionosphere is also a slighly anisotropic plasma due to the magnetic field of the Earth, polarized radio waves will experience Faraday rotation as they propagate through the F-layer of the ionosphere (Burn, 1966; Budden, 1988). Following (Burn, 1966), the Faraday rotation has the functional form

$$\phi(\boldsymbol{r}) = 0.81 \int_{there}^{here} n_e \boldsymbol{B} \cdot d\boldsymbol{r} \quad [rad \cdot m^{-2}] \tag{2.29}$$

where n_e is the mean electron density (in cm^{-3}) and $\boldsymbol{B}$ is the magnetic field. Thus the projected magnetic field strength in the line-of-sight to the source will cause a rotation of linear polarization. Scintillation is due to the small-scale variations (few meter to tens of kilometers) in the ionosphere that cause rapid fluctuations in amplitude and phase coherency (van Bemmel, 2007).

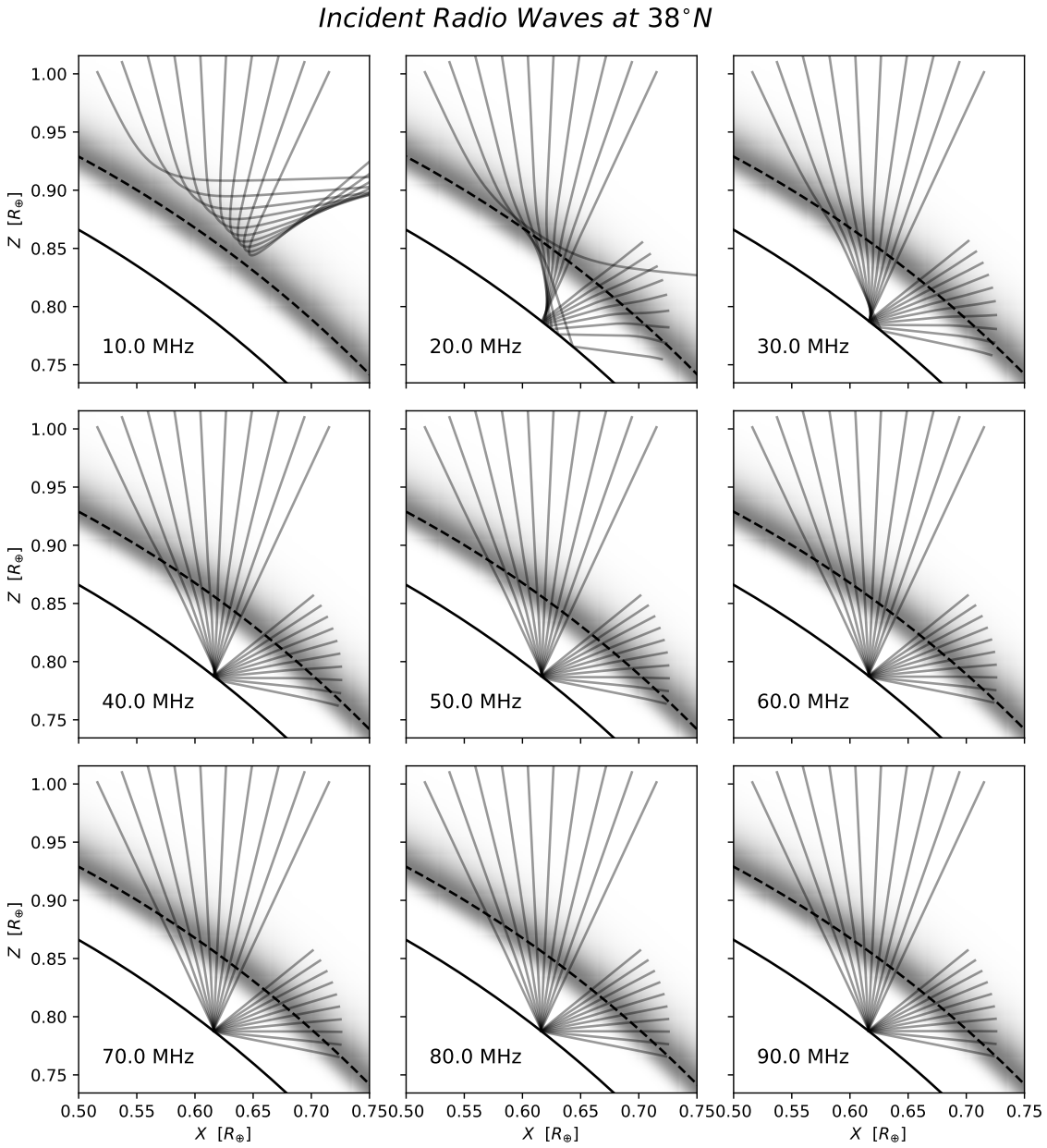

Figure 2.15: Ray tracing simulations of incident radio waves at below 100 MHz for typical day-time ionospheric conditions using a custom made 3D ray-tracing program. Note the strong frequency dependent effects close to the plasma frequency of $\nu \sim 15$ MHz that can produce significant distortions in the ray path to the point of being completely reflective.

HB-CTP Simulations

We used Equations 2.24 and 2.25 to predict the dynamically-induced polarization for various system conditions and nominal atmospheric conditions. We used the 408 MHz Haslam Map (Haslam et al., 1981) scaled down to 170 MHz with a constant spectral index ($\beta = 2.5$) as the source map that was rotated through a complete 360° and sampled by the first column of the beam Mueller matrix. We additionally included a location dependent effect: the local horizon obstructions, which were surveyed at the site using a level transit (see Figure 2.17; see Bassett et al. (2021) for further information of this effect). The local horizon obstruction creates further spatial anisotropy that alters the polarization vector response from the dynamically-induced polarization effect. Finally, we considered the effects of the antenna alignment with respect to the local meridian (e.g., alignment with respect to geographic north), which significantly changes the dynamically-induced polarization response, as it changes the spatial coupling to different parts of the sky (see Figures 2.17 and 2.16).

We find for an unpolarized sky brightness distribution and uniform ionospheric conditions in the field of view that atmospheric effects generally scale the dynamically-induced polarization features at the percent level. This is because the refraction and absorption to be symmetrical about the zenith, whose effects become more significant towards the horizon, but are ultimately limited by the decrease in effective gain of the antenna (or elements of the Mueller matrix). However, the simulations show that the sky-beam system are strongly affected by the relative orientation of the polarization basis of the antenna and the structure of the sky.

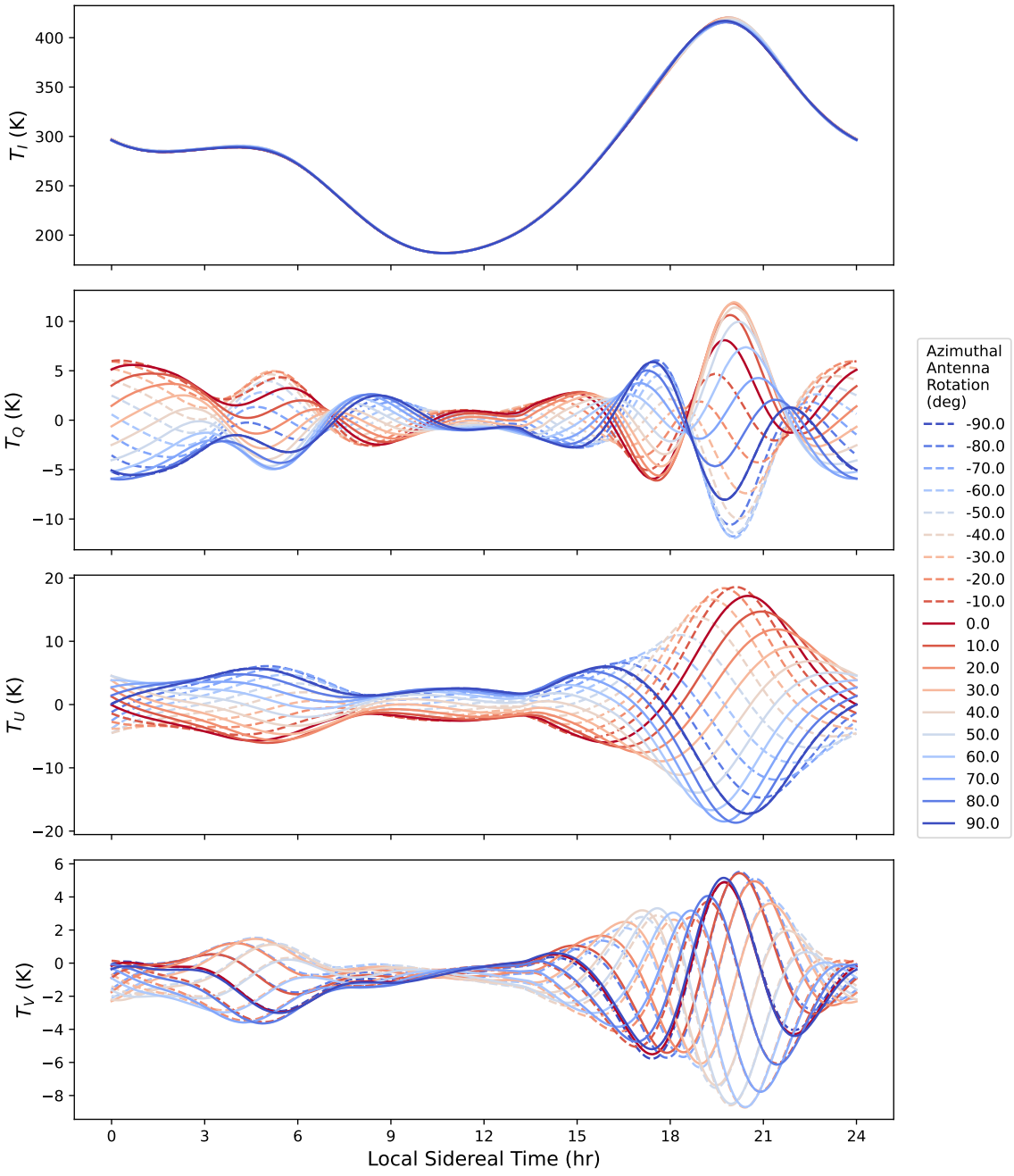

Figure 2.16: HB-CTP Dynamically Induced Polarization Models for varying azimuthal alignments of the antenna with respect to North. Positive angles corresponds to a Eastward rotation from North at 0 degress.

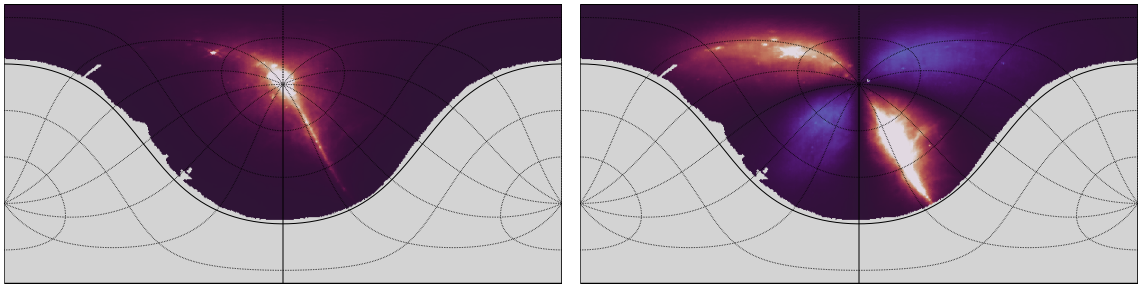

(a) $M_{11}(\theta, \phi; \nu) s_I(\theta, \phi; \nu)$

(c) $M_{33}(\theta, \phi; \nu) s_I(\theta, \phi; \nu)$

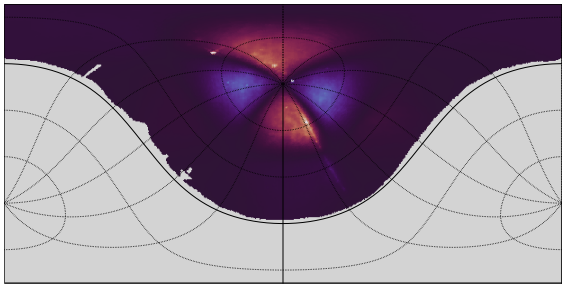

(b) $M_{22}(\theta, \phi; \nu) s_I(\theta, \phi; \nu)$

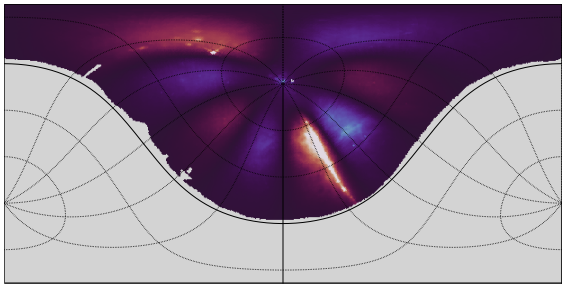

(d) $M_{44}(\theta, \phi; \nu) s_I(\theta, \phi; \nu)$

Figure 2.17: Illustration of the resultant beam-weighted Haslam map using the first column of the CTP antenna Mueller Matrix.

2.4.2 Observational Results

Start Date	Stop Date	Days	Frequency (MHz)	Antenna Azimuth
2019-11-14	2019-11-25	11	164-174	$\sim 0°$E
2019-11-25	2020-03-10	76	164-174	$\sim 20°$E

Table 2.2: HB-CTP Summary of Observation

The long-term observation campaign with the High-Band Cosmic Twilight Polarimeter lasted from November 14th, 2019, through March 10th, 2020, at Green Bank Observatory, operating continuously until scheduled maintence at GBO and the COVID-19 lockdown. The data were continuously monitored for the first week and showed clear signatures of dynamically-induced polarization features. To verify this, the antenna was physically rotated approximately 20° Eastward, about 11 days after first light (see Figure 2.18). This would be the final configuration for the remaining observation time, in order to monitor seasonal-variations and stability.

The comparison between the two different azimuthal alignments of the antenna is qualitatively in agreement with the predicted shift in polarization features. This is especially evident in Stokes U and V, which rely on the cross-correlation of X and Y polarizations that decorrelates the independently generated receiver noise. However, Stokes Q, being the difference of the X and Y polarizations auto-correlations (see Equation 2.23), is more suceptible to unacounted-for instrumental systematic errors and imbalances.

The long-term dataset (with the antenna rotated 20° Eastward) shows that the observed polarization signals are persistent in local sidereal time over roughly 3 months spanning the winter months of 2019-2020. This indicates that the signals are of astrophysical origin. Again, the polarization features are most persistent in Stokes U and V, while Stokes Q is more variable. This long-term dataset also highlights the general cluttered RFI environment, with RFI signals dependent on solar time, visible as a linear feature of flagged data drifting between 15-21 hr LST (corresponding to approximately 4 PM local time) in the dataset.

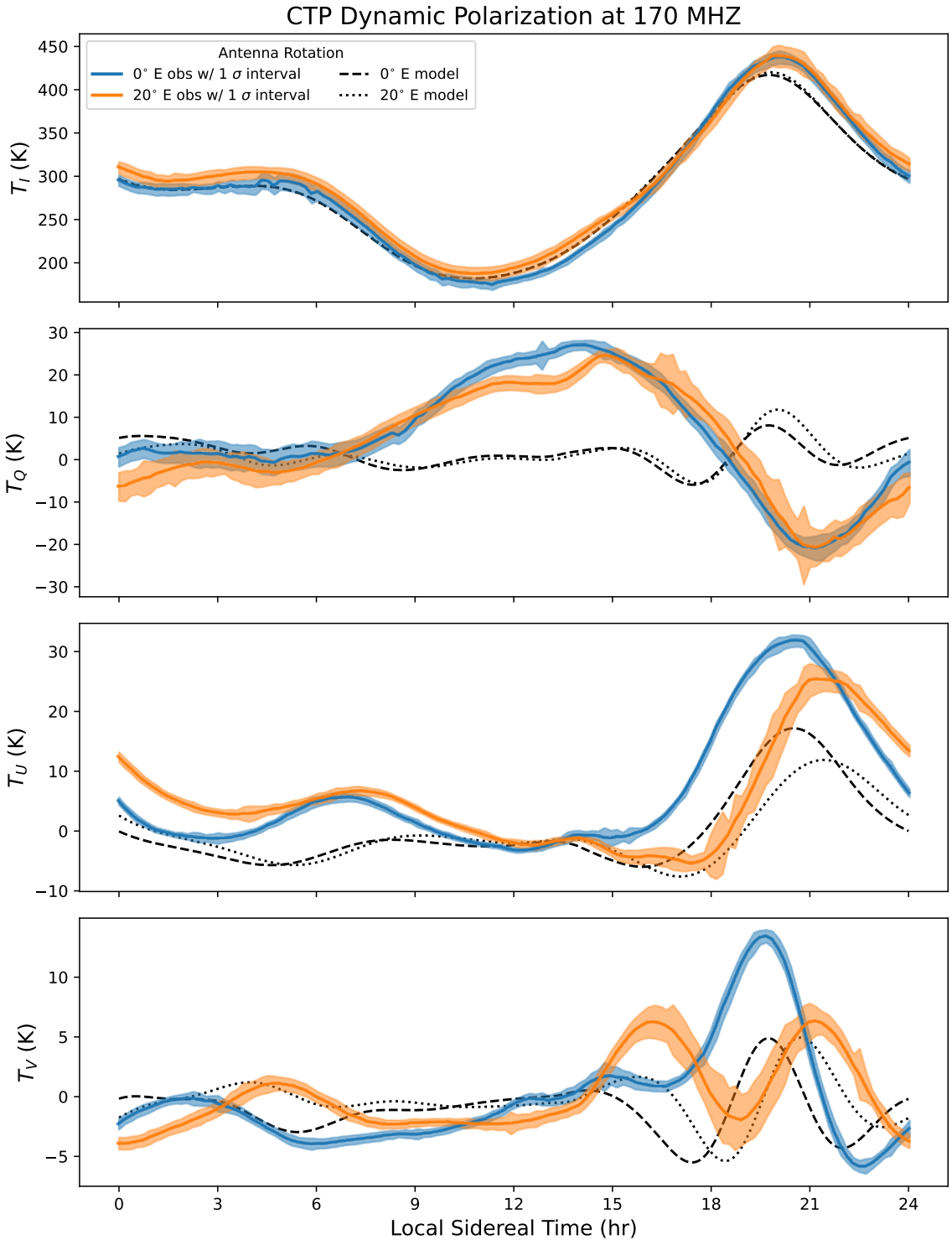

Figure 2.18: HB-CTP Short-Term Observed Dynamically Induced Polarization with Model. (one week of integrated data for each configuration)

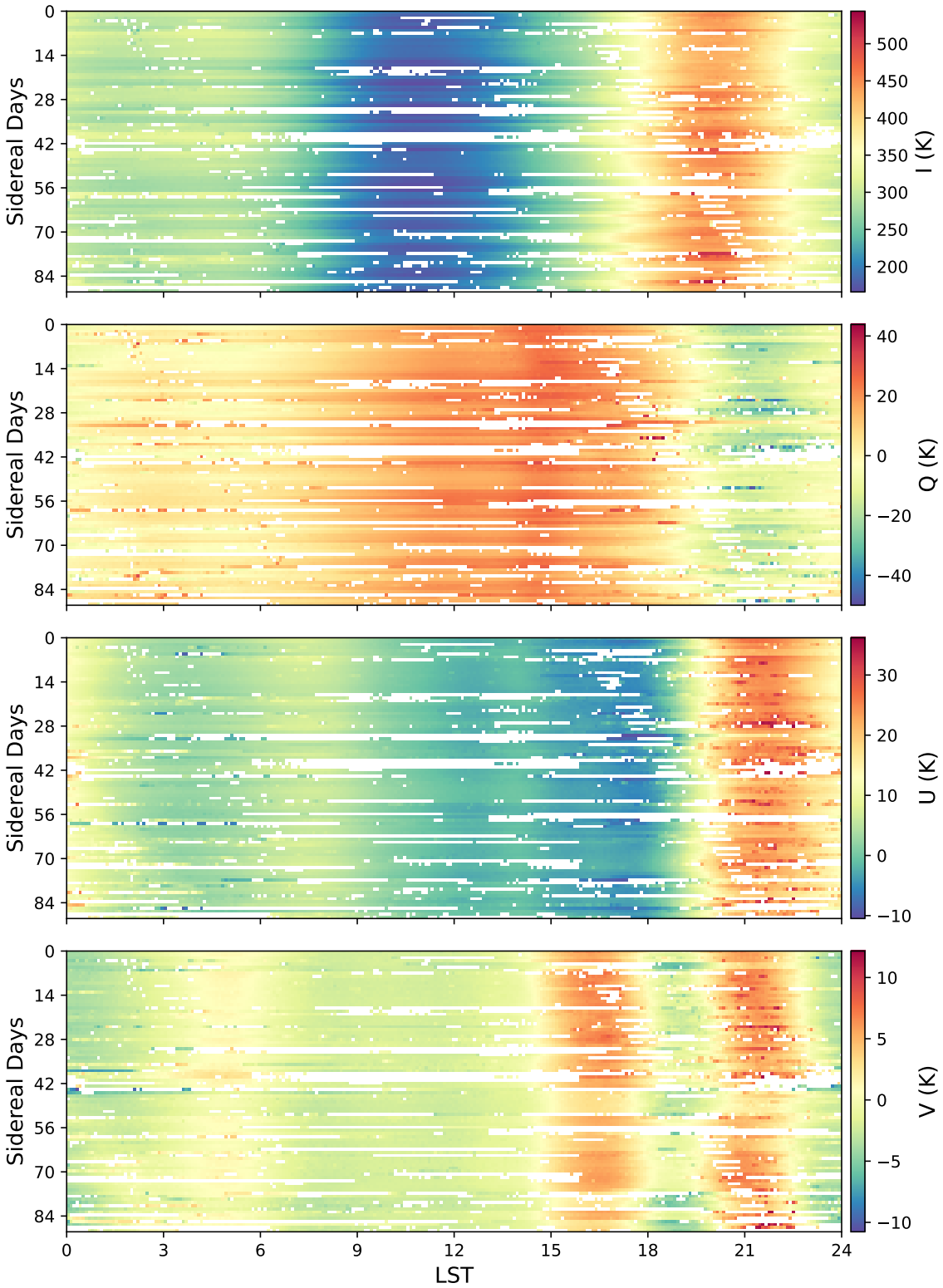

Figure 2.19: HB-CTP Long-Term Observed Dynamically Induced Polarization

2.5 Discussion and Conclusions

In this chapter, I continued the development of the Dynamically Induced Polarization effect, a novel polarimetric observation method that can encode spatially dependent information in the polarization response of wide-beam antenna measurements of the sky (Nhan et al., 2017, 2019). We have extended the theoretical formalism from Jones to Mueller calculus (Piepmeier et al., 2008; Born & Wolf, 2019) to directly operate on Stokes vectors and intuitively visualize how each polarization term is sensitive to the spatial structures on the sky. Accompanying theoretical models and simulations support the observational results from long-term zenith driftscans with the High-Band Cosmic Twilight Polarimeter operating at 170 MHz deployed at Green Bank Observatory.

Although the HB-CTP was built from existing hardware not intended for absolute measurements, long-term observations over nearly 90 days were stable and showed self-constitency, which implies that the lab-characterized gain calibration model and RFI excision was largely effective at reducing large-scale instrumental variations and contamination. Additionally, the observed polarization features qualitatively agree with the predicted DIP signal and follows the expected behavior under perturbations. However, there are still significant deviations in the observed versus predicted response that point towards several possible confounding issues (that may not be mutually exclusive):

(i.) Instrument calibrations are incorrect. This is very likely due to the distributed nature of the instrument, which could not be fully through calibrated in the field. However, the results over a 3 month period show little variation in the observed signal (i.e., deviations are not tied to solar-time/temperature), which would suggest that if there are gain and receiver noise calibration errors, then they are mostly a constant effect and largely invariant in time.

(ii.) The beam simulations may be incorrect or altered by the coupling with the environment. This is also very likely because the soil and nearby dielectric/metallic structures could distort or otherwise interact with the antenna near-field to create spurious polarization responses. However, it is unclear how this could effect only the antenna's Stokes Q polarization leakage and not Stokes U and V while the system is physically perturbed, which would otherwise change the nature of the environmental coupling.

(iii.) Radio propagation effects are insufficiently modeled or missing. This is also very likely, but there are no significant variations observed in solar-time that would suggest that propagation effects are not significant sources of these deviations (at the few percent level). Additionally, since most atmospheric effects are approximately symmetric about the local zenith vector and are proportional to the air-mass (stronger effect close to the horizon), they would primarily scale up or down but not strongly distort the DIP curves, because the polarization leakage is also symmetric (see Figure 2.1). Tropospheric propagation effects are largely stable at these frequencies, however the day/night ionospheric conditions typically change electron/ion densities by a factor of 10 or more, which would significantly alter the associated radio propagation effects (refraction, absorption, and emission). Such strong variations are not observed in the data(Kelley, 2009; Budden, 1988), however.

(iv.) The reference sky map may be incorrect or missing sky polarization information. This is also very likely since the simulations primarily used the Haslam map scaled by a spectral index ($\beta = 2.5$). While multi-wavelength sky models exist, the disparate instruments used (e.g., interferometers versus single-dish) are sensitive to different spatial features on the sky, or may not be absolutely calibrated, which makes inferring the spectral index difficult. Alternatively, the linear polarization from synchrotron radiation from diffuse and optically thin emission regions (e.g., away from the Galactic plane) may retain polarization over larger angular scales, such as in the Fan Region and the North Polar Spur (West et al., 2021; Pacholczyk, 1970). This could explain the significant deviations in Stokes Q when it is pointing away from the Galactic plane around 12 hrs LST, considering the Stokes Q to I polarization leakage (see M_{12} Mueller Matrix element in Figure 2.1).

While this experiment was only able to qualitatively confirm the effects of dynamically induced polarization, it highlighted important gaps in our modeling and understanding of the system, relevant to all global 21-cm experiments. In particular, the polarization of the diffuse radio sky at low-frequencies may be a driving factor in the observed deviations that we have observed in Stokes Q, which would also leak into Stokes I measurements. This illustrates the strength of full-polarimetric measurements in 21-cm cosmology, because the polarization response is able to resolve certain features that total power measurements would be incapable of, providing extra information that can be used to constratin the beam-weighted foreground system. Further work on the CTP was therefore postponed in early 2020, with efforts focused

instead on related work: the Dark Ages Polarimeter Pathfinder (DAPPER; PI – J. Burns CU Boulder), which was a conceptual design study for a global 21-cm experiment orbiting around the moon using the same polarimetric approach; and the GBT 310 MHz Absolute Mapping Project (PI – J. Singal UR, see Chapters 3 and 4).

(a) Surveying the local horizon

(b) Deploying backend in the GBO 45'-Telescope Trailer

Figure 2.20: HB-CTP Deployment and Testing

Chapter 3

Balanced Correlation Receivers

> Low-frequency or $1/f$ noise has several unique properties. If it were not such a problem it would be very interesting.
>
> Mochtenbacher et al., 1993, p. 25

3.1 Introduction

A fundamental challenge in precision radiometry is maintaining long-term stability of the measurement system. In practice, the output of a radiometer will be the sum of the input signal (e.g., the antenna temperature T_A) and a variety of self-generated additive (e.g., thermal noise) and parametric (e.g., flicker (1/f) noise, shot noise, or drift due to temperature or DC bias voltage) sources. Not only do these additional noise contributions reduce the instantaneous *signal to noise ratio* (SNR) of the measurement, they also introduce a mechanism of instability that degrades the ultimate sensitivity, or lowest detectible temperature, of the observation due to the statistical properties of the noise process.

Receiver instability commonly manifests itself as correlated or $1/f$ like fluctuations. Such noise is characterized as a nonstationary random process with the inverse frequency dependence of its power spectral density, so that the variance of the noise distribution is only finite over finite spans of time (Keshner, 1982). Consequently,

once the measurement system is dominated by $1/f$ noise, the central limit theorem no longer holds, thus causing the uncertainty of the measurement to increase over time. Although the mechanisms that produce $1/f$ noise are poorly understood, it is ubiquitous throughout nature including electrical components, biology, weather, and climate to name a few (Keshner, 1982). For electronics, a common source is flicker noise, which is found in all active devices (e.g., diodes, transistors), and even some passive devices such as carbon resistors. This noise is parametrically dependent on the flow of direct current, and its underlying mechanism is believed to be caused by the discrete charge carriers (the electrons) getting trapped by impurities or defects in the crystal lattice and then released in a random fashion with some time constant (Gray, 2001; Motchenbacher & Connelly, 1993). This process results in a concentration of energy at low frequencies, giving rise to the inverse frequency dependence in the power spectral density.

Several methods were conceived in the 1940s to minimize receiver instability using switching or correlation-like approaches to remove or otherwise supress the $1/f$ fluctuations. A technique still widely used today was first introduced by Dicke (1946), which uses a switch at the input of the first amplifier to rapidly toggle between the antenna and a reference noise source. Gain instabilities are suppressed by switching between the reference and target source faster than the receiver can drift in gain (i.e., the $1/f$-knee frequency) and then taking the difference between these two quantities with a synchronous receiver. Because the gain fluctuations are negligible between successive measurements, the continuous differencing process allows the reference source to act as a stable anchor point for the target measurement at the expense of half the sensitivity (as the target is only observed half of the time). The *Dicke receiver* approach saw various improvements and modifications over the following decades (e.g., gain-modulation receiver Orhaug & Waltman (1963), or null-balancing receiver Machin et al. (1952)), but all require some form of input switching.

Correlation approaches were also conceived of during this time period, following naturally from the development of the first radio intereferometers. These methods rely on two separate receiver branches, each fed by a separate arm of an interferometer, or by splitting the output of a single antenna whose outputs are then multiplied together instead of summing/differencing. This operation will supress the independent/uncorrelated receiver noise from each branch, while retaining correlated or common signals. Although such an approach is fundamental to the operation of all

modern radio interferometers, it is rarely employed by single-dish telescopes due to the technical challenges of signal isolation Kraus & Tiuri (1966) and phase stability Fujimoto (1964). While the implementation and adoption of single-dish correlation receivers were limited by the technology of their time, they remain a compelling solution for measurements tht require high-stability and precision (low-offsets). This will be the topic for the remainder of this chapter, where we present the theoretical design of a *balanced correlation receiver* (BCR) enabled by modern technology.

In the following sections, we will present the overall design and theory of operation for a balanced correlation receiver, featuring a unique method for synthesizing virtual dipole beams and associated digital polarization synthesis. Expressions for the Stokes antenna temperatures and receiver sensitivity will be compared to conventional total-power receivers.

3.2 Theory of Operation

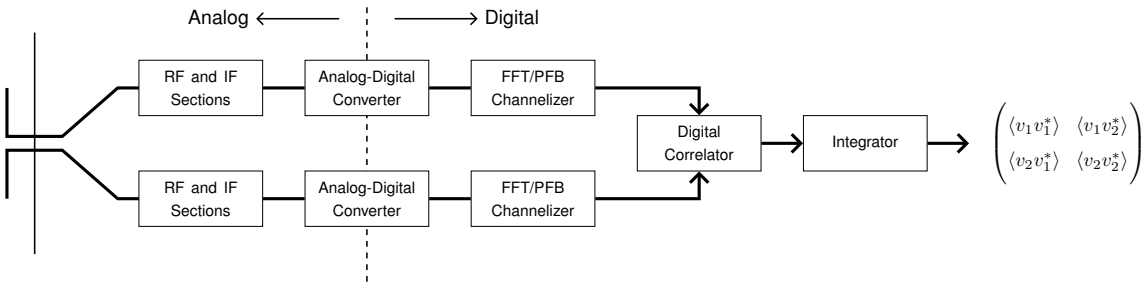

Figure 3.1: A basic Balanced Correlation Receiver

3.2.1 Receiver Architecture

The defining feature of a balanced correlation receiver (BCR) is the unique method used to synthesize the dipole, which allows for maximum isolation of the independent receiver branches (aside from the unavoidable coupling at the feed). As shown in Figure 3.1, the arms of the dipole (on the left) are physically separated and processed by independent RF/IF sections before being digitized and correlated. This dipole synthesis method allows the BCR to remove all shared baluns, transmission lines, hybrid couplers, and RF switches that may be used for typical continuous-differencing receivers (e.g., Dicke switching) or modern pseudo-correlation receivers Bersanelli

et al. (2010). This approach ultimately removes all sources of self-generated noise that would be coherent and therefore contribute to the system noise floor (e.g., an calibration offset).

3.2.2 Synthesis of Virtual Dipole Beams

We start the analysis of a balanced correlation receiver by considering the field solutions of an ideal and split half-wave dipole. As the name suggests, a dipole antenna is composed of two opposing conductors with central feedpoints that approximate the behavior of an electric dipole. The dipole is the foundation for all other radiating structures, and their behavior can be analytically determined directly from the conductor geometry and the current distribution on the conductors. These systems operate in three general regimes: electrically short ($L << \lambda$), resonant ($L \approx \lambda/2$), and harmonic ($L > \lambda$). We will focus on the resonant dipoles, which are of most practical interest since the reactive/imaginary-component of their radiation resistance can be readily tuned out, thereby simplifying impedance matching between the antenna and receiver and maximizing power throughput (Kraus, 1988; Stutzman & Thiele, 1998; Jordan & Balmain, 1968).

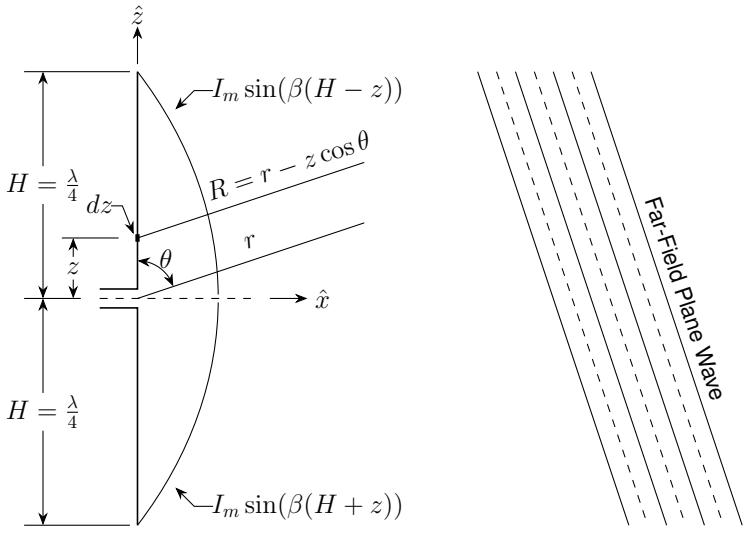

Figure 3.2: Illustration of a half-wave dipole of two thin line current elements on the $\hat{z}$ axis (left). Highlighted are the effective distance from a far-field plane wave (right) on a length segment dz. A sinusoidal current distribution on each arm of the dipole, above and below the xy-plane, are labeled.

Let us begin by defining the geometry of the ideal half-wave dipole and applying some general assumptions of the nature of the induced currents. The dipole shall be formed by two line conductors (monopoles) on the z-axis that are symmetrically distributed above and below the origin, labeled A and B respectively. Next, we will consider the effects of an incident plane-wave originating from the far-field ($R >> \lambda$), that produces a sinusoidal current distribution on the two conductors due to the sinusoidal nature of the radiating EM field represented by the following pair of equations:

$$\begin{aligned} I^{(A)} &= I_m \sin[\beta(H-z)] \qquad z>0 \\ I^{(B)} &= I_m \sin[\beta(H+z)] \qquad z<0 \end{aligned} \tag{3.1}$$

where I_m is the maximum current flowing through the loop, $\beta = \frac{2\pi}{\lambda}$, and $H = \frac{\lambda}{4}$ for a half-wave dipole or quarter-wave monopole. To determine the electric and magnetic field strength at a point P that is a distance r from the origin and R from a line segment dz on the antenna we must solve for the vector potential. The vector potential at point P due to a line charge Idz is given by

$$\begin{aligned} A_z^{(A)} &= \frac{\mu}{4\pi}\int_0^H \frac{I_m \sin[\beta(H+z)]e^{-i\beta R}}{R}dz \\ A_z^{(B)} &= \frac{\mu}{4\pi}\int_{-H}^0 \frac{I_m \sin[\beta(H-z)]e^{-i\beta R}}{R}dz \end{aligned} \tag{3.2}$$

We may simplify the above expressions by considering the relevant quantities for the far-field. The R in the denominator is approximately the inverse distance factor, so that $R \approx r$, since the length of the dipole is negligible when $\lambda/2 << r$. However, for R in the numerator, the difference between the origin and the line segment distance is important, thus we may write $R \approx r - z\cos\theta$. This simplifies Equations 3.2 to the following form:

$$\begin{aligned} A_z^{(A)} &= \frac{\mu I_m e^{-i\beta r}}{4\pi r}\int_0^H \sin[\beta(H+z)]e^{i\beta z\cos(\theta)}dz \\ A_z^{(B)} &= \frac{\mu I_m e^{-i\beta r}}{4\pi r}\int_{-H}^0 \sin[\beta(H-z)]e^{i\beta z\cos(\theta)}dz \end{aligned} \tag{3.3}$$

Using the integral solution (Stutzman & Thiele, 1998)

$$\int \sin(a+bx)e^{cx}dx = \frac{e^{cx}}{b^2+c^2}[c\sin(a+bx) - b\cos(a+bx)] \tag{3.4}$$

we may write the vector potential for monopole A as

$$\begin{aligned} A_z^{(A)} &= \frac{\mu I_m e^{-i\beta r}}{4\pi r}\left[\frac{e^{i\beta z\cos\theta}}{\beta^2 - \beta^2 cos^2\theta}\left[i\beta\sin\theta\sin(\frac{\pi}{2}-\beta z) - \beta\cos(\frac{\pi}{2}-\beta z)\right]\right]_0^H \\ &= \frac{\mu\beta I_m e^{-i\beta r}}{4\pi r(\beta^2 - \beta^2\cos^2\theta)}\left[e^{i\frac{\pi}{2}\cos\theta} - i\cos\theta\right] \\ &= \frac{\mu I_m e^{-i\beta r}}{4\pi r\beta}\left[\frac{e^{i\frac{\pi}{2}\cos\theta} - i\cos\theta}{\sin^2\theta}\right] \end{aligned} \tag{3.5}$$

Similarly, the vector potential for monopole B is

$$\begin{aligned} A_z^{(B)} &= \frac{\mu I_m e^{-i\beta r}}{4\pi r}\left[\frac{e^{i\beta z cos\theta}}{\beta^2 - \beta^2\cos^2\theta}\left[i\beta\sin\theta\sin(\frac{\pi}{2}+\beta z) + \beta\cos(\frac{\pi}{2}+\beta z)\right]\right]_{-H}^0 \\ &= \frac{\mu\beta I_m e^{-i\beta r}}{4\pi r(\beta^2 - \beta^2\cos^2\theta)}\left[e^{-i\frac{\pi}{2}\cos\theta} + i\cos\theta\right] \\ &= \frac{\mu I_m e^{-i\beta r}}{4\pi r\beta}\left[\frac{e^{-i\frac{\pi}{2}\cos\theta} + i\cos\theta}{\sin^2\theta}\right] \end{aligned} \tag{3.6}$$

We may note that in the far-field approximation, the vector potentials for the two monopoles are the complex conjugate of one another, (i.e., $A_z^{(A)} = A_z^{*(B)}$). We may also verify that the sum of both vector potentials simplifies to the standard half-wave dipole solution,

$$\begin{aligned} A_z^{(Dip)} &= A_z^{(A)} + A_z^{(B)} \\ &= \frac{\mu I_m e^{-i\beta r}}{2\pi r\beta}\left[\frac{e^{i\frac{\pi}{2}\cos\theta} + e^{-i\frac{\pi}{2}\cos\theta}}{sin^2\theta}\right] \\ &= \frac{\mu I_m e^{-i\beta r}}{2\pi r\beta}\left[\frac{\cos(\frac{\pi}{2}\cos\theta)}{sin^2\theta}\right] \end{aligned} \tag{3.7}$$

Since the vector potential is entirely in the z-axis we may determine the magnetic field H_φ and electric field E_θ from the following simplified equations following (Jordan & Balmain, 1968):

$$\mu H_\varphi = -\frac{\partial A_z}{\partial r}\sin\theta \tag{3.8}$$

$$E_\theta = \eta H_\varphi \tag{3.9}$$

where $\eta = \sqrt{\mu/\varepsilon}$ is the intrinsic impedance of the medium (for free space $\eta_0 = 376.7\,\Omega$). Applying Equations 3.8 and 3.9 to the derived vector potentials (Equations 3.5, 3.6, and 3.7) results in the following magnetic and electric fields at the far-field:

$$H_\varphi^{(A)} = \frac{iI_m e^{-i\beta r}}{4\pi r}\left[\frac{e^{i\frac{\pi}{2}\cos\theta} - i\cos\theta}{\sin\theta}\right]; \quad E_\theta^{(A)} = \frac{i\eta I_m e^{-i\beta r}}{4\pi r}\left[\frac{e^{i\frac{\pi}{2}\cos\theta} - i\cos\theta}{\sin\theta}\right] \tag{3.10}$$

$$H_\varphi^{(B)} = \frac{iI_m e^{-i\beta r}}{4\pi r}\left[\frac{e^{-i\frac{\pi}{2}\cos\theta} + i\cos\theta}{\sin\theta}\right]; \quad E_\theta^{(B)} = \frac{i\eta I_m e^{-i\beta r}}{4\pi r}\left[\frac{e^{-i\frac{\pi}{2}\cos\theta} + i\cos\theta}{\sin\theta}\right] \tag{3.11}$$

$$H_\varphi^{(Dip)} = \frac{iI_m e^{-i\beta r}}{2\pi r}\left[\frac{\cos(\frac{\pi}{2}\cos\theta)}{\sin\theta}\right]; \quad E_\theta^{(Dip)} = \frac{i\eta I_m e^{-i\beta r}}{2\pi r}\left[\frac{\cos(\frac{\pi}{2}\cos\theta)}{\sin\theta}\right] \tag{3.12}$$

The complex power density flowing out of a sphere of radius r surrounding the dipole can be computed by the Poynting Vector (Kraus, 1991), defined as

$$\boldsymbol{S} = \boldsymbol{E} \times \boldsymbol{H}^* \tag{3.13}$$

Since the E and H derived in the far-field condition are in-phase and orthogonal, we may simplify the cross-product to

$$\boldsymbol{S} = E_\theta H_\varphi^* \,\hat{\boldsymbol{r}} = \frac{E_\theta E_\theta^*}{\eta}\,\hat{\boldsymbol{r}} \tag{3.14}$$

The Poynting vector is in general complex-valued, where the real component typically corresponds to the far-field radiation and the imaginary/reactive component corresponds to the near-field of the radiating structure. Thus the average radial power is

$$P_{avg} = \frac{1}{2}\boldsymbol{S} \cdot \hat{\boldsymbol{r}} = \frac{E_\theta E_\theta^*}{2\eta} \tag{3.15}$$

Using the equation above, we can now verify that the average power from an ideal dipole is

$$P_{avg}^{(Dip)} = \frac{\eta I_m^2}{8\pi^2 r^2}\left[\frac{\cos^2(\frac{\pi}{2}\cos\theta)}{\sin^2\theta}\right] \tag{3.16}$$

By treating the dipole as two independent monopoles, a balanced-correlation receiver allows us to synthesize two additional virtual beams via the summation of auto or cross-correlation pairs. In the case of the auto-correlated beam, we find that the average far-field power pattern is

$$\begin{aligned} P_{avg}^{(+)} &= \frac{E_\theta^{(A)} E_\theta^{*(A)}}{2\eta} + \frac{E_\theta^{(B)} E_\theta^{*(B)}}{2\eta} = \frac{E_\theta^{(A)} E_\theta^{*(A)}}{\eta} \\ &= \frac{\eta I_m^2}{16\pi^2 r^2}\left[\frac{(e^{i\frac{\pi}{2}\cos\theta} - i\cos\theta)(e^{-i\frac{\pi}{2}\cos\theta} + i\cos\theta)}{\sin^2\theta}\right] \\ &= \frac{\eta I_m^2}{16\pi^2 r^2}\left[\frac{\cos^2\theta - 2\cos\theta\sin(\frac{\pi}{2}\cos\theta) + 1}{\sin^2\theta}\right] \end{aligned} \tag{3.17}$$

Because this process destroys the relative phase information in the system, the gain of the beam will be degraded compared to the ideal half-wave dipole. Furthermore, the receiver noise contribution will be retained because of the auto-correlations, thus leaving this measurement susceptible to the effects of $1/f$ noise.

On the other hand, the cross-correlated beam has significant benefits over both the auto-correlated beam and even the ideal dipole, as it allows for a separation of noise signals. The average far-field power for the cross-correlated beam is given by

$$\begin{aligned} P_{avg}^{(\times)} &= \frac{E_\theta^{(A)} E_\theta^{*(B)}}{2\eta} + \frac{E_\theta^{(B)} E_\theta^{*(A)}}{2\eta} = \mathrm{Re}\left(\frac{E_\theta^{(A)} E_\theta^{*(B)}}{\eta}\right) \\ &= \mathrm{Re}\left(\frac{\eta I_m^2}{16\pi^2 r^2}\left[\frac{(e^{i\frac{\pi}{2}\cos\theta} - i\cos\theta)(e^{i\frac{\pi}{2}\cos\theta} - i\cos\theta)}{\sin^2\theta}\right]\right) \\ &= \mathrm{Re}\left(\frac{\eta I_m^2}{16\pi^2 r^2}\left[\frac{-\cos^2\theta + e^{i\pi\cos\theta} - 2i\cos\theta e^{i\frac{\pi}{2}\cos\theta}}{\sin^2\theta}\right]\right) \\ &= \frac{\eta I_m^2}{16\pi^2 r^2}\left[\frac{-\cos^2\theta + \cos(\pi\cos\theta) + 2\cos\theta\sin(\frac{\pi}{2}\cos\theta)}{\sin^2\theta}\right] \end{aligned} \tag{3.18}$$

Although each of the cross-power pairs, $E_\theta^{(A)} E_\theta^{*(B)}$ and $E_\theta^{(B)} E_\theta^{*(A)}$ are complex-valued, the imaginary components will cancel out due to symmetry, as shown in Figure 3.3. We see that by including the phase information between monopoles, we enhance the effective gain of the system in comparison to the ideal half-wave dipole. Additionally, because the only common signal in both monopole receiver chains will be due to the incident radio wave on the antenna (ignoring radiative cross-coupling), the independent receiver noise will decorrelate when integrated in time. This presents an optimal

radiative system to both reduce the overall noise from the receiver itself, but also to obtain higher spatial resolution compared to traditional antennas synthesized via baluns or other analog means.

Half-wave Dipole Type	*Far-Field Pattern*	*FWHM* (Deg)	*D* (lin.)	*D* (dB)	*R* (Ω)
Ideal	$\frac{\cos^2(\frac{\pi}{2}\cos\theta)}{\sin^2\theta}$	78°	1.64	2.15	73.1
Auto-Correlated Monopoles	$\frac{\cos^2\theta - 2\cos\theta\sin(\frac{\pi}{2}\cos\theta)+1}{\sin^2\theta}$	86°	1.54	1.88	38.9
Cross-Correlated Monopoles	$\frac{-\cos^2\theta+\cos(\pi\cos\theta)+2\cos\theta\sin(\frac{\pi}{2}\cos\theta)}{\sin^2\theta}$	68.4°	1.75	2.44	34.2

Table 3.1: Ideal and virtual dipole properties

3.2.3 Digital Polarization Synthesis

Let us now consider the reception of polarized light through a geometrical analysis of a dually polarized radiating system. The polarization of light refers, by convention, to the relative alignment and phase of the electric field components with respect to some reference frame (Hamaker & Bregman, 1996). Following this convention, we can define a suitable polarized representation for an incident signal as a complex vector in a Cartesian coordinate system:

$$\boldsymbol{e}(t) = \begin{pmatrix} e_x(t) \\ e_y(t) \end{pmatrix} = \begin{pmatrix} a_1(t)e^{i(\phi_1(t)-2\pi\bar{\nu}t)} \\ a_2(t)e^{i(\phi_2(t)-2\pi\bar{\nu}t)} \end{pmatrix} \tag{3.19}$$

In this representation we assume that the direction of propagation is in the $\hat{z}$ direction and thus the electric field $\boldsymbol{e}(t)$ can be decomposed into two mutually orthogonal complex components $e_x(t)$ and $e_y(t)$. If the time-dependent quantities vary slower than the coherence time ($\Delta\tau\Delta\nu \sim \frac{1}{4\pi}$), the quasi-monochromatic limit holds, and the time dependence of the signal can be ignored in practice (Born & Wolf, 2019).

Next, we show how such a complex signal vector is sampled by an ideal detector that transforms fields to measurable scalar quantities. Let us start by considering the

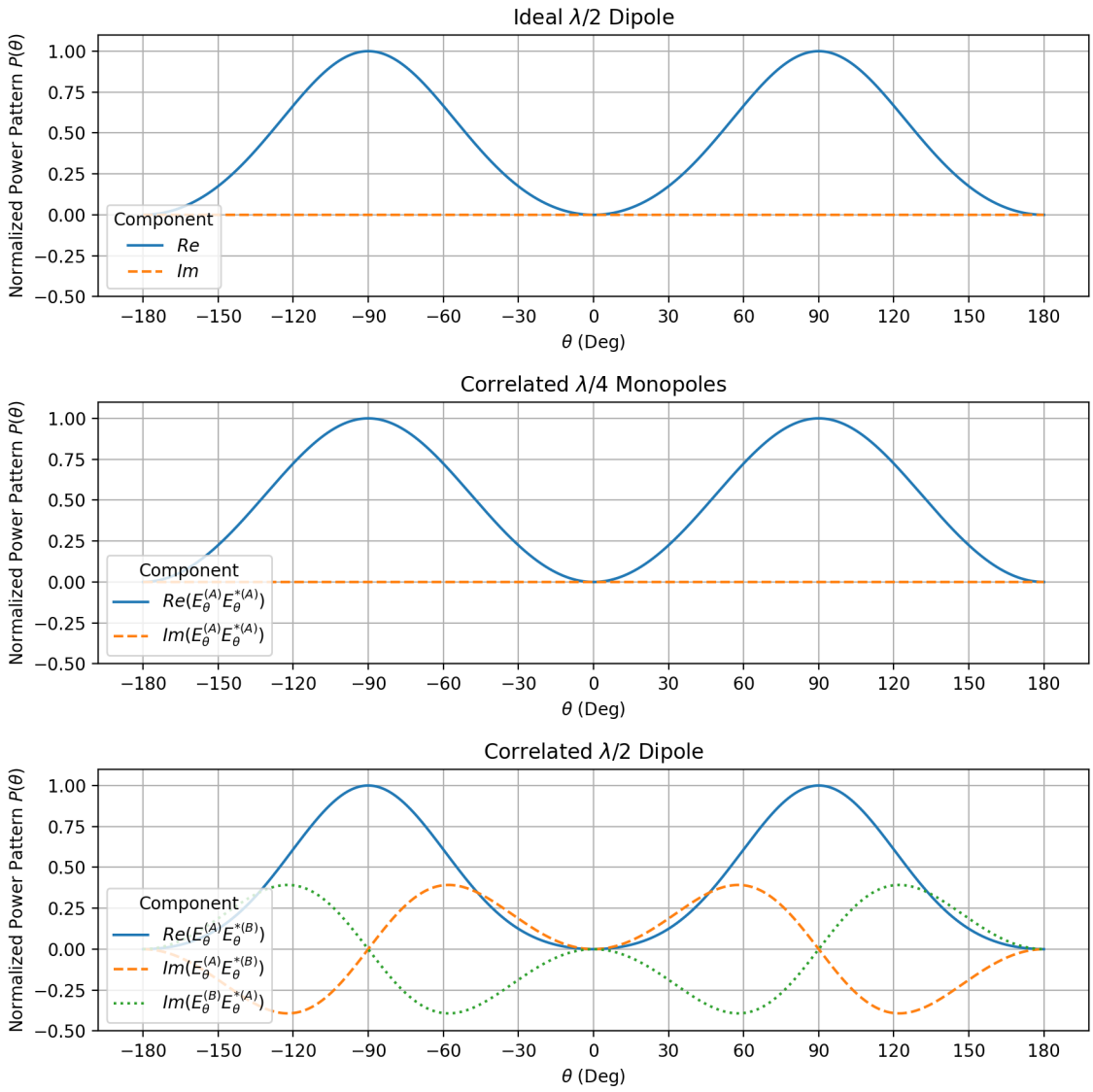

Figure 3.3: Normalized power patterns for the three considered cases: the ideal half-wave dipole, the summation of auto-correlated monopoles, and the summation of cross-correlated monopoles. Note that the imaginary components in the third case are for each pair and would cancel under summation. Each pattern shows a dipole like behavior, however in the case of the auto- and cross-correlated monopoles, we see that the effective beam patterns are slightly broader and narrower, respectively, than the ideal dipole.

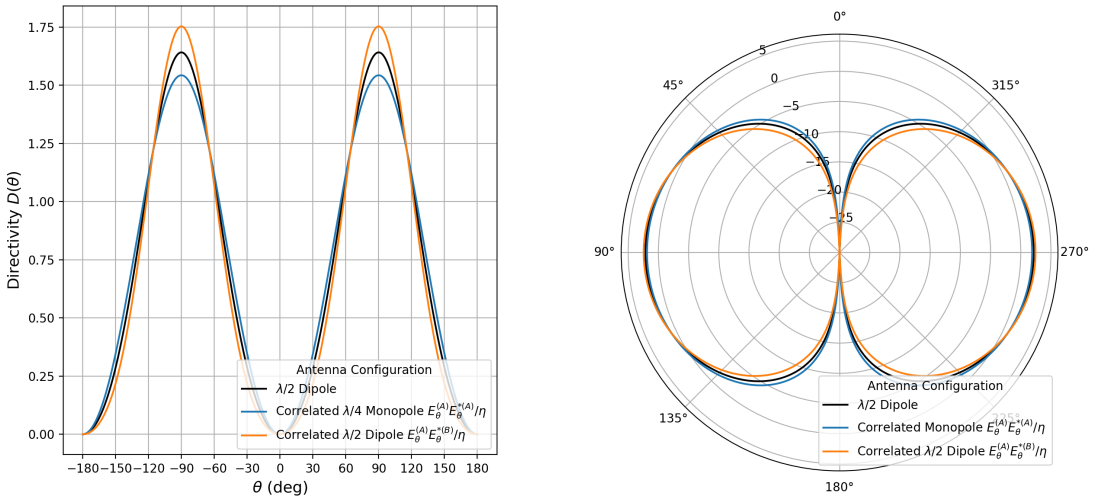

(a) Linear (b) Polar

Figure 3.4: Dipole Directivity Comparison

effect of a single electrical conductor in the presence of an electric field. A voltage will develop along the conductor due to the projection of the electric field (i.e., $V = \boldsymbol{E}\cdot\boldsymbol{L}$). Thus, if the electric field and conductor are aligned, a maximum voltage can be observed. If they are orthogonal, no voltage is observed across the conductor. This is a fundamental principle behind the operation of radiating systems, including the dipoles considered in the previous section. Therefore, dipoles and monopoles are able to sample the electric field, with at least two (ideally orthogonal) probes required to fully determine the polarization of the incident light. The generalized sampling of the field by N probes can be represented by the following generalized equation:

$$\boldsymbol{v}(t) = \boldsymbol{Q}\boldsymbol{e}(t) \tag{3.20}$$

where $\boldsymbol{Q}$ is a $N \times 2$ sampling matrix with physical dimensions of length (m), and $\boldsymbol{v}$ is the electronic signal vector in voltage (V) (Hamaker et al., 1996; Hamaker, 2000; Morgan et al., 2010). The resultant electronic signal vector represents the voltages measured at each port of the detector due to an incident signal.

The sampling of the electric field is a linear operation and retains the coherent properties (e.g., the phase information) of the incident signal. However, in practice, signals are subjected to stochastic processes that result in decoherence (depolariza-

tion) due to variable emission mechanisms or propagation effects, such as turbulence, which changes the polarization over time. To address the partial decoherence of light, we can employ a useful mathematical tool, the coherence matrix, whose elements carry the mutual intensities of the signal components (Born & Wolf, 2019; Hamaker et al., 1996). In our case, the coherence matrix may found by taking the outer product of the electric field vector (our coherent signal):

$$\boldsymbol{C} = \langle \boldsymbol{e}(t)\boldsymbol{e}(t)^{\dagger} \rangle \tag{3.21}$$

where $\langle \ldots \rangle$ denotes an ensemble average and $\dagger$ is the Hermitian transpose. Because the underlying random processes that affect the electric field amplitudes and phases are expected to be statistically stationary and ergodic, we may drop the explicit time dependence by the applied averaging:

$$\boldsymbol{C} = \begin{pmatrix} \langle e_x e_x^* \rangle & \langle e_x e_y^* \rangle \\ \langle e_y e_x^* \rangle & \langle e_y e_y^* \rangle \end{pmatrix} = \begin{pmatrix} \langle a_1^2 \rangle & \langle a_1 a_2 e^{i(\phi_1 - \phi_2)} \rangle \\ \langle a_1 a_2 e^{-i(\phi_1 - \phi_2)} \rangle & \langle a_2^2 \rangle \end{pmatrix} \tag{3.22}$$

Another useful mathematical construct are the Stokes parameters, an abstract representation of the total intensity and polarization state of light. By definition, the coherence matrix can be constructed with the four Stokes Paramters (I, Q, U, and V), providing the following equivalent representations (Hamaker, 2000):

$$\boldsymbol{C} = \begin{pmatrix} I + Q & U - iV \\ U + iV & I - Q \end{pmatrix} = s_I \boldsymbol{\sigma_0} + s_Q \boldsymbol{\sigma_1} + s_U \boldsymbol{\sigma_2} + s_V \boldsymbol{\sigma_3} \tag{3.23}$$

where σ_n is the identity matrix ($n = 0$) and the Pauli spin matrices for ($n = 1, 2, 3$):

$$\boldsymbol{\sigma}_0 = \begin{pmatrix} 1 & 0 \\ 0 & 1 \end{pmatrix} \quad \boldsymbol{\sigma}_1 = \begin{pmatrix} 1 & 0 \\ 0 & -1 \end{pmatrix} \quad \boldsymbol{\sigma}_2 = \begin{pmatrix} 0 & 1 \\ 1 & 0 \end{pmatrix} \quad \boldsymbol{\sigma}_3 = \begin{pmatrix} 0 & -i \\ i & 0 \end{pmatrix} \tag{3.24}$$

Thus, the Stokes vector representation of light can be determined from the coherency matrix using the following equation:

$$\boldsymbol{s}_\mu = \mathrm{tr}(\boldsymbol{\sigma}_\mu \boldsymbol{C}). \tag{3.25}$$

However, Electric fields cannot be measured directly in practice; instead voltage

potentials induced by a local field are observed. Thus, it is useful to rewrite Equation 3.21 in terms of voltages by substituting in Equation 3.20:

$$\boldsymbol{C} = \langle \boldsymbol{e}\boldsymbol{e}^{\dagger} \rangle \tag{3.26}$$

$$= \langle (\boldsymbol{Q}^{-1}\boldsymbol{v})(\boldsymbol{Q}^{-1}\boldsymbol{v})^{\dagger} \rangle \tag{3.27}$$

$$= \boldsymbol{Q}^{-1} \langle \boldsymbol{v}\boldsymbol{v}^{\dagger} \rangle (\boldsymbol{Q}^{-1})^{\dagger} \tag{3.28}$$

$$= \boldsymbol{A}\boldsymbol{M}\boldsymbol{A}^{\dagger} \tag{3.29}$$

For clarity, $\langle \ldots \rangle$ signs are dropped and terms are consolidated into a measurement matrix $\boldsymbol{M} = \langle \boldsymbol{v}\boldsymbol{v}^{\dagger} \rangle$, and the inverse sampling matrix $\boldsymbol{A} = \boldsymbol{Q}^{-1}$. The measurement matrix is a natural output from conventional FX-correlators used in radio polarimeters, where time-series of voltages are first channelized in frequency and then auto/cross-correlated and accumulated over an integration period.

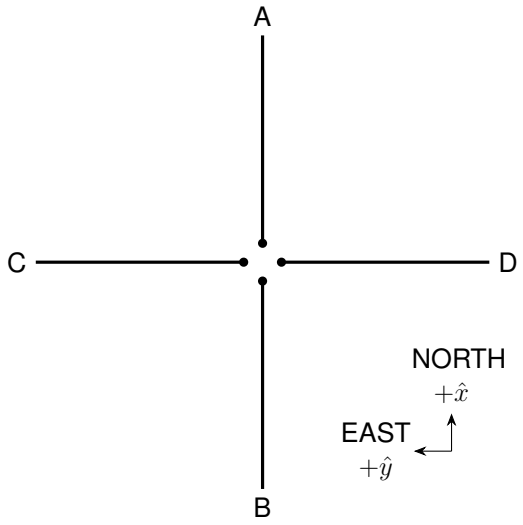

Figure 3.5: Illustration of a crossed dipole

Ideal Cross-Dipole

Using an ideal cross-dipole as the first example, we can further develop the mathematical methods required to quantify partially-polarized light. The cross-dipole is composed of two orthogonal dipoles along the $\hat{x}$ and $\hat{y}$ axes. If we assume this system

has unit gain, we can represent the sampling matrix as a square 2×2 Jones matrix:

$$\boldsymbol{Q}^{(2)} = \begin{pmatrix} 1 & 0 \\ 0 & 1 \end{pmatrix} \tag{3.30}$$

Because $\boldsymbol{Q}^{(2)}$ is a square non-singular matrix, it has a well defined inverse. Additionally, our selection of basis means that $\boldsymbol{Q}^{(2)}$ is the identity matrix; thus, the trivial solution for the inverse is $\boldsymbol{Q}^{-1} = \boldsymbol{Q} = \boldsymbol{I}$. The measurement matrix, on the other hand, is the outer product of the observed voltage vector:

$$\boldsymbol{M}^{(2)} = \langle \boldsymbol{v}\boldsymbol{v}^{\dagger} \rangle = \begin{pmatrix} \langle v_x v_x^* \rangle & \langle v_x v_y^* \rangle \\ \langle v_y v_x^* \rangle & \langle v_y v_y^* \rangle \end{pmatrix} \tag{3.31}$$

From this, the coherence matrix can be computed using Equation 3.29:

$$\boldsymbol{C}^{(2)} = \boldsymbol{I}\boldsymbol{M}^{(2)}\boldsymbol{I}^{\dagger} = \boldsymbol{M}^{(2)} \tag{3.32}$$

Using Equation 3.25, the Stokes parameters in terms of complex voltages can then be computed:

$$\boldsymbol{s}^{(2)} = \begin{pmatrix} s_I \\ s_Q \\ s_U \\ s_V \end{pmatrix} = \begin{pmatrix} \langle v_x v_x^* \rangle + \langle v_y v_y^* \rangle \\ \langle v_x v_x^* \rangle - \langle v_y v_y^* \rangle \\ \langle v_x v_y^* \rangle + \langle v_y v_x^* \rangle \\ i(\langle v_x v_y^* \rangle + \langle v_y v_x^* \rangle) \end{pmatrix} \tag{3.33}$$

where $\boldsymbol{s}^{(2)}$ is the conventional solution for the Stokes vector from a linear measurement basis.

Ideal Digitally Synthesized Cross-Dipole

Let us now consider a radiating system that supports the synthesis of the virtual auto- and cross-correlated beams, as discussed in Section 3.2.2. The construction of this radiating system is identical to the ideal cross-dipole case, however we are now sampling each arm of the dipoles independently, which results in 4 independent

probes, each with half the original amplitude:

$$\boldsymbol{Q}^{(4)} = \begin{pmatrix} \frac{1}{2} & 0 \\ -\frac{1}{2} & 0 \\ 0 & \frac{1}{2} \\ 0 & -\frac{1}{2} \end{pmatrix} \tag{3.34}$$

Because the sampling matrix is not square, the inverse required to compute the coherency matrix cannot be directly computed. However, since we have an overdetermined system of equations due to the pair of redundant probes, we can make use of the Moore-Penrose pseudoinverse (Penrose, 1955; Haykin, 1996). In the case of a $K \times M$ matrix where $N > M$ with rank W equal to M, the pseudoinverse may be expressed as

$$\boldsymbol{A}^{+} = (\boldsymbol{Q}^{T}\boldsymbol{Q})^{-1}\boldsymbol{Q}^{T} \tag{3.35}$$

where the pseudoinverse provides the least-squares solution to Equation 3.20:

$$\boldsymbol{v}(t) = \boldsymbol{A}^{+}\boldsymbol{e}(t) \tag{3.36}$$

$$\boldsymbol{A}^{+(4)} = \begin{pmatrix} 1 & -1 & 0 & 0 \\ 0 & 0 & 1 & -1 \end{pmatrix} \tag{3.37}$$

Next we define the observed measurement matrix:

$$\boldsymbol{M}^{(4)} = \begin{pmatrix} M_{11} & M_{12} & M_{13} & M_{14} \\ M_{21} & M_{22} & M_{23} & M_{24} \\ M_{31} & M_{32} & M_{33} & M_{34} \\ M_{41} & M_{42} & M_{43} & M_{44} \end{pmatrix} \tag{3.38}$$

where

$$M_{ij} = (\boldsymbol{v}_i \boldsymbol{v}_j^{\dagger})_{ij} \tag{3.39}$$

By construction, we have a symmetrical system of two redundant orthogonal pairs, each capable of forming an effective dipole when following the approach described in Section 3.2.2. We can therefore apply the same method for forming the virtual auto/cross-correlated beams of a single dipole to a system of two orthogonal dipoles. This is achieved by treating the auto- and cross-correlated terms separately, and

representing the measurement matrix as the following sum:

$$\boldsymbol{M}^{(4)} = \boldsymbol{M}_A^{(4)} + \boldsymbol{M}_X^{(4)} \tag{3.40}$$

where the auto-correlated component matrix is

$$\boldsymbol{M}_A = \begin{pmatrix} M_{11} & 0 & 0 & 0 \\ 0 & M_{22} & 0 & 0 \\ 0 & 0 & M_{33} & 0 \\ 0 & 0 & 0 & M_{44} \end{pmatrix} \tag{3.41}$$

Similarly the cross-correlation only component matrix is

$$\boldsymbol{M}_X = \begin{pmatrix} 0 & M_{12} & M_{12} & M_{14} \\ M_{21} & 0 & M_{23} & M_{24} \\ M_{31} & M_{32} & 0 & M_{34} \\ M_{41} & M_{42} & M_{43} & 0 \end{pmatrix} \tag{3.42}$$

From these two separate datasets, we can determine the corresponding coherency matrix for both the auto- and cross-correlated monopole pairs. Performing this step is equivalent to Equations 3.17 and 3.18, through which the virtual auto- and cross-correlated beams can be synthesized, respectively. For the auto-correlated case the coherency matrix will be

$$\begin{aligned} \boldsymbol{C}_A^{(4)} &= \boldsymbol{A}^{(4)} \boldsymbol{M}_A^{(4)} (\boldsymbol{A}^{(4)})^\dagger \\ &= \begin{pmatrix} M_{11} + M_{22} & 0 \\ 0 & M_{33} + M_{44} \end{pmatrix} \end{aligned} \tag{3.43}$$

with associated Stokes parameters via Equation 3.25:

$$\boldsymbol{s}_A^{(4)} = \begin{pmatrix} M_{11} + M_{22} + M_{33} + M_{44} \\ M_{11} + M_{22} - M_{33} - M_{44} \\ 0 \\ 0 \end{pmatrix} \tag{3.44}$$

Because all phase information is lost due to the auto-correlation of signals, we can

only partially reconstruct the incident Stokes vector. However, there remains enough information to form both $\hat{x}-\hat{y}$ auto-correlated dipoles, recovering half of the incident total power (Stokes I) and linear 0 and 90° polarization (Stokes Q) signal.

Next, we synthesize the virtual cross-correlated beam response, following the same process as before to determine the coherency matrix:

$$\begin{aligned}\boldsymbol{C}_X^{(4)} &= \boldsymbol{A}^{(4)}\boldsymbol{M}_X^{(4)}(\boldsymbol{A}^{(4)})^\dagger \\ &= \begin{pmatrix} -M_{12}-M_{21} & M_{13}-M_{32}-M_{14}+M_{24} \\ M_{31}-M_{23}-M_{41}+M_{42} & -M_{34}-M_{43} \end{pmatrix}\end{aligned} \tag{3.45}$$

and associated Stoke parameters:

$$\begin{aligned}\boldsymbol{s}_X^{(4)} &= \begin{pmatrix} -M_{12}-M_{21}-M_{34}-M_{43} \\ -M_{12}-M_{21}+M_{34}+M_{43} \\ M_{13}-M_{32}-M_{14}+M_{24}+M_{31}-M_{23}-M_{41}+M_{42} \\ i(M_{13}-M_{32}-M_{14}+M_{24}-M_{31}+M_{23}+M_{41}-M_{42}) \end{pmatrix} \\ &= 2\begin{pmatrix} Re(-M_{12}-M_{34}) \\ Re(-M_{12}+M_{34}) \\ Re(M_{13}-M_{14}-M_{23}+M_{24}) \\ Im(M_{13}-M_{14}-M_{23}+M_{24}) \end{pmatrix}\end{aligned} \tag{3.46}$$

Because the cross-correlations retain all of the relative phase information between pairs of antennas and can sample both orthogonal basis directions, we maintain sensitivity to all Stokes parameters. Inspecting the resultant Stokes vector, $\boldsymbol{s}_X^{(4)}$, we find that we recover the other half of Stokes I and Q, and all of Stokes U and V (linear ±45° and circular polarization).

3.2.4 Radiation Resistance and Feedline Structures

Next, we shall consider the required feedline structure required to support the balanced correlation receiver approach. As we have shown from the field analysis in the prior section, an antenna transforms electromagnetic waves propagating in free-space (photons) to guided-waves (currents) and vice versa. As such, an antenna shares properties of both a transmission line with a characteristic impedance, and as a resonator where energy is stored in the surrounding reactive near-field (Kraus, 1988). If

we consider the antenna as an open-ended transmission line, the antenna will appear as a two-terminal circuit with some characteristic impedance. This is the radiation resistance, or the effective impedance of a lossless resistor that relates the applied maximum current to the radiated power. Thus, an antenna can also be considered as an impedance transformer that efficiently converts the impedance of free-space to an effective resistance at the antenna feedpoints (Kraus, 1988).

To efficiently transfer power to and from the antenna, we much match the source impedance of the antenna feedpoints to the load impedance of the connected receiver. In practice, this is accomplished with a balun (BALanced-to-UNbalanced) circuit, which is used to synthesize the antenna beam and also transform the impedance to the system impedance (commonly 50Ω). However, because we want to maintain the independence of the two monopoles, we seperately transform the impedances of each branch, as if the system was an ideal $\lambda/4$ monopole over a ground plane. For example, a center-tapped transformer, with each winding pair having a ratio of $1 : \sqrt{2}$, will convert the ideal monopole impedance ($Z_A = 36.5\Omega$) to approximately $Z_L = 50\Omega$, as shown in Figure 3.7b. However, transformers tend to be lossy components due to the material properties of their cores. Alternatively, transmission line tapered impedance transformers could be used to gradually transition the input and output impedance. For instance, a Klopfenstein tapered transmission line would provide an optimal approach (Klopfenstein, 1956; Pozar, 2012).

Following Jordan & Balmain (1968), the total root-mean-square power transmitted or received by the antenna is

$$P_{rms} = Z_A(I_m/\sqrt{2})^2 = \oint P_{rad} d\Omega \tag{3.47}$$

where P_{rad} is the average radiated power pattern as in Equations 3.16, 3.17, and 3.18, integrated over the surface of a large sphere in the far-field. Rearanging terms and solving for Z_A provides the following expression:

$$Z_A = \frac{2}{I_m^2} \oint P_{rad} d\Omega \tag{3.48}$$

By numerical integration of Equation 3.48, the radiation resistance for the possible

dipole beams can be computed. For the ideal dipole,

$$Z_A^{(dip)} = \frac{\eta}{2\pi}\int_0^{\pi}\left[\frac{\cos^2(\frac{\pi}{2}\cos\theta)}{\sin\theta}\right]d\theta \approx \frac{\eta}{2\pi}[1.219] \approx 73.1\Omega \tag{3.49}$$

the auto-correlated virtual dipole,

$$Z_A^{(+)} = \frac{\eta}{4\pi}\int_0^{\pi}\left[\frac{\cos^2\theta - 2\cos\theta\sin(\frac{\pi}{2}\cos\theta) + 1}{\sin\theta}\right]d\theta \approx \frac{\eta}{4\pi}[1.297] \approx 38.9\Omega \tag{3.50}$$

and finally the cross-correlated virtual dipole,

$$\begin{aligned} Z_A^{(\times)} &= \frac{\eta}{4\pi}\int_0^{\pi}\left[\frac{-\cos^2\theta + \cos(\pi\cos\theta) + 2\cos\theta\sin(\frac{\pi}{2}\cos\theta)}{\sin\theta}\right]d\theta \\ &\approx \frac{\eta}{4\pi}[1.141] \approx 34.2\Omega \end{aligned} \tag{3.51}$$

The above calculations assumed that the characteristic impedance of the medium η is that of a vaccuum:

$$\eta_0 = \sqrt{\mu_0/\varepsilon_0} \approx 376.7\,\Omega \tag{3.52}$$

where μ_0 and ϵ_0 are the magnetic permeability and electric polarizability of a vacuum, respectively. However, this value is a close approximation for waves propagating in air as well.

We find that the radiation resistances of the two virtual dipoles are approximately half of the ideal $\lambda/2$ dipole impedance. From image theory, we can recognize that this is the solution for the ideal $\lambda/4$ monopole over an infinite groundplane (Jordan & Balmain, 1968; Stutzman & Thiele, 1998). However, we can instead consider the virtually synthesized dipoles as two monopoles between a virtual ground axis, as this configuration no longer needs an infinite groundplane to form the image monopole.

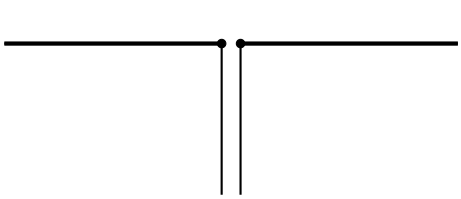

(a) Dipole

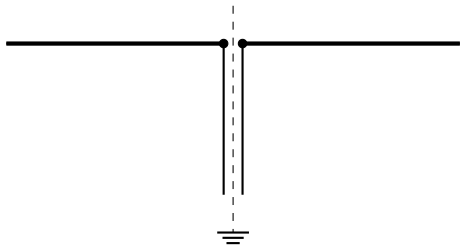

(b) Virtual Dipole

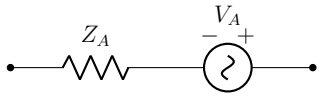

(c) Dipole Equivalent Circuit

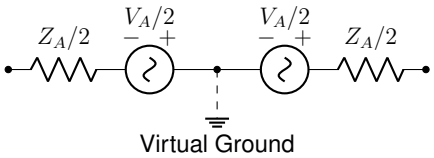

(d) Virtual Dipole Equivalent Circuit

Figure 3.6: Dipole equivalent circuits

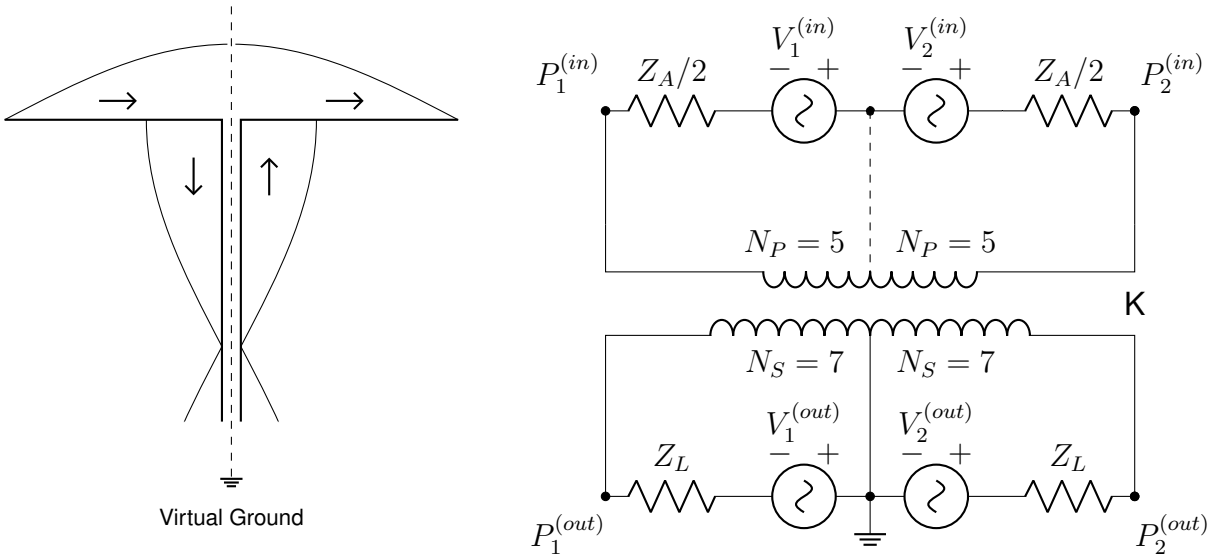

(a) Balanced Feedline Structure

(b) Balun Equivalent Circuit

Figure 3.7: Balanced Correlation Receiver Feedline Currents and Equivalent Balun Circuit

3.3 Sensitivity of A Balanced Correlation Radiometer

The sensitivity of a radio telescope is limited by the fluctuations of the output from the self-generated noise of the radiometer and its statistical characteristics. The total system noise power per unit bandwidth, $W_{sys} = k_B T_{sys}$, which is instantaneously present at the output of the receiver, will be the sum of the antenna W_A and receiver W_R spectral noise powers. Thus, when the receiver output is followed by an ideal integrator, the sensitivity, or standard deviation σ_{sys}, of the system noise can be improved following the ideal-radiometer equation (Kraus & Tiuri, 1966):

$$\sigma_{sys} = \gamma \frac{T_{sys}}{\sqrt{\tau \Delta\nu}} \tag{3.53}$$

where γ is a factor near unity based on the system design, τ is the integration time (typically on order of 0.1-100s of seconds), and $\Delta\nu$ is the signal bandwidth (e.g., the resolution bandwidth of an FX-correlator).

The ideal-radiometer equation assumes that the gain of the radiometer is absolutely stable, however this is not the case in general. Receiver gain fluctuations tend to exhibit a $1/f$-noise characteristics that are driven by both intrinsic (e.g., device flicker or burst noise) and extrinsic (e.g., power supply and temperature fluctuations) effects, which can be mathematically represented as:

$$\frac{\Delta G}{G} = \frac{K_1}{\nu^{\alpha}} \tag{3.54}$$

where K_1 is a constant factor dependent on the system, and $\alpha \approx 1$ (Keshner, 1982; Gray, 2001). The gain fluctations are statistically independent and uncorrelated from the receiver noise, thus their associated variance will simply add ($\sigma_{sys}^2 = \sigma_r^2 + \sigma_g^2$). This leads to the practical total-power radiometer equation:

$$\sigma_{sys} \approx T_{sys}\left[\frac{1}{\sqrt{\tau\Delta\nu}} + \left(\frac{\Delta G}{G}\right)^2\right]^{1/2} \tag{3.55}$$

As a consequence of the $1/f$-noise like gain fluctuations, integrating slower than the ""$1/f - knee$" frequency f_k, where $\sigma_r = \sigma_g$, will cause increased receiver output fluctuations as the central limit theorem breaks down in the $1/f$-noise dominated regime (Kraus & Tiuri, 1966; Pacholczyk, 1970; Condon & Ransom, 2016).

The balanced correlation receiver is an improved version of the conventional correlation receiver. While the conventional design splits the output of a single antenna into two independent receiver branches using power splitters or hybrid junctions, the balanced correlation receiver uses the feed itself to split the incident signal into two independent balanced signals without any shared circuitry that could contribute correlated noise (see Figure 3.8).

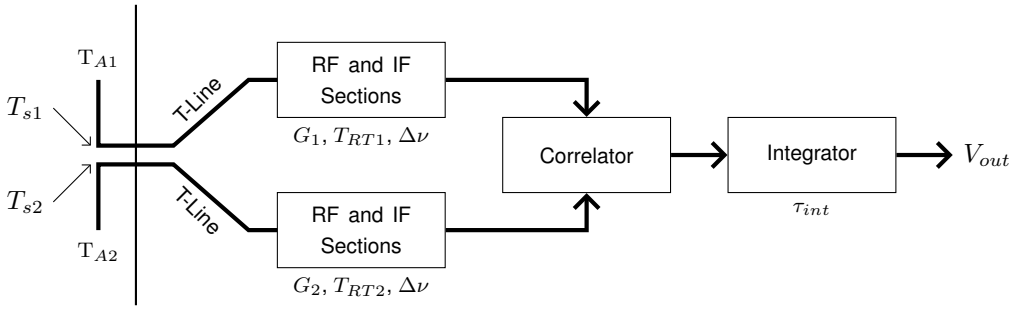

Figure 3.8: Annotated Balanced Correlation Receiver

The two branch system temperatures ($T_{s1} = T_{A1} + T_{RT1}$ and $T_{s2} = T_{A2} + T_{RT2}$) contain both the correlated sky noise component ($T_A = T_{s1} - T_{s2}$, where $|T_s|/2 = |T_A|$), and the statistically independent and uncorrelated noise from the receiver and transmission lines (T_{RT1} and T_{RT2}). Taking the product (or cross-correlation) of these two branches will lead to an average value of zero for any statistically uncorrelated component, while the correlated signal remains:

$$\begin{aligned}\langle T_{sys}\rangle &= (\langle T_{s1}T^*_{s2}\rangle)^{1/2} \\ &= (\langle T_{A1}T^*_{A2}\rangle + \langle T_{A1}T^*_{RT2}\rangle + \langle T_{RT1}T^*_{A2}\rangle + \langle CT_{RT1}T^*_{RT2}\rangle)^{1/2} \\ &= (\langle T_{A1}T^*_{A2}\rangle + \langle CT_{RT1}T^*_{RT2}\rangle)^{1/2} \\ &= \frac{\langle T_A\rangle}{2}, \quad \text{if} \quad C = 0\end{aligned} \tag{3.56}$$

where C is the correlation coefficient between self-generated receiver noise components that ranges from $-1 < C < 1$, with $C = 0$ being totally uncorrelated. This implies that the sensitivity of the balanced correlation receiver is not limited by gain instabilies if the receiver noise contributions are uncorrelated ($C = 0$). In this limit, the sensitivity will be the same as a conventional correlation receiver (Kraus & Tiuri, 1966),

$$\sigma_{sys} = \frac{2T_{sys}}{\sqrt{2\tau\Delta\nu}} = \sqrt{2}\frac{T_{sys}}{\sqrt{\tau\Delta\nu}} \tag{3.57}$$

where $\gamma = \sqrt{2}$ due the power splitting between antenna elements. However, the observed antenna noise temperature from a balanced correlation receiver will have negligible additive self-generated noise compared to the standard correlation receiver (see Figure 3.9). This is due to the construction of the balanced correlation receiver which removes correlated instrumental noise contributions from shared lossy transmission lines or power splitters compared to the standard correlation receiver.

As an example of the balanced correlation receiver, we can look at the performance of the GBT 310 MHz receiver (see Chapter 4). The observed noise power spectral density of the thermaly stabilized GBT310 receiver shows that the auto-correlated signals are dominated by $1/f$ at integration times of about $\tau_k \approx 1$ minute. However, the cross-correlated channels show no discernible $1/f$ contributions to the maximum integration tested ($\tau_{max} \approx 36$ hrs), implying that the isolation of the receiver channels is sufficent to prevent the self-generated receiver noise from correlating.

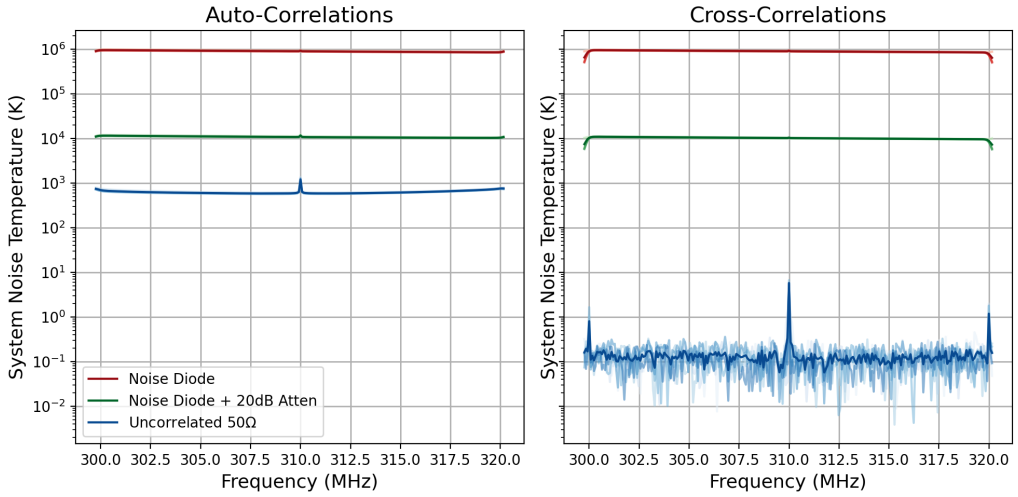

Figure 3.9: Comparison of average system noise temperature from the GBT310 MHz balanced correlation receiver with 3 different noise inputs (2 internal noise diode states and a 300K termination) with 5 minute integrations ($T_{RT} \approx 200$ K).

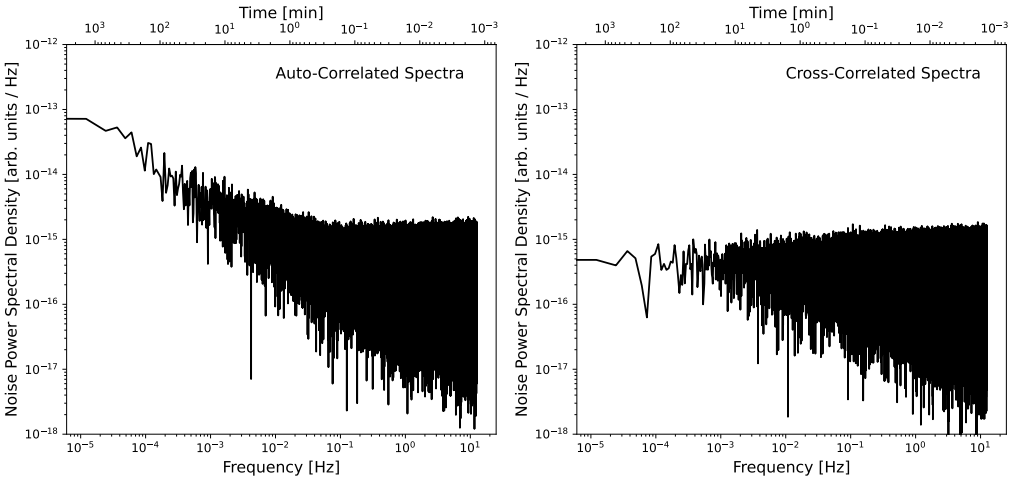

Figure 3.10: Noise Power Spectral Density of the GBT 310 MHz frontend receiver with inputs independently terminated ($T_{A1} = T_{A2} \approx 300$K). (Left) shows a single auto-correlated channel (e.g., a total-power receiver) that is influenced by $1/f - noise$. (Right) shows the cross-correlation of two channels (e.g., a correlation receiver) that shows no discernible correlated $1/f$ component below the minimum frequency tested ($f_{min} \approx 10^{-5}$ Hz)

The Stokes antenna temperatures can be found by recasting the observed output measurement matrix $\boldsymbol{M}$ from Section 3.2.3 into input referenced temperatures before applying Equation 3.29 and 3.25, using the branch transducer gains g_i and receiver noise temperatures T_i^N:

$$\boldsymbol{M}^{(in,T)} = \frac{1}{k_b Z_L \Delta\nu} \boldsymbol{G} \boldsymbol{M}^{(out)} \boldsymbol{G}^{\dagger} - \boldsymbol{T}^N \tag{3.58}$$

where k_b is the Boltzman constant, Z_L is the system impedance (typ. 50Ω), and $\Delta\nu$ is the channel resolution, along with the diagonal inverse gain matrix:

$$\boldsymbol{G} = \text{diag}(\sqrt{g_1}, ..., \sqrt{g_n})^{-1} \tag{3.59}$$

where elements g_i are the transducer gains for each branch following Pozar (2012):

$$g_i = \frac{(1 - |\Gamma_{src}|^2)(1 - |\Gamma_{load}|^2)|S_{21}|^2}{|(1 - S_{11}\Gamma_{src})(1 - S_{22}\Gamma_{load}) - S_{21}S_{21}\Gamma_{src}\Gamma_{load}|^2} \tag{3.60}$$

and the additive diagonal matrix of the branch receiver noise:

$$\boldsymbol{T}_N = \text{diag}(T_1^N, ..., T_n^N) \tag{3.61}$$

Results of the Stokes antenna temperatures for the three different configurations considered in the previous sections are shown in the following Table 3.2:

Type	Stokes Antenna Temperature (K)
Ideal Dipole	$T_I = \frac{1}{Z_L k_B \Delta\nu}\big[\frac{\langle v_1 v_1^*\rangle}{\sqrt{g_1 g_1^*}} + \frac{\langle v_2 v_2^*\rangle}{\sqrt{g_2 g_2^*}}\big] - (T_1^N + T_2^N)$ $T_Q = \frac{1}{Z_L k_B \Delta\nu}\big[\frac{\langle v_1 v_1^*\rangle}{\sqrt{g_1 g_1^*}} - \frac{\langle v_2 v_2^*\rangle}{\sqrt{g_2 g_2^*}}\big] - (T_1^N - T_2^N)$ $T_U = \frac{2}{Z_L k_B \Delta\nu}\mathrm{Re}\big[\frac{\langle v_1 v_2^*\rangle}{\sqrt{g_1 g_2^*}}\big]$ $T_V = \frac{2}{Z_L k_B \Delta\nu}\mathrm{Im}\big[\frac{\langle v_1 v_2^*\rangle}{\sqrt{g_1 g_2^*}}\big]$
Auto-Correlated Dipole (BCR)	$T_I = \frac{1}{Z_L k_B \Delta\nu}\big[\frac{\langle v_1 v_1^*\rangle}{\sqrt{g_1 g_1^*}} + \frac{\langle v_2 v_2^*\rangle}{\sqrt{g_2 g_2^*}} + \frac{\langle v_3 v_3^*\rangle}{\sqrt{g_3 g_3^*}} + \frac{\langle v_4 v_4^*\rangle}{\sqrt{g_4 g_4^*}}\big]$ $- (T_1^N + T_2^N + T_3^N + T_4^N)$ $T_Q = \frac{1}{Z_L k_B \Delta\nu}\big[\frac{\langle v_1 v_1^*\rangle}{\sqrt{g_1 g_1^*}} + \frac{\langle v_2 v_2^*\rangle}{\sqrt{g_2 g_2^*}} - \frac{\langle v_3 v_3^*\rangle}{\sqrt{g_3 g_3^*}} - \frac{\langle v_4 v_4^*\rangle}{\sqrt{g_4 g_4^*}}\big]$ $- (T_1^N + T_2^N - T_3^N - T_4^N)$ $T_U = 0$ $T_V = 0$
Cross-Correlated Dipole (BCR)	$T_I = \frac{1}{Z_L k_B \Delta\nu}\mathrm{Re}\big[-\frac{\langle v_1 v_2^*\rangle}{\sqrt{g_1 g_2^*}} - \frac{\langle v_3 v_4^*\rangle}{\sqrt{g_3 g_4^*}}\big]$ $T_Q = \frac{1}{Z_L k_B \Delta\nu}\mathrm{Re}\big[-\frac{\langle v_1 v_2^*\rangle}{\sqrt{g_1 g_2^*}} + \frac{\langle v_3 v_4^*\rangle}{\sqrt{g_3 g_4^*}}\big]$ $T_U = \frac{1}{Z_L k_B \Delta\nu}\mathrm{Re}\big[\frac{\langle v_1 v_3^*\rangle}{\sqrt{g_1 g_3^*}} - \frac{\langle v_3 v_2^*\rangle}{\sqrt{g_3 g_2^*}} - \frac{\langle v_1 v_4^*\rangle}{\sqrt{g_1 g_4^*}} + \frac{\langle v_2 v_4^*\rangle}{\sqrt{g_2 g_4^*}}\big]$ $T_V = \frac{1}{Z_L k_B \Delta\nu}\mathrm{Im}\big[\frac{\langle v_1 v_3^*\rangle}{\sqrt{g_1 g_3^*}} - \frac{\langle v_3 v_2^*\rangle}{\sqrt{g_3 g_2^*}} - \frac{\langle v_1 v_4^*\rangle}{\sqrt{g_1 g_4^*}} + \frac{\langle v_2 v_4^*\rangle}{\sqrt{g_2 g_4^*}}\big]$

Table 3.2: BCR Stokes Antenna Temperature

3.4 Discussion and Conclusions

In this work, I presented the theoretical operation of the balanced correlation receiver (BCR), a novel design that relies only on cross-correlations between redundant-in-polarization E-field probes (e.g., the balanced output from two monopole arms of a dipole) to digitally synthesize the beam of a dipole antenna and suppress receiver gain instabilities. This unique way of synthesizing a dipole beam avoids the shared circuitry ahead of the receiver such as the balun that forms the antenna itself, transmission lines, and powersplitters or hybrid junctions used to split the signal into the two receiver branches of a traditional correlation receiver. As such, the BCR maximizes the isolation of the independent receiver branches, and minimizes the con-

tribution of self-genereated correlated noise that would otherwise contribute to the receiver noise-floor. This theoretically allows a BCR to have exceptional long-term receiver gain stability (decorrelation of $1/f$ noise) and also minimal offsets in the averaged system noise temperature (no auto-correlation of signals).

Supporting the BCR is an analysis of a digitally synthesized beam from the balanced outputs of a dipole. This showed that when treating the monopoles of a dipole seperately, three different beams can be synthesized from the sum of voltage products: a lower-gain dipole beam from auto-correlated monopoles, a higher-gain dipole beam from cross-correlated monopoles, and when combined these beams simplify to the ideal dipole case. Thus, if monopoles can be individually digitized, then specific beams can be formed by choosing the required sum of auto or cross-correlation pairs. Furthermore, this directly supports the functionality of a correlation receiver when only considering the cross-correlations of monopoles. This analysis was also extended to the treatment of a cross-dipole and digital polarization synthesis, which showed full Stokes polarimetry is possible with only cross-correlation pairs as well. Thus, the poarlimetric output from a BCR will be unbiased by additive receiver noise temperature contributions since the correlation of statistically independent noise terms (i.e., the self-generated receiver noise of each branch) has an expectation value of zero.

Finally, the sensitivity of a balanced correlation receiver was considered, and it shows that the BCR follows the expected ideal radiometer equation for a correlation-receiver if the correlation coeficient between independent noise terms are zero. Therefore the BCR can remove effects of self-generated $1/f$-like receiver gain-fluctuations if isolation can be ensured. However, this implies the main limitation of the system, the finite isolation and coupling through the feed and feedlines, and also the superposition of multiple coherent signals at the input. Additionally, since a BCR does not use a balun, common-mode signals present in the feed are not rejected and therefore could overpower the desired differential-mode signal on the dipoles (e.g., from coaxial-modes within the feed structure, or strong sources of RFI). Furthermore are reflections from the antenna and receiver interface, which could create time-delayed echos that would cause decoherence.

The unique properties of a Balanced Correlation Receiver make it well suited for measurements requiring high-stability and precision. However, the instrument must be carefully designed to ensure high-isolation, and to suppress common or even-modes within the feed of the system.

Chapter 4

A 310 MHz Absolute Map

4.1 Introduction

An emergent astrophysical question is the origin of the bright radio synchrotron background, which exceeds the total brightness produced by known source populations and emission mechanisms (Singal et al., 2018, 2023). The radio background emission below $\nu \sim 0.5$GHz is dominated by steep-spectrum synchrotron radiation from integrated extragalactic sources, in addition to the fainter CMB emission $T_{CMB} \approx 2.7$ K (Planck Collaboration et al., 2016) that only begins to dominate at higher-frequencies ($\nu > 3$ GHz). The background synchrotron spectrum was determined by Dowell & Taylor (2018), using 40-80 MHz LWA measurements (Taylor et al., 2012) and 3-90 GHz ARCADE 2 spectra (Fixsen et al., 2011; Singal et al., 2011), as the following power law (scaled to our instrument's operating frequency of 310 MHz):

$$T_B(K) = 24.1 \pm 2.1\,\mathrm{K}\left(\frac{\nu}{310\mathrm{MHz}}\right)^{-2.6\pm0.04} \tag{4.1}$$

However, current counts of extragalactic radio sources only account for one-fifth of this brigthness (Condon et al., 2012). This may point towards a hypothetical, new population of faint extragalactic sources, more numerous than all known galaxies (Vernstrom et al., 2014; Condon et al., 2012; Tasse et al., 2021). Other possible contributing sources of diffuse extragalactic radio emission have also been suggested, such as cluster mergers (Fang & Linden, 2016), intergalactic dark matter decays and annihilations (Hooper et al., 2012), and population III supernovae (Biermann

et al., 2014). Alternatively, a galactic synchrotron halo has been proposed, which could explain the emission (Subrahmanyan & Cowsik, 2013; Orlando, 2018). This is generally not supported by current observations (Singal et al., 2015, 2010; Fornengo et al., 2014), however.

Furthermore, large-area, absolutely calibrated, zero-level maps of the diffuse radio emission are essential in the study of the CMB and HI 21-cm experiments, which both require accurate models and templates of forground structure. The current gold-standard, low-frequency map is the Haslam 408 MHz map (Haslam et al., 1981), however absolute zero-level calibration was not its primary goal. It instead relied on cross-calibration with overlaping measurements from decade prior (Pauliny-Toth & Shakeshaft, 1962). Thus, a new low-frequency map with full-Stokes polarization that is from the ground-up and designed for absolute calibrations is vital in reducing systematic errors (e.g., spatially varying spectral indices and intrinsic foreground polarization).

However, low-frequency radio surveys that report absolute brightnesses (e.g., Roger et al. (1999); Maeda et al. (1999); Dowell & Taylor (2018); Haslam et al. (1981); Reich & Reich (1986); Tello et al. (2013); Jonas et al. (1998)) ultimately derive their zero-level calibration from dipoles and old measurements prone to systematic uncertainties (e.g., Pauliny-Toth & Shakeshaft (1962); Howell & Shakeshaft (1966); Bersanelli et al. (1994)). This motivated the creation of a new low-frequency radio sky map, purpose-built for absolute calibration.

4.2 Observation Requirements and Strategies

The Green Bank Telescope (GBT), with its large 100-m unblocked aperture, is the ideal platform for creating this new and improved low-frequency, absolutely calibrated, zero-level map of the northern hemisphere. Using a basket-weave observation strategy (see Figure 4.1), errors due to antenna spillover, atmospheric opacity, and emission can be limited by performing a series of constant-in-elevation azimuth sweeps (between -5° to 365° at a scanning rate of $30^\circ\,\mathrm{min}^{-1}$) that pass through the NCP at 38.44°. Additional tipping scans can be used to constrain the current atmospheric opacity along with covering lower declinations possible than with the azimuth scans alone. However, preliminary observations taken during the summer of 2018 (award

GBT18A-483 — PI: J. Singal) have revealed that the current low-frequency Prime Focus 1 (PF1) feed and receiver are not well suited for this task, primarily due to gain instability and high antenna spillover, as PF1 was optimized for point-source sensitivity. Furthermore, the output power spectrum of the PF1 receiver is dominated by $1/f$ noise for all $f \lesssim 4$ Hz, which would cause significant drift during the 15-minute azimuth scanning interval between repeat measurements of the NCP. This highlighted the need for a purpose-built, 310 MHz receiver system (GBT310), specifically optimized for continuum mapping at the lowest practical frequencies ($\sim$300 MHz) achievable with the GBT.

To achieve the maximum scientific utility of this map, the uncertainty in the absolute zero-level must be limited to less than 5 K. The total uncertainty of the system is the quadrature sum of uncertainties in the following quantites: receiver noise temperature, spillover and ground pickup, and atmospheric absorption and emission. Atmospheric effects are well-charactized for Green Bank Observatory, and while the effective contibution is on the order of several K (dependent on elevation), the uncertainties are typically below 1 K. The spillover can be limited to less than 3 K by using a custom high edge-taper feed that underilluminates the GBT dish. This leaves ~ 4 K for the uncertainty in the receiver noise temperature, the details of which are the subject of the rest of this chapter.

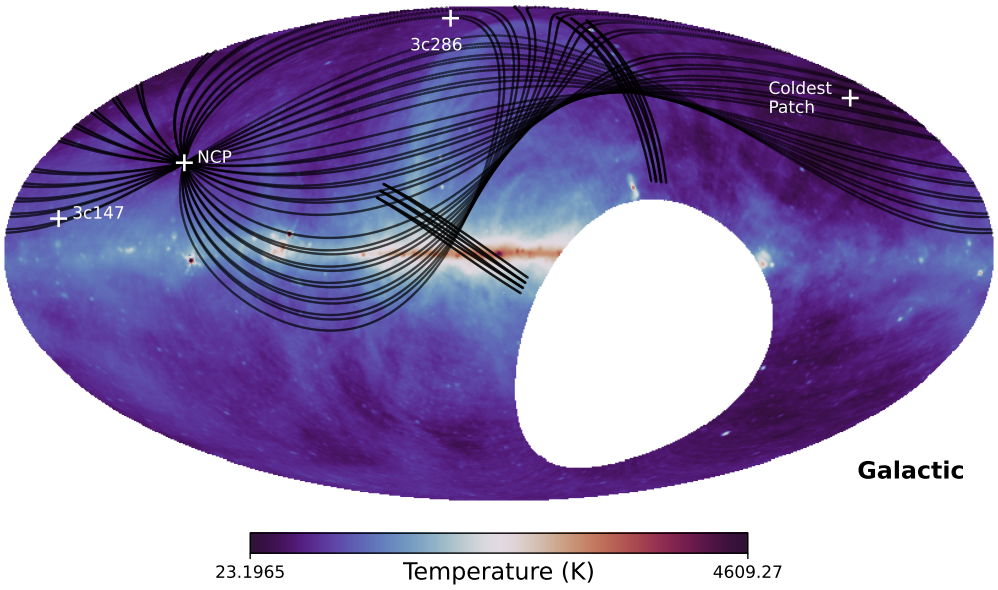

(a) Annotated sky with basket-weave and tip-scan observation traces

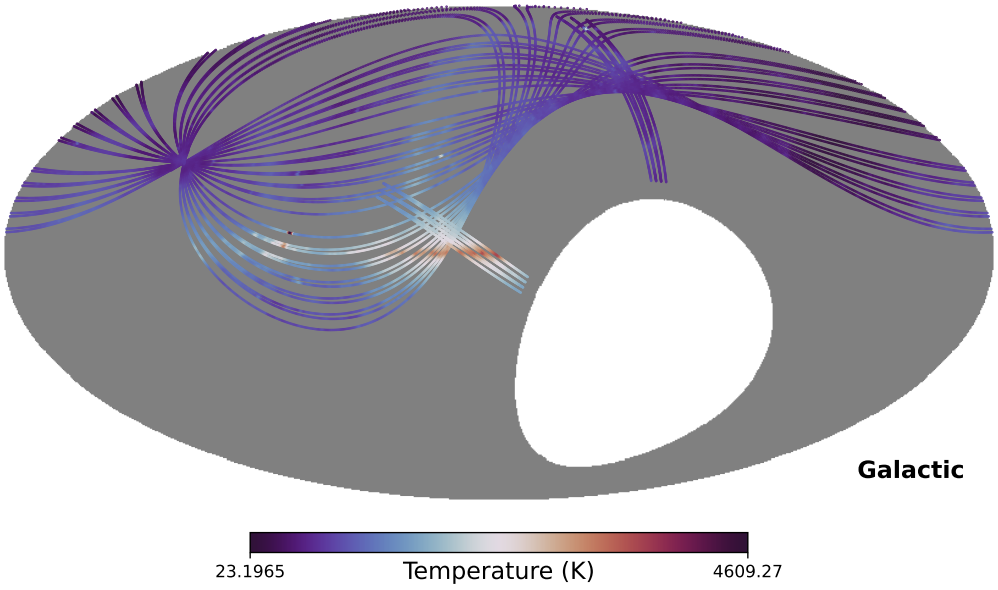

(b) Resultant sky coverage for one observation

Figure 4.1: Example of a single Basket-Weave observation (observing on April 15th). Measurements consist of constant elevation(48°) azimuth scans crossing through the NCP, along with tipping-scans to reach lower declination angles and for atmospheric opacity corrections.

4.3 The GBT 310 MHz Balanced Correlation Receiver

The GBT310 receiver makes use of a novel balanced correlation receiver (BCR) design that synthesizes the beam directly from cross-correlations of the balanced output of the feed. This correlation approach allows for the suppression of receiver gain instabilities, because the $1/f$ noise from each receiver branch is statistically independent and will therefore decorrelate on average. Additionally, a custom high-edge taper feed with low side/back-lobes is required for the BCR approach and to underilluminate the GBT dish.

The conceptual design of the GBT310 began in late 2018 with the general goal of rapidly fielding a capable, yet expedient instrument. Key technological efforts were identified to meet the observational goals of the survey, along with finding practical limitations that also needed to be solved (i.e., the required feed is too large to fit within the prime-focus shelter of the GBT). Thus, a quick experiment soon dragged on for many years during the unprecedented times of the COVID-19 pandemic. The scope of work was broken up as follows:

- **Electromagnetic Feed Design** – Design of a custom 310 MHz high-edge taper feed based on a Short Backfire Antenna (SBA) led by: Bang Nhan, Krishna Makhija, Sivasankaran Srikanth.
- **Mechanical Feed Design** – Design of a modular and lightweight feed with crumple-zones led by: David Bordenave, Art Symms
- **Frontend Receiver Design** – Low-Noise Amplifier design, multi-channel correlated noise sources, and physical circuit modeling led by: David Bordenave, Rich Bradley.
- **Frontend Data Acquisition** – Configuration and integration of Software Defined Radios led by: David Bordenave, Krishna Makhija.
- **Monitoring and Control** – Embedded design and programming of monitoring and control systems: David Bordenave.
- **Digital Signal Processing and Software** – Development of a real-time spectrograph, data management and processing tools, and command-line and graphical user interfaces led by: David Bordenave
- **Integration, Testing, and Calibrations** – (David Bordenave)

Figure 4.2: Ground Commissioning of the GBT310 Receiver

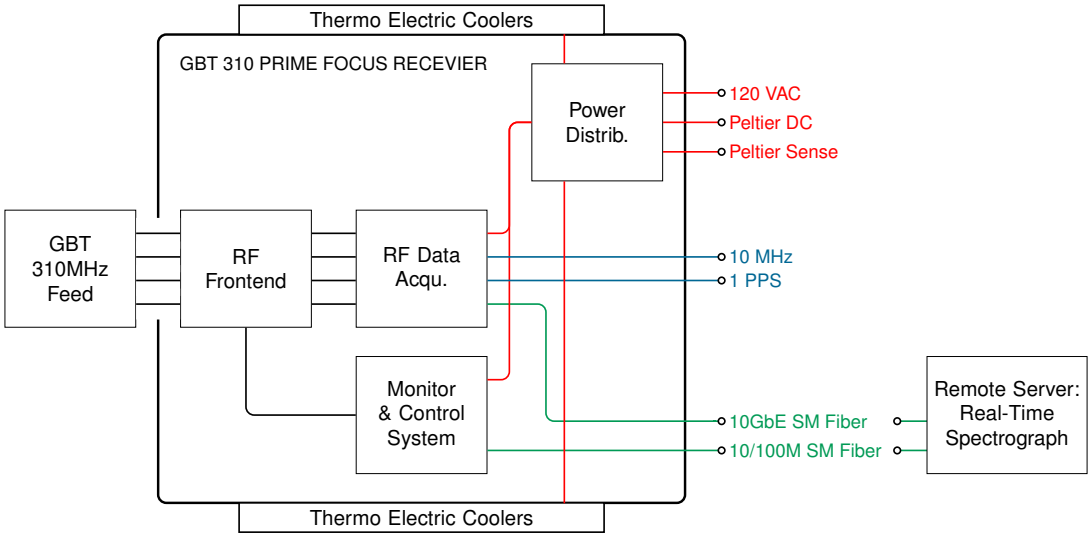

Figure 4.3: System Block Diagram of the GBT 310MHz Receiver

4.4 Feed

4.4.1 Electromagnetic Design

To achieve the desired $\sim$ 3 K uncertainty limit from antenna spillover, a custom high-edge taper and low sidelobe feed was designed to under-illuminate the GBT dish. This design was based on the *short backfire antenna* (SBA) design, which is an optimal choice for a compact antenna with high-gain ($\sim$ 15 dBi) for a narrow frequency band ($\sim$ 10%) (Ehrenspeck, 1965; Johnson & Jasik, 1993). The basic SBA features a dipole or cross-dipole feed between two circular planar reflectors spaced $\sim 0.5\lambda$ apart, with one larger ($\sim \varnothing 2\lambda$) than the other ($\sim \varnothing 0.4\lambda$), and which form a leaky resonant cavity structure with good sidelobe and backlobe suppression (by about $\sim$ 20dB and $\sim$ 30dB, respectively) (Ehrenspeck, 1965).

The GBT 310MHz feed design started as a scaled version of an 800-MHz SBA design provided by Sri Srikanth[1], which also draws lineage from the current PF1 feed (Srikanth & Behrens, 2007; Hwang et al., 2019; Lin et al., 2012). The reference design further improves on the work by Ohmori et al. (1983) and features enhanced bandwidth, edge-taper (the roll-off of the primary beam), and sidelobe/backlobe suppression beyond the standard SBA. The designed feed structure features a sleeved cross-dipole driven element and conical main and secondary reflectors with additional planar reflectors, and a corrugated rim (see Figure 4.4). Bang Nhan and Krishna Makhija, with assistance from Sri Srikanth, optimized the design and feedline transition for operation in the 300-320 MHz range using `CST` and `GRASP8` electromagnetic simulation programs.

Because the primary goal of the GBT310 feed was to reduce the uncertainty from spillover and ground pickup, the feed was optimized to limit the antenna gain falling beyond the telescope dish. For a prime-focus GBT receiver, the 100 $\times$ 110m off-axis parabolic dish subtends $\sim \pm 39^\circ$ (Srikanth & Behrens, 2007). Any feed gain beyond these bounds may intercept unwanted sources of noise, including $\sim$ 300K ground emission or RFI from the horizon, which are both pointing dependent. While spillover noise is generally unavoidable, the variation can be limited by controlling how fast the beam rolls off from boresight, to limit the average gain at the edge of the dish, as well as the sidelobe and backlobe levels. The GBT310 feed was specifically optimized for

[1]Senior Research Engineer at NRAO Central Development Lab

Figure 4.4: (Left) GBT310 Feed in the Field. (Top) Section View of GBT310 Feed

these requirements and resulted in a predicted gain at the edge of the GBT of -18.8 dB lower than the peak, with a minimum sidelobe suppression level of -30 dB for the target frequency range see Figure 4.5. The simulated beam patterns were verified with antenna range measurements conducted at the Green Bank Observatory outdoor antenna test range (see Figure 4.6). The range measurements (see Figure 4.7) showed good agreement with simulations except for the sidelobe level in the co-polarized H-plane beam cuts, which was roughly 5 dB higher than in the simulations. However, from the `GRAPS8` optical analysis using these corrections, the effective ground pickup with the GBT and mapping strategy (azimuth sweeps at constant elevation $\sim 38°$) is approximately 10 to 12 K. From these measurements and simulations, the expected spillover uncertainty is predicted to be $\sim 1 - 2$ K.

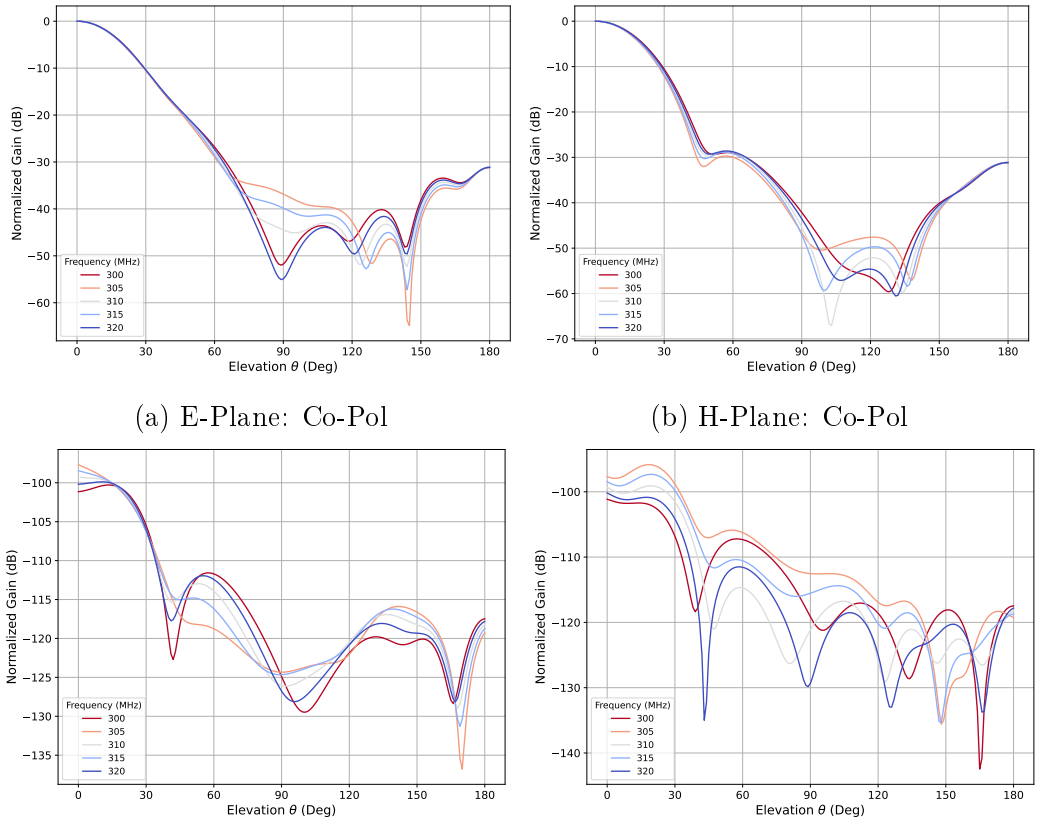

(a) E-Plane: Co-Pol

(b) H-Plane: Co-Pol

(c) E-Plane: Cross-Pol

(d) H-Plane: Cross-Pol

Figure 4.5: CST simulated beamcuts for the final GBT 310MHz feed design

Figure 4.6: GBT 310 MHz feed at the Green Bank Observatory outdoor antenna test range. (July 2021)

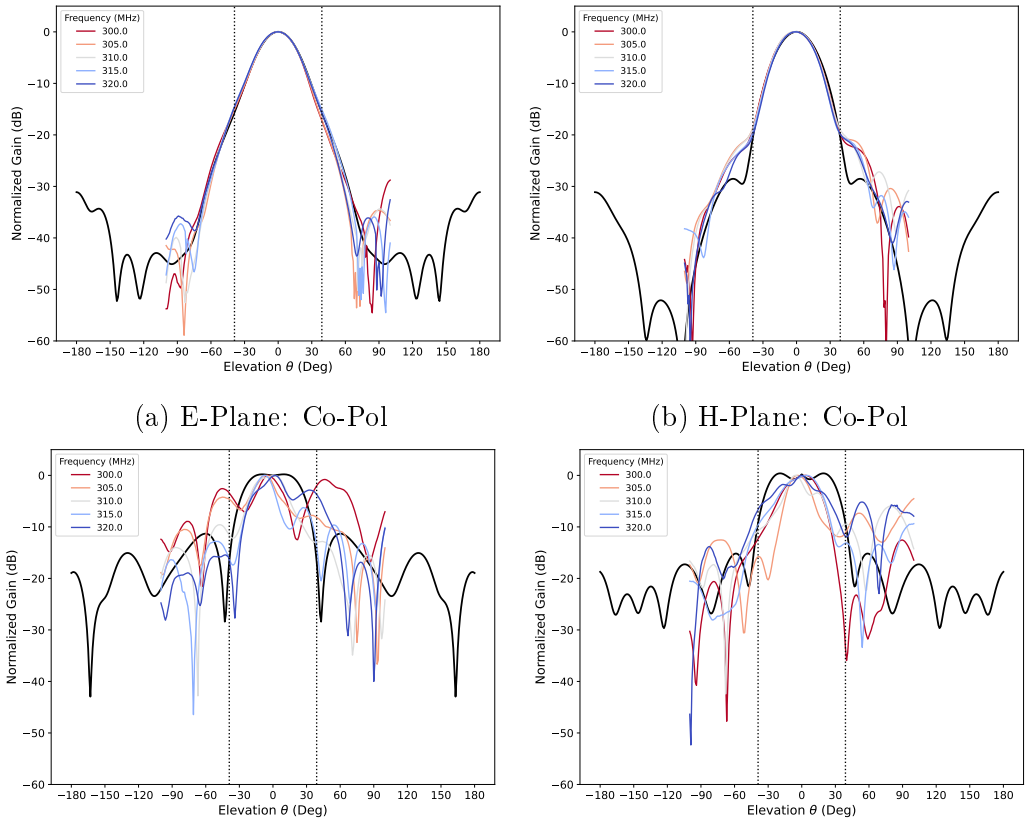

(a) E-Plane: Co-Pol

(b) H-Plane: Co-Pol

(c) E-Plane: Cross-Pol

(d) H-Plane: Cross-Pol

Figure 4.7: Measured beamcuts for the final GBT 310MHz feed design

Since the GBT 310 is a balanced correlation receiver, the feed did not use a traditional balun. Instead, each monopole was separately impedance-matched with 4 coaxial air-lines to provide the balanced 50Ω output for the directly-attached frontend receiver. This feedline assembly was integrated into the dipole stem assembly that supports the dipoles, sleeves, and sub-reflectors (see Figure 4.8). The simulated and measured S-parameters show good agreement, with reflection coefficients for each port (S11, ..., S44) better than 25 dB (see Figure 4.9). However, the feed appears to be slightly more inductive than predicted (see Smith Chart in Figure 4.10), likely due to manufacturing tolerances.

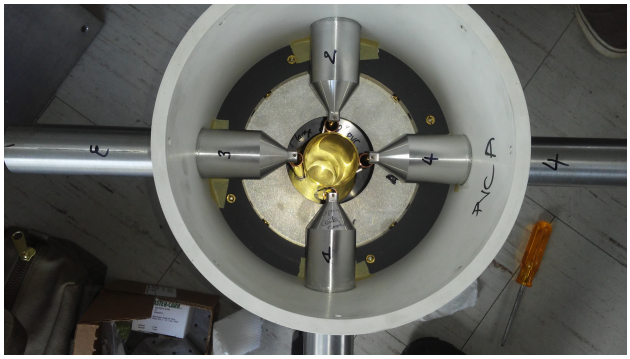

(a) Internal view of the GBT310 dipole assembly

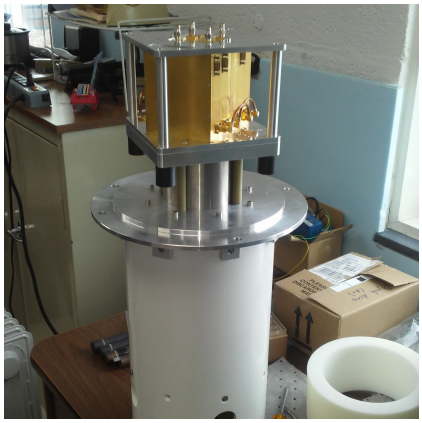

(b) Dipole assembly and receiver integration test fitting

Figure 4.8: Detailed views of the GBT310 dipole and feedline assembly and integration tests with the first iteration of the bulkhead and frontend receiver module.

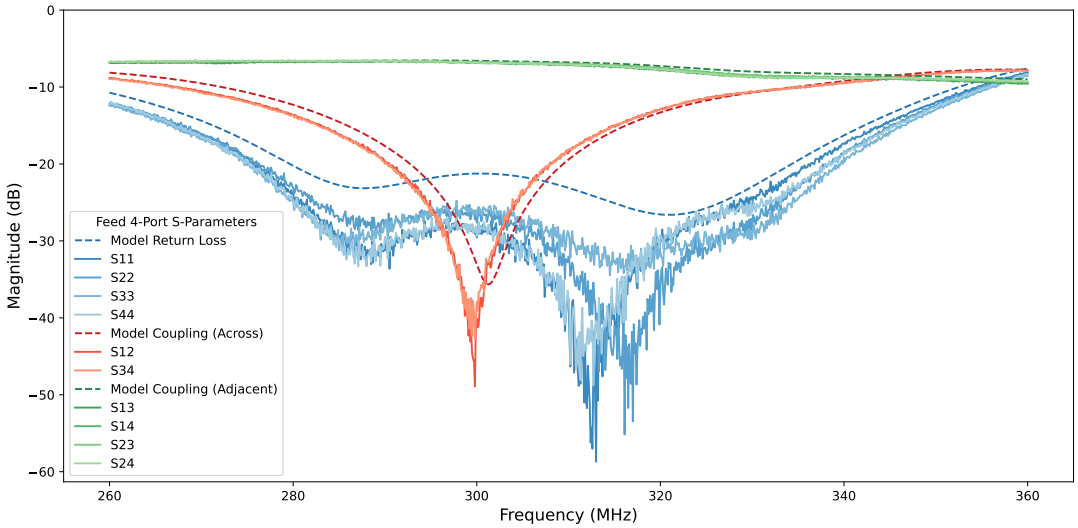

Figure 4.9: Summary of measured S-parameters for the GBT 310MHz feed: blue traces correspond to the return loss for each port, red traces to the coupling between opposing arms of the cross-dipole, and green traces to the coupling between adjacent arms of the cross-dipole. The dashed lines correspond to the simulated S-parameters from CST.

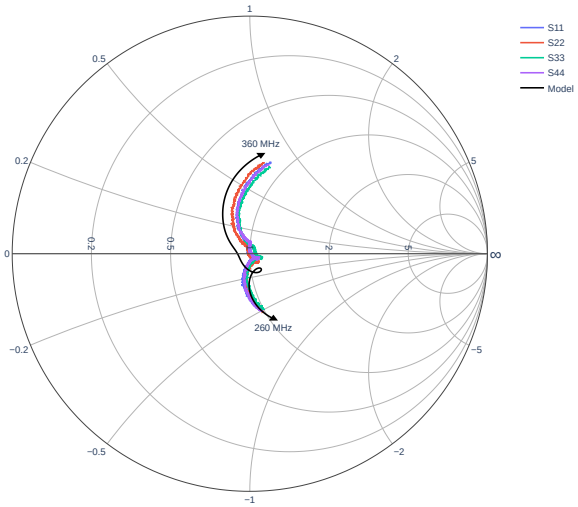

Figure 4.10: Smith chart of the measured and simulated return loss of the GBT 310MHz feed. The figure shows that the measured return loss of the feed is slightly more inductive than simulated, likely due to manufacturing and fabrication tolerances of the feedline assembly.

4.4.2 Mechanical Design

The electrical design of the 310 MHz feed posed a significant challenge for the mechanical design, construction, and eventual deployment of the antenna. The primary complication was that the overall size of the antenna, with exterior dimensions approximating a cylinder 31" tall with a diameter of 106," cannot fit, nor be assembled, within the typical prime-focus shelter on the Green Bank Telescope (see Figure 4.12). This presents a collision risk in the event of an 'auto-stow' of the prime-focus receiver (e.g., due to strong winds), with the feed striking the catwalks within the prime-focus shelter, or possibly the larger Gregorian-mounted feed horns (i.e., L-band and S-band). Furthermore, the large reflector cross-section will also be more susceptible to excessive windloading. Therefore, the feed was designed to be a modular structure for ease of handling and assembly. It balances the dimensional stability required to ensure consistent electrical performance, while also being strategically weakened, such that a potential collision or excessive windloading would not result in damage to the telescope structure.

Figure 4.11: A wooden mockup of the proposed GBT 310 MHz feed built in the Quonset hut by the NRAO CDL.

The mechanical design of the 310 MHz feed started in the summer of 2019 with an intial focus on testing the feasibility of mounting a large, seperable antenna reflector on the GBT prime focus boom. Using the preliminary dimensions from the EM simulations available at the time, a wooden scale model was constructed (see Figure 4.11). This matched the exterior dimensions of the proposed feed in order to test for clearances, and to evaluate the 6-fold segmented reflector design. While the feed mockup showed that the fully assembled feed does not fit within the catwalks as anticipated, it verified that the feed (with the 6-fold symmetry) can be partially assembled within the shelter, and the remaining segments mounted with the prime-

focus boom slightly retracted beyond the catwalks. It also demonstrated that the feed, when fully extended along the optical axis, clears all other obstructions except for the Gregorian mounted L-band and S-band receivers (see Figure 4.12). Fortunately, these receivers can be rotated such that they are out of the path that the feed will sweep through. Thus, the test showed that a large modular feed could be supported at the prime focus of the GBT.

(a) Prime Focus boom fully stowed (b) Prime Focus boom slightly retracted

Figure 4.12: Testing clearances and fit of the 310MHz feed mockup on the GBT Prime Focus Boom. Only two of the six segments were mounted to simplify testing. Note that the full feed would need to be assembled with the prime focus boom slightly retracted. Gregorian feed horns may continue to obstruct, such as the large L-band horn in view of panel (b).

Following the mockup feed test on the GBT, development continued for designing the final manufacturable version during Spring 2020. The feed was split into 8 primary sub-assemblies: a central hub, a dipole assembly, and 6 identical outer reflector segments. The central hub features a hexagonal, welded aluminum frame that forms the base of the reflector surface and includes the mounting flange for a standard GBT prime-focus receiver box, mount points on the perimeter and face for the six reflector segments on the perimeter, and a central bolt pattern to mount the dipole assembly.

The reflector segments form the complicated profile for the flare and corrugation of the feed, with an open frame covered with galvanized steel mesh forming the reflector surface. The final component is the dipole assembly, which was designed by Bang Nhan and Krishna Makhija, and incorporates the crossed-dipoles, feedlines, sleves, and sub-reflectors into a single, connectorized sub-assembly. The following section on the structural analysis will show the detailed design, which ensures the structural integrity of the feed for normal operating conditions and also in the case of excessive windloading or collisions.

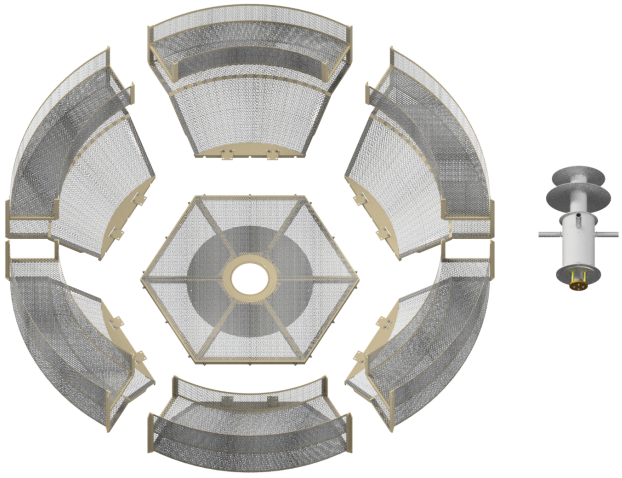

Figure 4.13: CAD render showing the exploded view of the GBT310 feed.

4.4.3 Structural Analysis

We start by addressing the most likely expected failure: a frontal collision of the feed into the catwalks within the GBT *Prime Focus Shelter* (PFS) during an auto-stow. This auto-stow would be triggered in the event of sustained wind speeds of 35 mph and gusts in excess of 40 mph (unless disabled), thus posing a persistent risk while the feed is deployed. While the best means of mitigating this risk is to plan observations only during fair weather, we must also ensure that the expected collision will not exceed the mechanical limits of the prime-focus sterling mount, as well as minimize damage to the GBT. For reference, the static force and moment limits of the GBT prime-focus sterling mount are 1,500 lbs, and 2,500 ft-lbs respectively.

The feed was intentionally weakened to force a predictable point of failure, thus

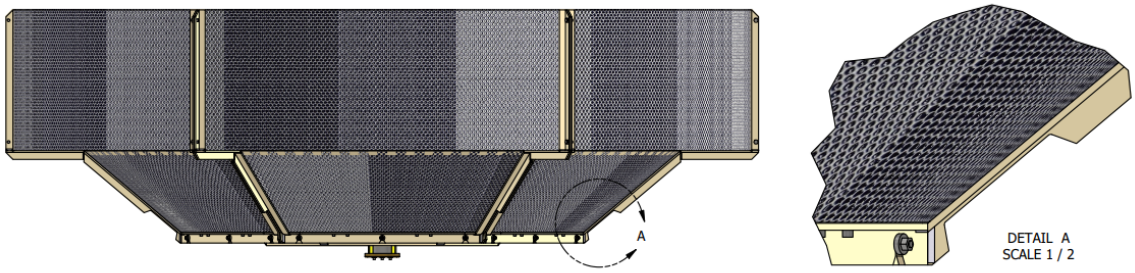

Figure 4.14: Detail View of GBT310 Feed Weakpoint

to minimizing the exerted force and moment on the prime-focus sterling mount (see Figure 4.14). For a frontal collision, the outer edge of the reflector will collide first and will generate a bending moment within the support structure due to the external force. Because the central hub is more rigid than the outer reflector segments by design, the stress due to the bending moment will naturally concentrate at the base of the reflector support arm that is experiencing a collision. Thus, by adding relief cuts at the base of each reflector segment support arm, the structure can be weakened in the radial direction to match the expected collision geometry, and to break at a specified bending moment.

We can design the reflector support arms to yield or break at a target failure load using a simple analytical model of the bending stress within a cantilever T-Beam (Appendix A.1) and the strength of the material. We define the safety factor following Timoshenko (1983) as

$$N = \frac{\sigma_U}{\sigma_B} \tag{4.2}$$

where N is the safety factor, σ_U the ultimate yield strength of the material, and σ_B the bending stress that develops for the desired breaking load applied to the feed support arm A.1. Since we want the structure to fail, we require $N \leq 1$ when the failure load condition is applied. We can use this relation with the cantilever T-beam bending stress model to estimate the breaking load for a given depth of cut in the web of the T-beam (the vertical section).

The results of this model are shown in Figure 4.15, using the ultimate strength of $\sigma_U \approx 42,000$ psi (Al 6061-T6). We see that the T-beam is weakest in compression for this collision arangement, thus the arms are expected to fail by buckling first. For a desired breaking load of $\sim$ 100 lbf applied to the outer edges of the feed (at the

corrugated rim), a 0.875 inch depth of cut is sufficient.

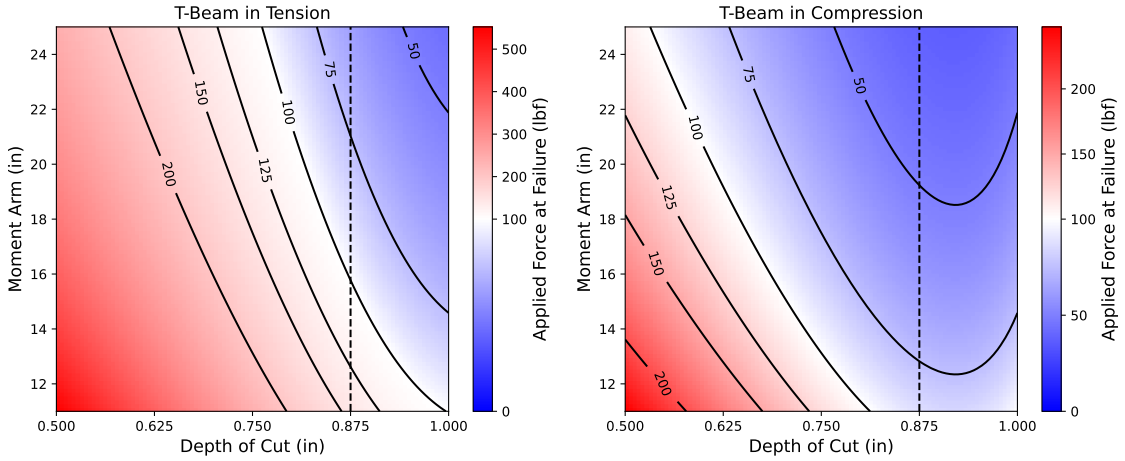

Figure 4.15: The force required to exceed the ultimate yield stress of the T-beam at the extreme fibers for a range of expected moment arm lengths. The dashed line shows the final selected depth of cut for the T-beam web, such that the failure load is approximately 100 lbs for a moment arm range between 12-24 in. In this scenario, the T-Beam will be weakest in compression, thus the failure is expected to occur first at the outer-most part of the web.

Structural Analysis — Static

The analytical bending-stress failure model was verified with numerical Finite Element Analysis (FEA) trials using Autodesk Iventors integrated tools. A collision can be simulated by applying force vectors on the 3D model at likely interaction points. The most likely collision to expect will apply an angled force on the outer or inner edge of the feed support arms that are 180° or 120° separated (see Figure 4.12). We can then find the safety factor in tensions and compression by appling a 100 lbs force vector at 45° on these support arms (see Figure 4.16). The results of these FEA trials are in agreement with the analytical model and show an estimated load at failure of 100 lbs or less. Table 4.1 compiles the results for axial and lateral loading conditions (simulations shown in Appendix A.2).

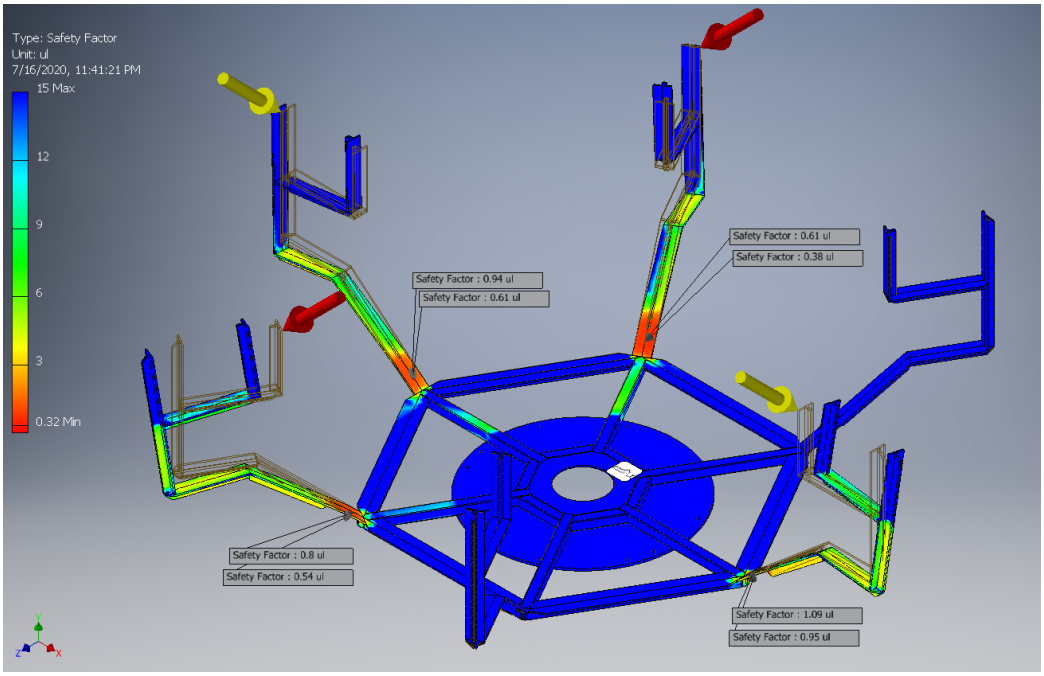

Figure 4.16: GBT310 FEA static analysis for 45° angled collision with 100 lbf point loads

Arm	Failure Load (lbf)		
Separation	Axial	45°	Lateral
180°	100	100	150
120°	100	75	75

Table 4.1: Breaking force

Structural Analysis — Modal

By intentionally weakening the feed structure in the radial and axial direction, as to not overstress the prime-focus sterling mount in case of a collision, we may also be lowering the characteristic resonant frequencies of the structure. These frequencies are tied to specific vibrational modes (essentially the eigenstates of the structure) of the structure (see Figure 4.17 and Appendix A.3). Therefore, if an external driving force has a similar frequency as one of the harmonic frequencies of the structure, large oscillations can be excited and potentially lead to the failure of the structure.

Modal analysis of the GBT310 feed was performed with Autodesk Inventors FEA modal analysis tools to determine the charactistic vibrational modes and frequencies of the feed structure. This was performed for the frame only, and with thin support bands that provide shape to the mesh that lines the feed. Results of these results are shown in Table 4.2, which are roughly an order of magnitude greater than known expected oscillations (e.g., ~ 0.5 Hz at the prime focus boom).

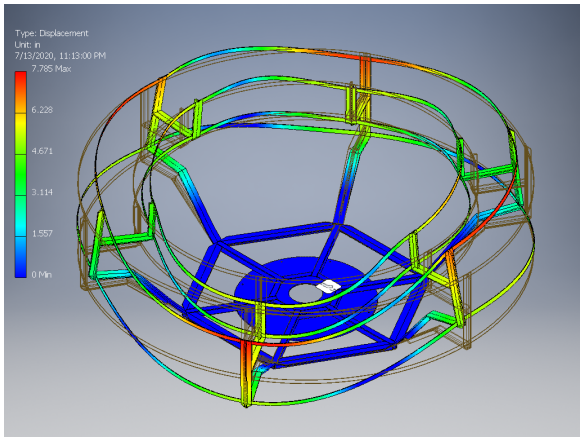

Figure 4.17: GBT310 FEA trial for 45° angled collision with 100 lbf point loads

Mode	Frequency (Hz)	
[n]	Frame	Frame+Banding
1	4.64	10.19
2	4.65	10.19
3	4.67	11.32
4	4.68	12.47
5	4.71	15.15
6	4.72	15.26
7	10.31	15.57
8	10.35	21.06
9	10.37	21.59

Table 4.2: Summary of the first 9 vibrational modes.

Structural Analysis — Wind Loading

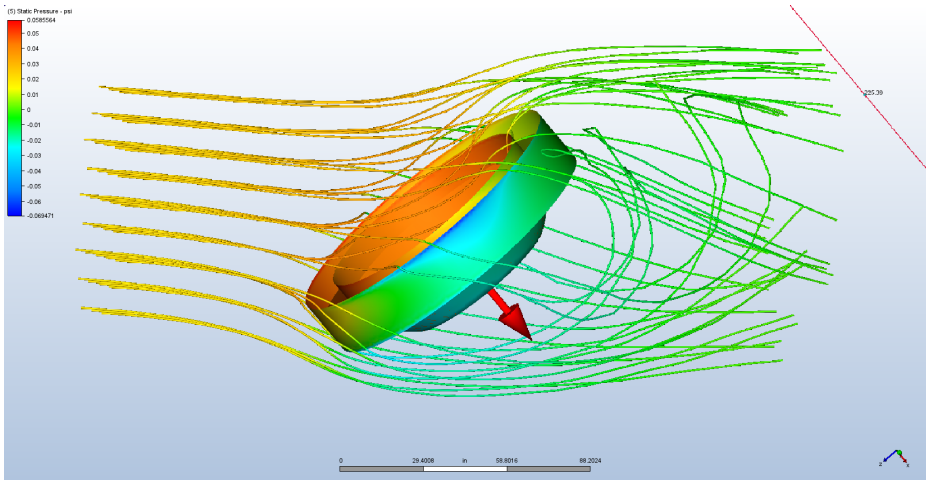

Figure 4.18: CFD Simulation Screenshot

Wind-loading was another concern due to the large size of the GBT310 feed (∼ ⌀106"). The potential applied force due to wind loading was first estimated by using the drag equation due to a steady state fluid flow:

$$F_w = \frac{1}{2}\rho A C_d v^2 \tag{4.3}$$

where ρ is the fluid density, A is the cross-sectional area, C_d is the drag coefficient, and v is the fluid velocity. The drag coefficient is typically an experimentally-determined, dimensionless value that encompasses the complex dependence of object shape, inclination, flow conditions, and more. Johnson & Jasik (1993) tabulates typical values for a convex shaped antenna that is solid or mesh (with 1/2" openings) with drag coefficients $C_{d,solid} = 1.8$ and $C_{d,mesh} = 0.8$, respectively. The estimated axial force due to windloading, for standard atmospheric conditions, is provided in Figure 4.19.

These estimates of the worst-case wind loading condition (face-on) can subject the feed to 250-600 lbf at 50 mph. Because these values are close to half of the static force limit of the prime-focus mount, more careful analysis needed to be performed to correctly include the complex shape of the GBT310 feed. The wind loading was analyzed Computational Fluid Dynamics (CFD) simulations performed with Autodesk CFD (see Figure 4.18). The feed (in various states of assembly) was subjected to face-on (axial), angled, and lateral winds ranging between 5-50 mph, with the results

tabulated in Table 4.3 and shown in Figure 4.19. Simulations were limited to solid surfaces rather than mesh, thus we used the ratio of a convex mesh versus convex solid drag coefficients to scale the CFD simulations of the solid reflector axial case into an approximate mesh equivalent.

The simulated worst-case wind loading forces for the mesh version of the GBT 310 feed are substantial ($\sim$ 900 lbs at 50 mph) but unlikely to occur, since the feed would be angled with respect to the horizon for typical operating conditions. Also, when observing with this receiver, telescope operators may be required to pre-emptively stow the feed at lower than typical wind-speeds ($v < 35$ mph).

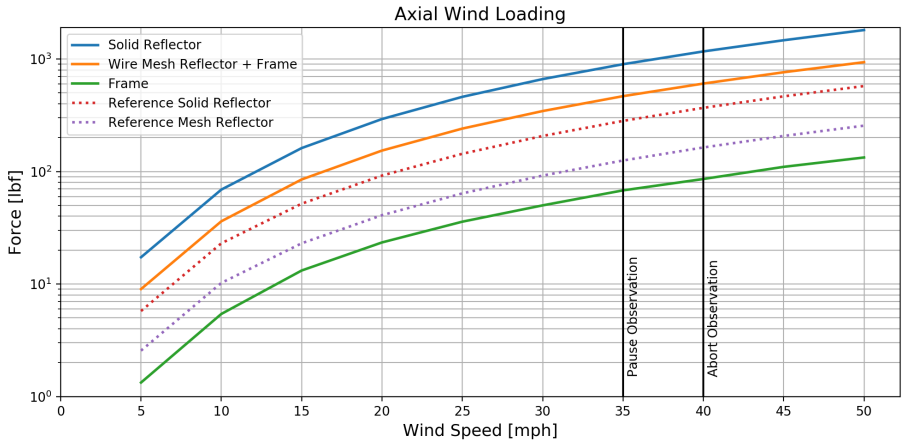

Figure 4.19: CFD wind loading simulations for the GBT 310 Feed.

Wind Speed	Axial Wind Load (lbf)			45° Wind Load (lbf)		Lateral Wind Load (lbf)	
(mph)	Frame	Frame+Mesh	Solid	Frame	Solid	Frame	Solid
5	1	9	17	–	9	0	2
10	5	36	69	–	37	1	6
15	13	85	162	–	88	3	15
20	23	154	293	–	155	4	25
25	36	241	461	–	251	7	37
30	50	345	664	–	370	10	53
35	68	468	900	–	505	14	72
40	86	605	1169	–	643	18	94
45	110	763	1470	–	821	22	120
50	133	938	1810	–	983	27	148

Table 4.3: Summary of wind loading for different configurations of the feed.

4.5 Frontend Receiver System

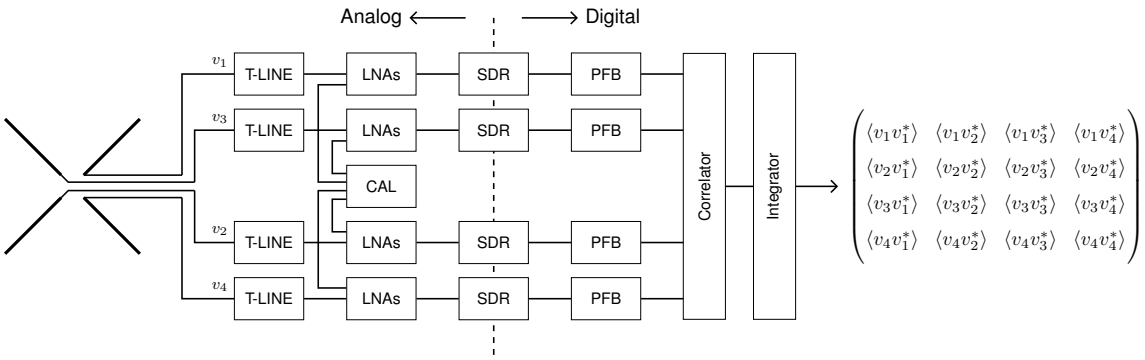

Figure 4.20: The GBT 310MHz Balanced Correlation Receiver Architecture

4.5.1 Receiver Architecture

To meet the observational uncertainty requirements of $\sigma_{RX} \lesssim 4$ K, the GBT310 receiver needs to be gain and noise temperature stable on timescales of at least ten minutes (the approximate length of one azimuth sweep). However, because the planned observations are confusion-limited at the achievable angular resolution $\theta \lesssim 1^\circ$ and slew rates of 30° min^{-1}, the sensitivity of the receiver will largely not be a driving factor (Condon et al., 2012). While these conditions make non-cryogenic receivers a viable option, the long-term stability requirements motivated the development of a novel correlation receiver design: the balanced correlation receiver (BCR; see Section 3).

A balanced correlation receiver can, in theory, achieve both superior gain stability and zero-offsets, because it removes all shared signal paths (e.g., transmission lines, baluns, power splitters, etc.) by forming the antenna through a unique digital synthesis process that uses only cross-correlations of redundant-in-polarization sensing elements. Because the receiver noise values for each branch are statistically independent and uncorrelated (except for global effects such as large temperature swings), averaging the product/cross-correlations between amplifier chains will only retain correlated components (e.g., the input signal). This process significantly reduces possible gain fluctuations because the self-generated $1/f$ flicker noise with potential knee frequencies (with knee frequencies on the order of 1 Hz $< f_k <$ 1 kHz; Condon &

Ransom (2016)) will also decorrelate.

Because the GBT 310MHz receiver was the first prototype of the BCR concept, it posed a significant developmental effort to determine relevant system specifications and implementations for it to work. As part of this effort was the design, implementation, and testing of a custom, highly-integrated Frontend Receiver Module. This sub-system implements the core analog functionality required for a full-Stokes balanced-correlation receiver: 4 low-noise amplifier branches, along with a configurable 4-channel coherent noise source (see Figure 4.20). The amplifier branches establish the complex gain and receiver noise temperature of the system, and include an input switch for calibration. The 4-channel coherent noise-source provides both correlated and uncorrelated reference signals for the receiver that can be used for a Y-factor calibration measurement and receiver phase alignment.

These sub-circuits were housed within a stack of individually compartmentalized brass modules mounted in a modular sub-assembly that provides maximum electrical isolation along with phase and thermal stability (see Figure 4.21). To further minimize transmission line losses, the whole receiver sub-assembly was directly attached to the output of the antenna feedlines by a spring-loaded bulkhead assembly and press-fit BMA connectors. The Frontend Receiver sub-assembly is interfaced to the rest of the system with four independent SMA ports, and a consolidated 78-pin d-sub connectorized wiring harness that carries power, parallel control signals, and sensor lines to each sub-module via six 15-pin micro d-sub connectors. The four outputs from the central calibration module are connected to the calibration input of each amplifier via short, length-matched RG-402 semi-rigid coax jumpers to minimize phase variations.

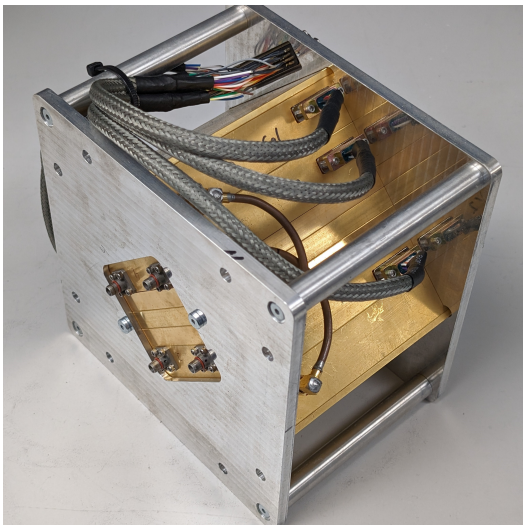

(a) GBT310 Receiver Module v1

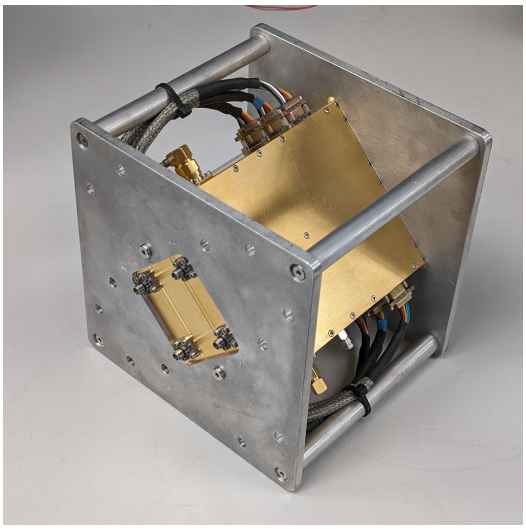

(b) GBT310 Receiver Module v2

Figure 4.21: System block diagram and finished assembly of the GBT 310MHz amplifier module. Each amplifier module contains a pair of identical amplifier boards within separate compartments to ensure high isolation between receiver channels.

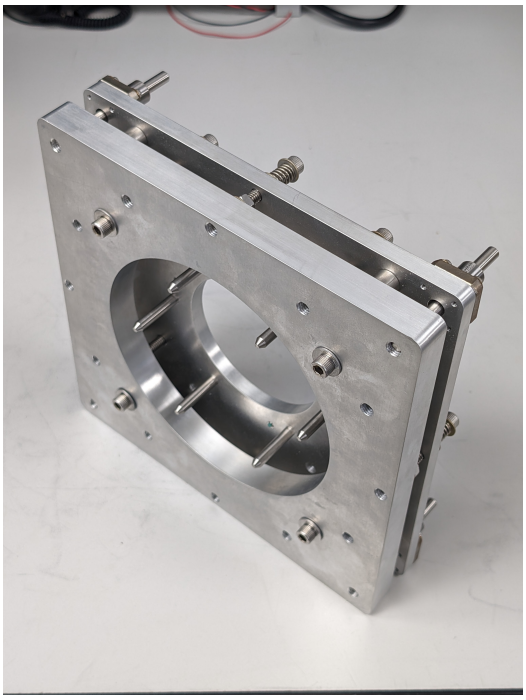

Figure 4.22: GBT310 Receiver Bulkhead Assembly. The long pins are keyed such that they align the output ports of the dipole assembly with the inputs to the receiver module. The thinner plate is spring-loaded to provide a consistent connector mating force.

4.5.2 Amplifier Module

The four identical low-noise amplifier (LNA) branches of the GBT310 Frontend Receiver ultimately establish the noise performance and sensitivity of the GBT310 receiver. However, since it is part of a larger system, the Frontend Receiver will also interact with any other RF device that interfaces with it. Therefore, careful modeling and characterization of the device are essential, which is especially important for calibration purposes, as the port impedance of the feed and the noise source will generally be different. This difference in source impedance will also, in practice, change the behavior of the system. This would include the effective transducer gain (Pozar, 2012) and with it, any derived calibration solutions. For this reason, both physical circuit modeling and extensive lab measurements were used in the design and characteriation of the frontend amplifier circuitry.

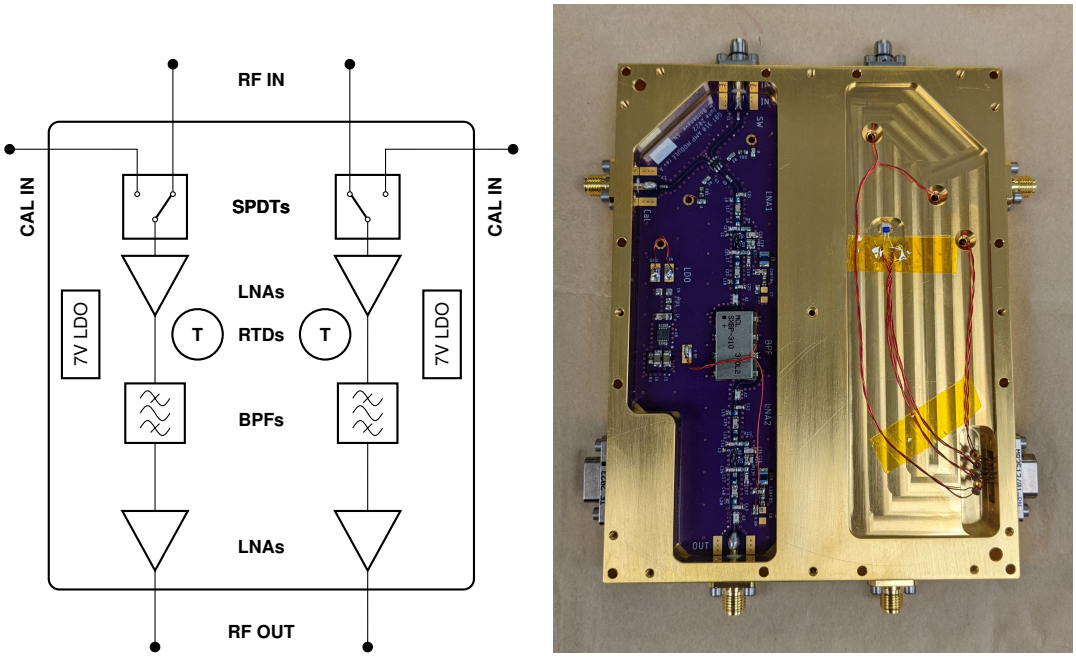

(a) Amplifier Module v2 Block Diagram (b) Amplifier Module v2 Assembly

Figure 4.23: System block diagram and finished assembly of the second iteration GBT 310MHz amplifier module. Each amplifier module contains a pair of identical amplifier boards within separate compartments to ensure high isolation between receiver channels.

The frontend receiver sub-assembly contained two identical dual-channel amplifer modules. The housings were designed to be rotationally symmetrical, such that the

same amplifier circuit boards and layout could be used for both the left and right side channels. Each amplifier board consisted of an input select RF switch, a first stage LNA, bandpass filtering, and a post-filtering gain stage, along with a local linear voltage regulator. Despite being lossy (~ 0.3 dB for the Analog Devices HMC595A), having the RF switch as the first element is essential for the absolute calibration of the downstream system, as the y-factor method used requires known reference inputs (Pozar, 2012). This allows the receiver to be in well-known and discrete states, which is not possible with a directional coupler that would merely add the calibration signal onto the background sky signal. Although the switch is an integrated circuit, without details on the internal implementation, it is a relatively simple circuit for which Rich Bradley was able to determine a good physical circuit approximation verified with lab measurements.

The design and testing of an optimized discrete component Low-Noise Amplifier (LNA) was another major development effort that underwent a series of design iterations. Using Keysight Advanced Design System (ADS), Rich Bradley designed the first iteration of the GBT310 LNA based on the standard common-emitter configuration. Although the LNA design had a good gain (~ 25 dB) and noise figure (NF ~ 1 dB or $T_e \approx 75$ K), it became apparent during lab integration tests that the input and output reflection coefficients (S11 ≈ -6 dB and S22 ≈ -9 dB) would be potential limiting factors that could be causing spurrious coherent signals due to reflections which could couple into other channels and remain correlated. This motivated a redesign of the LNA circuit (along with the calibration module), which tried to improve the input and output match, and reverse isolation of the circuit. A cascode configuration (a multi-stage common-emitter and common-base transistor pair) was chosen due to its high inherent reverse isolation. This allowed for easier impedance matching on each port, as they would only minimially interact (see Appendix A.5 for further details). This design resulted in a comparable system gain ($S21 \approx 23.5$) dB and noise figure (NF ≈ 1.1 dB or $T_e \approx 85$ K) to the first LNA design, but with enhanced reverse isolation ($S12 < -60$ dB limited by VNA noise floor; see Appendix A.5). When integrated into the receiver chain, it yielded an effective input and output impedance of S11 $\approx$ S22 ≈ -20 dB (see Figure 4.24 and Table 4.4).

Following the first stage amplifier is a lumped element 300-320 MHz bandpass filter (Minicircuits SXBP-310+) that is used to bandlimit the received signal and reduce unwanted noise power. Because the device was composed from discrete com-

ponents, Rich Bradley was able to disect and characterize each sub-component using an impedance analyzer in order to construct a physical circuit model. The filter is then followed by another LNA to boost the signal for further downstream devices.

Finally, each amplifier chain is powered by a low-noise linear regulator (Analog Devices LT3042 RF LDO) to improve both the power supply stability (minimizing gain fluctuations), and the power supply rejection ratio (PSRR) that increases the isolation between amplifier chains through the main power supply. Additionally, each amplifier circuit has co-located RTD sensors in a 4-wire sensing configuration mounted by the first amplifier stage (see Figure 4.23).

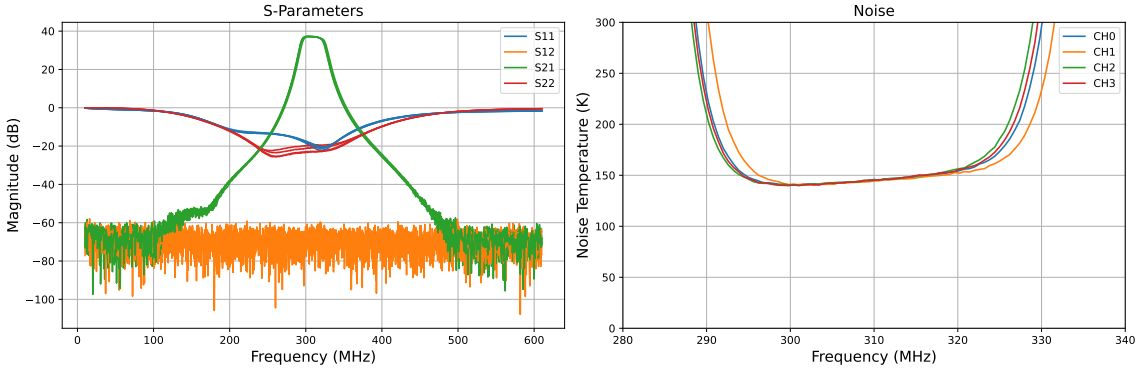

Figure 4.24: S-parameter and Noise Temperature Performance of the GBT 310 MHz Amplifier Channels.

Parameter	Condition (MHz)	Min.	Typ.	Max.	Units
Frequency Range		300		320	MHz
DC Voltage			7		V
Current			16		mA
Gain		35.96	36.15	37.35	dB
Input Return Loss		-22.20	-20.99	-17.51	dB
Output Return Loss		-23.32	-21.92	-19.37	dB
Reverse Isolation		-85.11	-79.94	-59.60	dB
Noise Figure		1.71	1.75	1.86	dB

Table 4.4: GBT310 Amplifier Module Typical Channel Performance Characteristics.

4.5.3 Coherent Calibration Module

The Coherent Calibration Module (CCM) is a multi-function noise calibrator essential for the absolute amplitude and phase calibration of the GBT310 system. The CCM allows for in-situ self-calibration of the receiver through the standard Y-factor method, which uses two matched loads at significantly different temperatures to estimate the gain and equivalent noise temperature of the system (see Appendix A.4.1). These different noise sources are realized by a central noise diode (a device that produces a controlled amount of electical noise) or by ambient-temperature 50 ohm resistors that are routed through a RF power-splitter/switch/attenuator network to produce coherent or incoherent/uncorrelated noise at the outputs of the CCM.

However, the CCM itself needs to be calibrated by the internal hot/cold sources using another external standard reference calibrator (e.g., NIST[2] traceable noise sources or physical temperature loads). A physical temperature load was used because they can generate pure white Gaussian noise by virtue of the intrinsic thermal noise of resistors (Johnson-Nyquist Noise; Johnson (1928); Nyquist (1928)). This was chosen instead of noise diodes that require an electrical current (e.g., Shot Noise; Schottky (1918)), and thus would offer the least uncertainty in the calibration solution. The full system calibration for each receiver channel can be performed by a reference Y-factor measurement using a liquid nitrogen noise standard as the cold reference ($T_{cold} \approx 77.5$K; see Figure 4.25) and an ambient-temperature 50Ω termination as the hot reference ($T_{hot} \approx 290$K) that are applied to the antenna input ports. Using these calibration solutions, the equivalent input noise temperature for the internal noise sources can be determined and later used for the in-situ Y-factor calibrations. Unfortunately, this process identified a significant problem within the first iteration of the CCM and GBT Frontend: the internal cold source was contaminated by other coherent noise contributions from the signal path. This ultimately motivated a redesign of the complete Frontend Module.

[2]National Institute of Standards and Technology

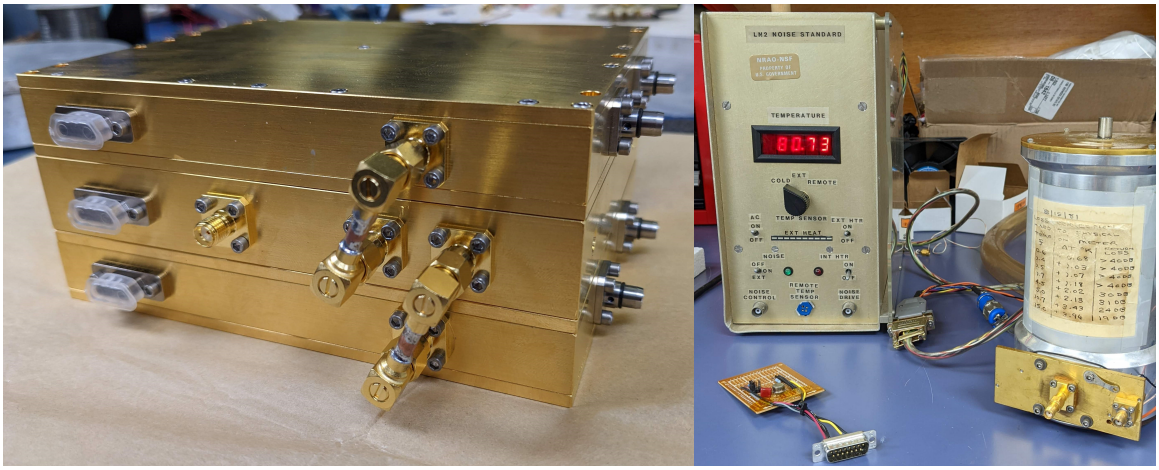

(a) Cal Module v2 (middle) with Interconnects (b) A Vintage LN Noise Source

Figure 4.25: (Left) Closeup view of the GBT310 Frontend Receiver Module v2 showing the calibration module sandwiched by two amplifier modules with coax interconnects for noise injection. (Right) Cryogenic Liguid Nitrogen noise source from the early 1980s used as the reference calibrator for the system.

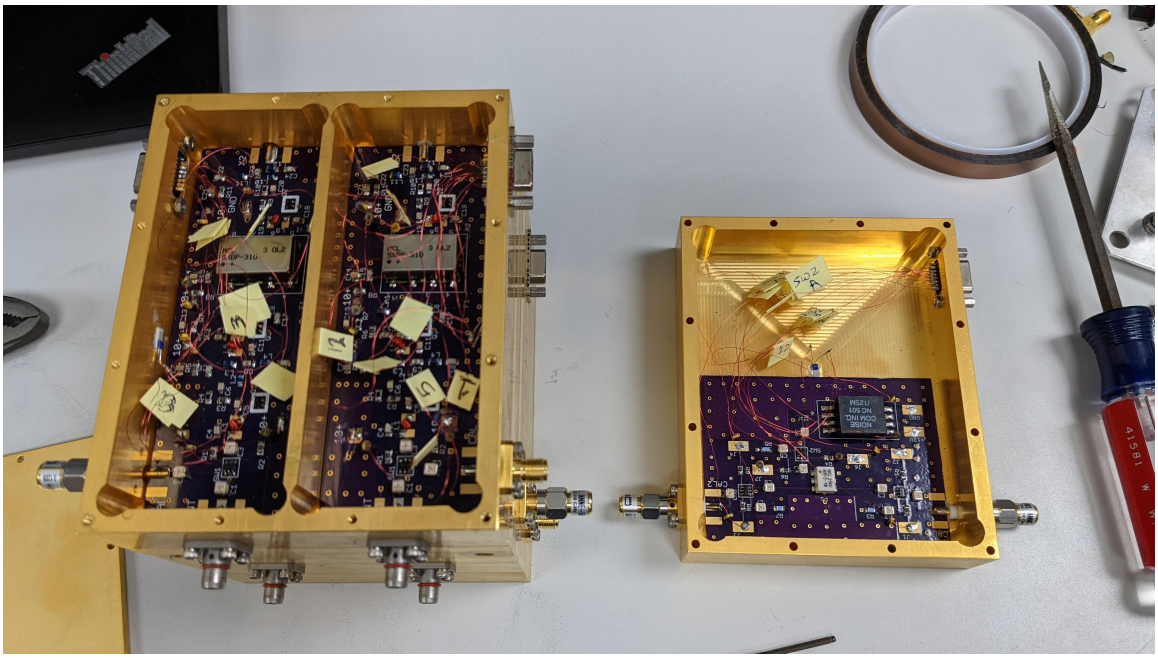

Figure 4.26: Internal look of the first iteration GBT310 frontend receiver modules. Left is a look at one of two v1 amplifier modules, and to the right one of two v1 dual-channel calibration modules.

CCM v1

The first iteration of the CCM consisted of two dual channel modules, one per polarization. This was because initially, only a total power measurement was considered (the sum of power from both x and y polarizations), and was conceptually simpler to implement. Each of these modules uses a Noisecom NC501/12SM 31 ± 2 dB ENR 200kHz-500 MHz for the hot source and a precision 50Ω resistor at ambient temperature for the cold source. This source was selected using an Analog Devices HMC595A SPDT (Single-Pole Double-Throw) RF switch, and split into two channels via a Mini-circuits ADP-2-1W 0° RF power splitter, followed by another set of RF SPDT switches that select either the common noise source or an independent 50Ω load to pass through to the outputs of the module. The power, switch control, and RTD temperature sensor signals are provided by a 15-pin micro d-sub connector.

When conducting an external cryogenic Y-factor calibration measurement for both single channel and 4-way power splitter use, it was observed that the system noise power was greater for the cryogenic source than either the external or internal ambient-temperature noise sources (see Figure 4.27). After a long series of troublshooting tests and mockups, this issue was later isolated to the power splitter. The power splitter, due to the 100Ω resistor that bridges the two outputs, generated its own coherent noise that was out-of-phase with the applied noise signal from the common port. Because the system measures the superposition of any coherent signal present, the room-temperature common noise would cancel out due to similar noise temperature from the splitter that is $\sim 180^\circ$ out-of-phase, while for the cryogenic noise source, the intrinsic splitter noise would dominate and only partially cancel out. If not addressed, this would increase uncertainties in the calibration, as the internal cold-source would be strongly affected by the distribution circuit, as well as with phase uncertainties when determining the complex gain.

CCM v2

An improved version of the calibration module was designed to address the issues discovered in the first iteration, and to support Full-Stokes measurements. The CCM v2 used a direct 4-way Wye resistive power splitter, instead of the lumped-element Wilkinson power splitter used in the prior version (Pozar, 2012). Although a resistive power splitter has more insertion loss, it offers better broadband behavior and does

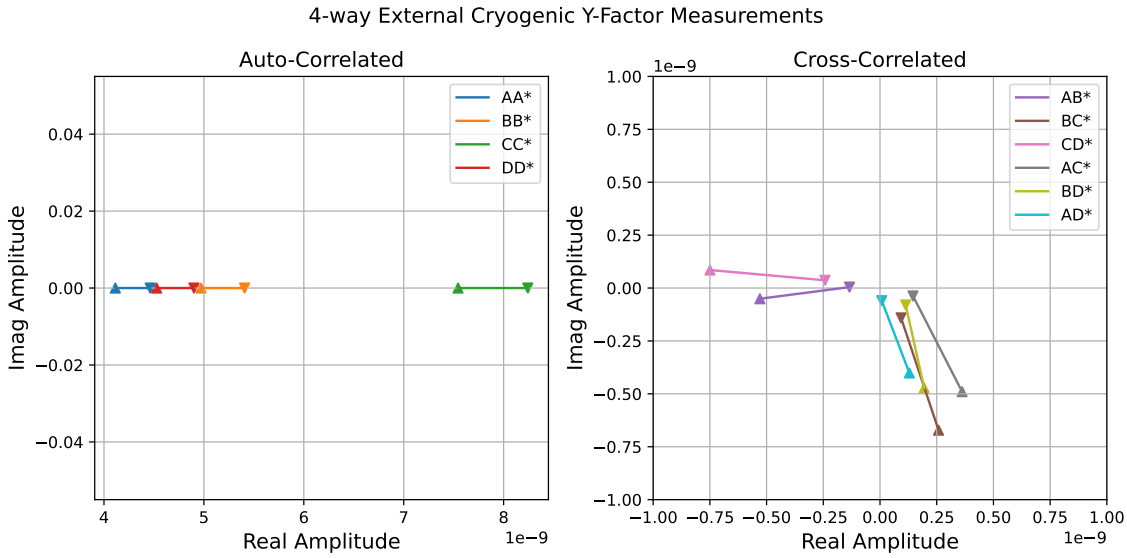

Figure 4.27: External 4-way split cryogenic Y-factor measurements of initial GBT310 Frontend Receiver Module showing excess low temperature noise (upward triangles) compared to the room-temperature noise source (downward triangles) for cross-correlations. The phase was not corrected for the four correlation pairs between different radios.

not produce significant out-of-phase noise components. However, this higher insertion loss ($L_{res} \approx 12$db) required a higher-power Noisecom NC511/12SM 51 ± 2.0 dB ENR noise source. A further addition was the use of a 20 dB digital step-attenuator for generating the hot and cold sources from the noise diode, along with an auxillary through port that allows for full through-measurement of the system using a VNA, in order to find the phase variation between output ports, and for calibrating the physical circuit models using Keysight ADS (for temperature dependent models).

This new calibration module allowed for all amplifiers to see the same calibration signal. This simplified the system calibration to understand one calibrator rather than two, and also allowed for better phase-alignment of the software defined radios used in the acquisition system. Furthermore, it allowed for calibrating the internal phase imbalance between channels and full-system verification self-tests.

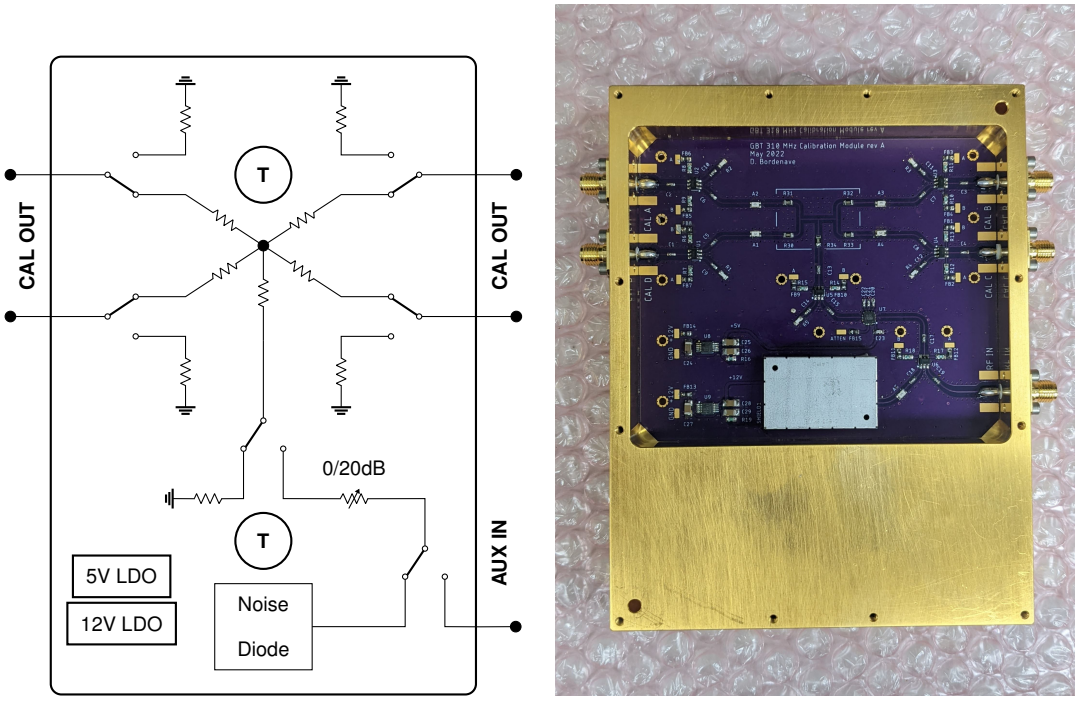

(a) CCM v2 Block Diagram (b) CCM v2 Assembly

Figure 4.28: System block diagram and finished assembly of the second iteration of the GBT 310MHz coherent Calibration Module.

4.6 Monitoring and Control System

The Monitoring and Control System (MCS) provides the computer interface to monitor and control the operational state of the GBT310 Receiver. The primary functionality of the MCS includes: (1) controlling the active signal path via RF switches within the frontend modules, and (2) monitoring remote temperature sensors placed near critical RF circuitry, ambient environmental sensors (temp, pressure, relative humidity), and the voltage and current of the system power supply rails 4.29. These functions were implemented with a set of custom circuit boards and an STMicroelectronics STM32F767ZI ARM Cortex-M7 microcontroller (MCU) development board. The MCS embedded circuitry was self-contained in a heavily modified 2U rackmount enclosure alongside AC to DC linear power supplies and the fiber media converter for the computer link (see Figure 4.30). Additionally, since this system is located within the receiver box, great emphasis was placed on RFI/EMI suppression using conductive gaskets, RF absorbing foam, filtered interfaces for power and signals lines,

and a cut-off waveguide for the fiber ethernet link.

The embedded microcontroller runs custom firmware using FreeRTOS to implement the system Finite State Machine (FSM), configure and operate all peripheral devices, and run a TCP server for remote control. A client program can connect to the MCS via the fiber ethernet interface and communicate using string formatted messages (with a SCPI like syntax). These messages are parsed and passed on to the FSM to change the state of the frontend receiver, while the data link also provides a streaming source for metadata back to the client.

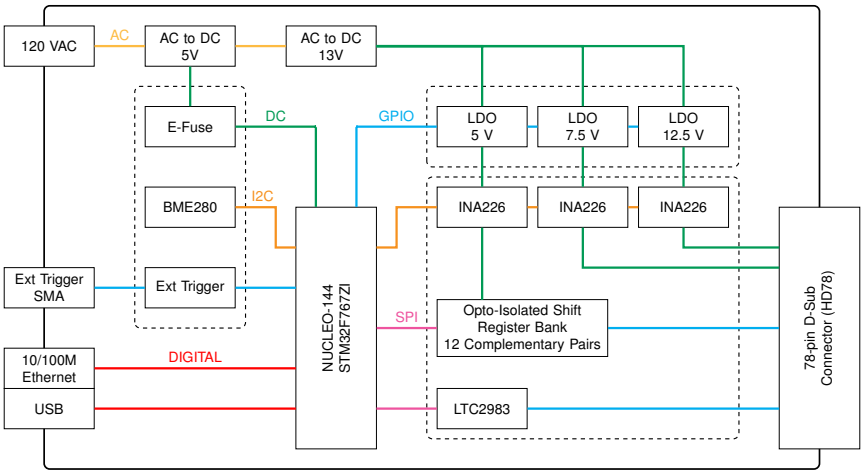

Figure 4.29: GBT310 Monitoring and Control System block diagram

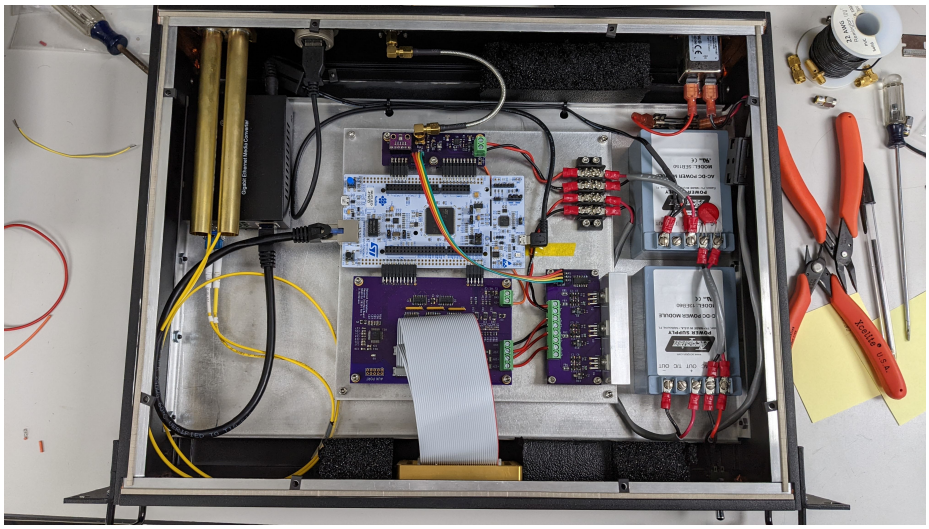

Figure 4.30: GBT310 Monitoring and Control System

4.7 Thermal Control Systems

The GBT310 uses thermoelectric coolers (or Peltier modules) for thermal control of the receiver box. This is the the standard method used by GBT prime-focus receivers, however for those systems, it is used to maintain a stable ambient enviroment for the exterior of the cryostats and IF circuitry. For our purposes, since the GBT310 is a room-temperature receiver, it will be the primary form of thermal stabilization. Fortunately, the lower power draw of the electronics create minimum additional heat that needs to be stablized.

The GBT receiver box used for the instrument features two rows of Peltier cooler assemblies on either side of the receiver box with external and internal heatsinks. The internal heatsinks are exposed within a plenum and form a forced air heat exchanger that circulates through the box. This airflow is monitored by a thermocouple, which is used to servo the Peltier modules to cool or heat the interior to within $< \pm 1^\circ$ C.

Figure 4.31: GBT310 Receiver Box Prepared for Transport

(a) One of 4 Peltier Sub-Assemblies

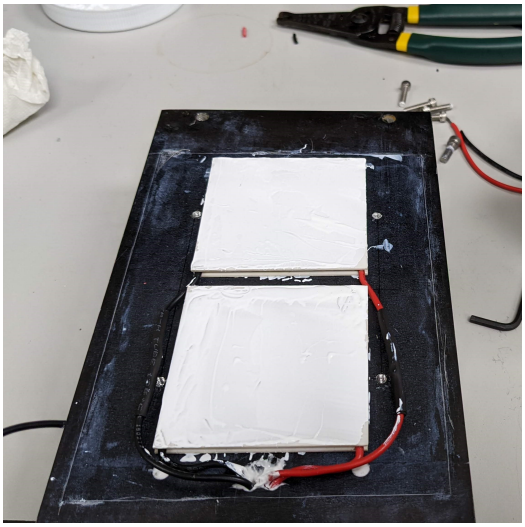

(b) Peltier Modules During Assembly

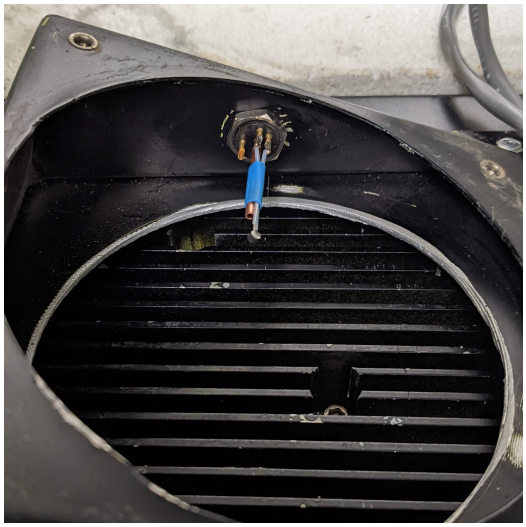

(c) Temperature Sensor

Figure 4.32: Pictures of the GBT310 Thermal Control System in various states of assembly.

4.8 Data Acquisition System

The Data Acquisition System (DAQ) of the GBT310 uses primarily commercial off-the-shelf hardware in the form of a small form-factor computer and two Ettus Research B210 software defined radios. These devices were mounted within a heavily modified 3U rackmount enclosure, and located within the instrument rack of the receiver alongside the MCS. Because of this, the enclosure included a variety of RFI/EMI suppression features including EMI/RFI gaskets, aluminum honeycomb air vents that act like cut-off waveguides for air-flow, a metal divider forming separate compartments for the SDR and computer compartments, and filtered power and signal interfaces (see Figure 4.34).

The primary task of the GBT310 DAQ is to coherently and simultaneouly sample the four channels of the Frontend Receiver and stream the I/Q (quadrature) data to the backend system. For the GBT310, the SDRs are configured for 20.48MHz of bandwidth per channel, amounting to 160 MSPS or 640 MBps of data (using single precision floats). The two B210 SDRs are synchronized to a common 10 MHz reference, which allows them to remain phase-coherent throughout the duration of the observations. However, while the system is coherent, the phase between the two SDRs is non-deterministic and will have an arbitrary offset each time the system restarts. This is due to both the Fractional-N PLL VCO that is used for the internal clock generation of the SDR, and also the difference in startup time for the USB data links. This synchronization problem can be compensated for by first finding the sample delay with the internal 4-channel coherent calibration source (using a special routine in the spectrograph that finds the closest integer sample delay), and then appropriately delaying or advancing the out-of-phase data-stream. This solution limits the phase variation to a maximum of one phase-wrap within the computed spectrum due to the fraction time-delay, but this can be removed in post-processing with phase calibration measurements.

The DAQ functionality is implemented with a `GNURadio` script, which configures the SDRs and provides a user interface for changing the sample delay. Additional settings include the center frequency (310 MHz), bandwidth (20.48 MHz), and receiver gain ($\sim$ 30 dB). The script delays the data for one of the SDRs, then interleaves the data, and transmits it over a TCP link to the backend that handles all of the signal processing.

Although these SDRs are well-suited for communications and rapid prototyping of flexible radio systems, they are not optimal for continuum and high-precision measurements (see Section 2.3.2). This is a consequence of the B210s, which, like most SDRs, use a zero-IF (or direct-downconversion) architecture. This approach uses a quadrature mixer for frequency conversion to provide both upper and lower sidebands about the central frequency (equal to the local oscillator frequency). However, these suffer from LO leakage (see Figure 3.10), limited sideband rejection, and enhanced noise from multi-rate filters and other digital signal processing techniques. An alternative is to use a conventional superheterodyne receiver architecture with explicit image rejection filters.

In anticipation for a possible upgraded version of the GBT310 receiver, a set of low-noise block downconverters were designed and fabricated that use a double-conversion design to maximize filter image rejection (see Appendix A.6). Additionally, these modules provide an extra ~ 36 dB of gain, which is necessary for the 4-channel high-speed ADC card used for testing (a GAGE RazorMax Express 16-bit 4-channel high-speed digitizer) with an input voltage range of $\pm 1V$. Using a 4-channel simulataneously sampled ADC (with a PCIe card or an RFSoc FPGA) would be the preferred way of implementing the data acquisition for the GBT310, as this direct approach avoids the complexity of phase-aligning the receiver channels.

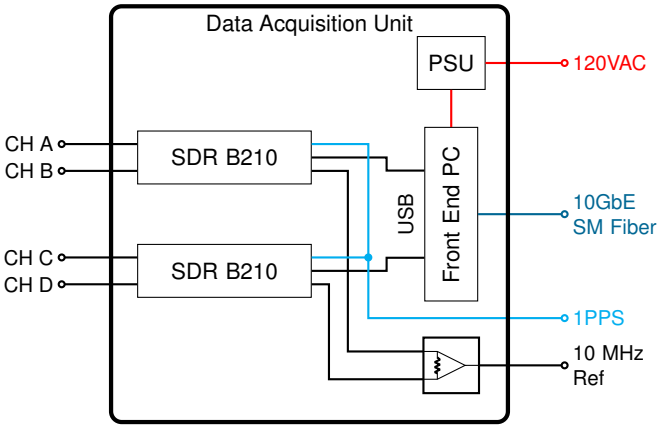

Figure 4.33: GBT310 Data Acquisition System Block Diagram

(a) RF/SDR Side

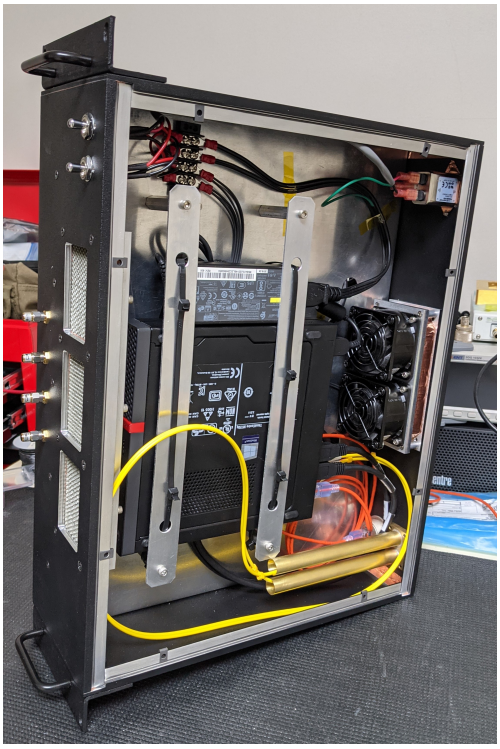

(b) Computer Side

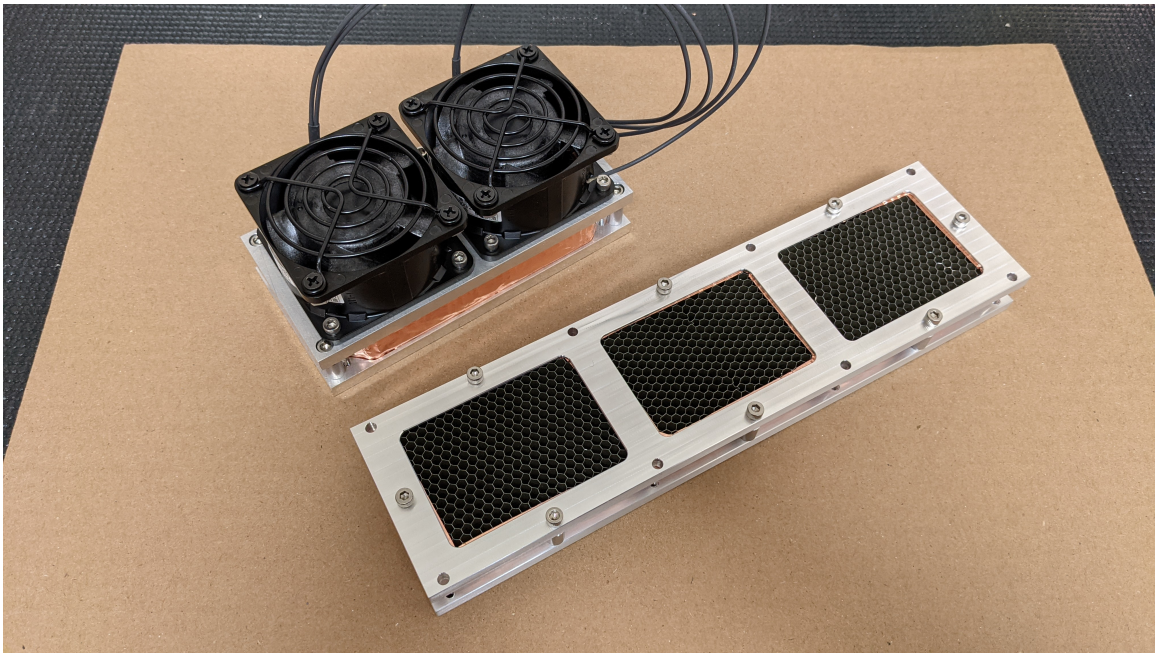

(c) RFI filtered vents using 3/4" thick with 0.125" cell-opening aluminum honeycomb

Figure 4.34: Pictures of the GTB310 Data Acquisition System Internals.

4.9 Backend System Software

The GBT310 Backend System Software (BSS) manages the operation of the instrument, data collection and digital signal processing, along with the user interfaces and data management. The core of the BSS is the main GBT310 Instrument Server application written in C/C++ that ingests the raw data streams from the fronted receiver on the telescope via a pair of full-duplex single mode fiber ethernet connections: one 10GbE link for the SDRs ($\sim$ 160 MSPS or $\sim$ 640 MBps) and one 10/100M link for the MCS. The collected data are then internally packetized into timestamped data chunks equal to the desired integration lenght/time along with the current device state and metadata from the MCS. These packets are distributed into and out of the FX (FFT then Correlate) thread pool via a pair of fixed-length circular buffers operating as a FIFO (First-In First-Out), which allows graceful handling of overflow conditions or timing variations. The processesed data are then broadcast to a variety of peripheral programs using a ZeroMQ (or ØMQ) Publish-Subscribe pattern, while a request-reply pattern is used for the control interface to the instrument supervisor thread.

FX Thread

It is worth explaining the FX thread design used for the GBT310 Instrument Server, as it performs the critical digital signal processing functions for the system. The FX thread is structured as a finite state machine with three selectable modes: idle, phase-alignment, and real-time FX correlation. The idle state allows the system to continue collecting data then simply discards it before further processing without otherwise disturbing the system. The second mode is phase-alignment, which performs a correlation based Time Delay Analysis (TDA; Smith (1997)) for finding the integer sample delay between the datastreams from the two coherent SDRs. This TDA was implemented using forward and reverse FFTs using the `FFTW3` and `FFTW++` C/C++ libraries (Frigo & Johnson, 2005). The sample delay can then be applied to the signal delay blocks in the frontend `GNURadio` script that controls the SDRs. This step allows the GBT310 receiver to become full-Stokes capable, as the datastreams are now synchronized to within a fraction of a sample (limiting the arbitrary phase difference to a single phase wrap), when using the quad-channel CCM v2 noise source as common phase reference. Finally, the real-time FX correlator de-interleaves the four SDR

channels, channelizes the complex valued timeseries using a 13-Tap (windowed-sinc filter) Polyphase Filter Bank with 256-Channels ($\Delta\nu = 80$ kHz), and cross-correlates and accumulates ($t_{int} \approx 0.1 - 1$ s) processed data for each unique pair of channels.

GUI

The Graphical User Interface is another important tool created to interact and monitor the real-time operation of the GBT310 Instrument. It was written in Python using the `PyQt` framework and `PyQtGraph`. Due to the network interface, it can operate both on remote computers or run local to the instrument server. The GUI provides state controls for configuring the signal path within the reciever amplifier and calibration modules, control of the spectrograph modes, and diagnostics readouts from device sensors and the instrument server application. Additionally, real-time plots of the metadata, and the amplitude, phase, and coherence of the auto/cross-correlated spectra are output. The data displayed by the GUI was extremely useful for engineering tests as well as for operating the instrument during observations.

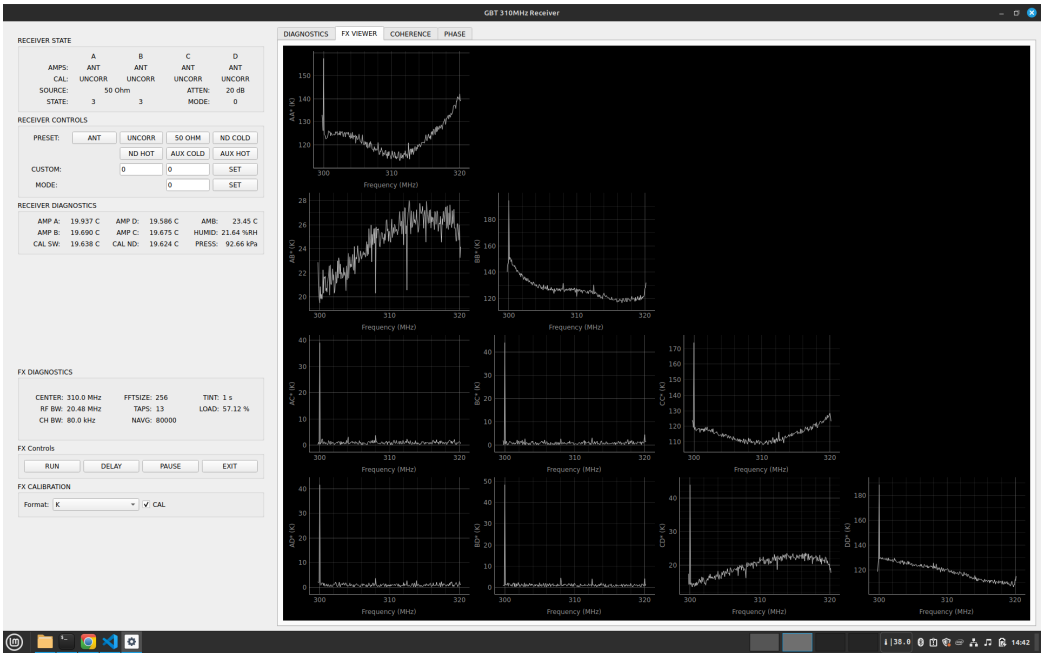

Figure 4.35: GBT310 Graphical User Interface

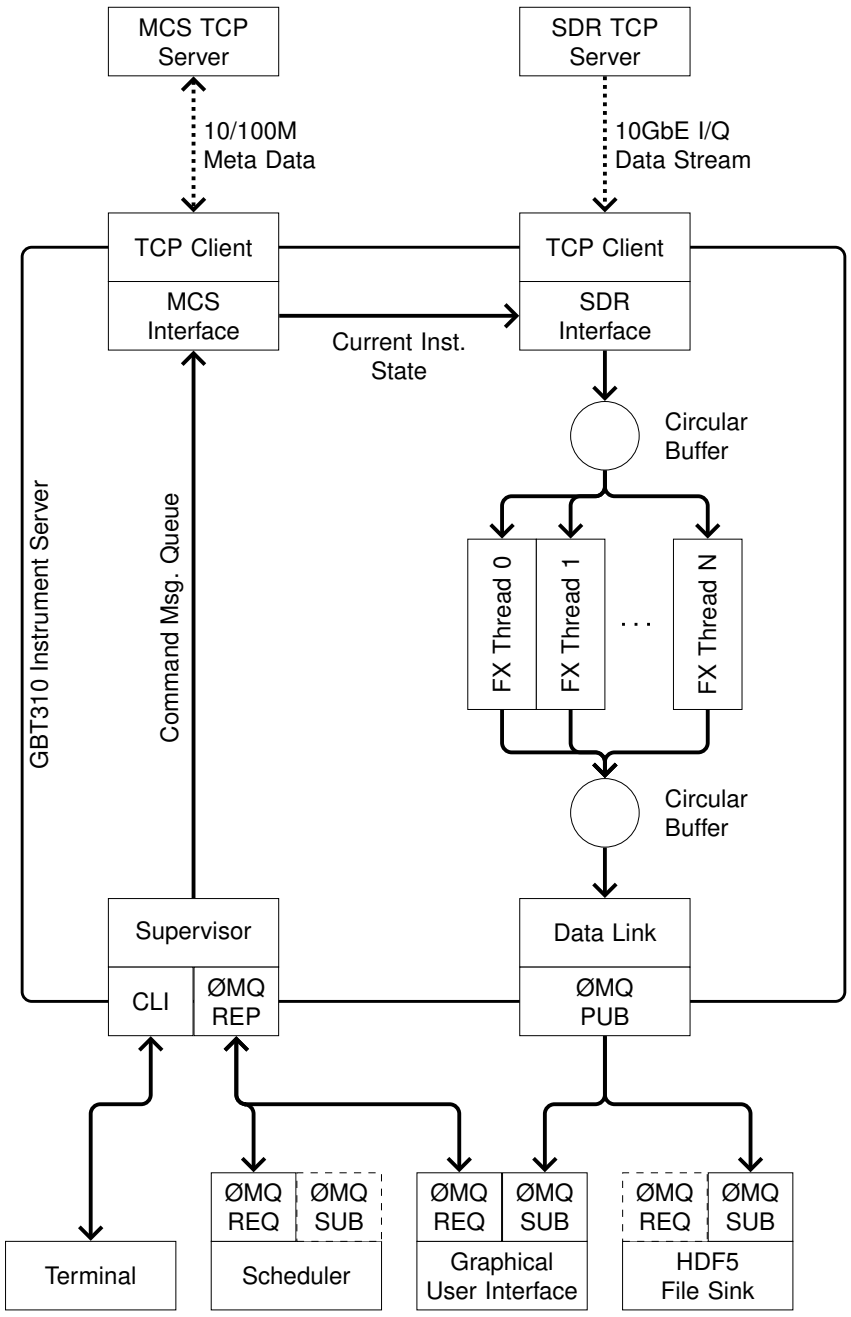

Figure 4.36: Software system block diagram of the GBT310

4.10 Commissioning

Final integration and lab testing of the GBT310 instrument was completed by mid-October 2022, and the instrument was transported to Green Bank, WV at the start of November 2022 for ground commissioning. The primary goal for these commissioning observations was to verify the stability and general operation of the GBT310 instrument (and the balanced correlation receiver approach in general) with zenith driftscans of the sky. These observations could then be compared to the simulated observations using the feed beam information and reference sky maps to validate the system and calibrations before proceeding to the first on-telescope deployment.

The large size of the feed also introduced logistical problems for this ground testing, because the feed was too large to fit within the typical outdoor test building mount. However, this was easily solved by building a custom test stand out of wood (see Figure 4.2). Fortunately, the test building could still be used to house the backend computer, 10 MHz Reference Oscillator, and Peltier controller, with all important interfaces connected as they would be when deployed on the telescope.

Start Date	Stop Date	Comments
2022-11-07	2022-11-08	First Deployment
2022-11-14	2022-11-14	Trouble Shooting Measurements
2023-05-15	2023-05-19	New Bulkhead Assembly
2023-11-13	2023-11-15	Driftscan with Balun Assembly
2023-11-15	2023-11-17	Driftscan in BCR Configuration
2023-11-29	2023-12-01	Driftscan with Balanced Amplifiers

Table 4.5: GBT310 Commissioning and Troubleshooting Observation

4.10.1 First Light – Denial and Anger

The first ground commissioning tests were conducted shortly after the instrument was delivered, beginning on Nov 7th, 2022 with deployment of the receiver, supporting backend hardware, and assembly of the feed on top. The system came online without any issues, but the first spectra produced in the tests showed a highly distorted, non-physical spectrum as opposed to the smoothly varying continuum that was expected (see Figure 4.38). This data showed a null in the cross-correlated dipole data

(AB^* and CD^*), which implied that there was at least a second frequency dependent continuum noise source. The null is formed through the superposition of vector noise sources: the expected differential or odd-mode (signals that are 180° out-of-phase) from the dipole and the even-mode (signals that are 0° out-of-phase) signal of unkown origin.

The data showed a severe issue that needed to be understood and solved before we could consider deploying the receiver on the GBT. Following the initial test measurement, a series of follow-up troubleshooting observations were performed a week later, with the system in different electrical or spectrograph configurations. These measurements primarily brought into question the nature of the SDRs' zero-IF downconversion scheme and multi-rate CIC (Cascaded integrator-comb) filtering (Hogenauer, 1981) that is used to downsample the base acquisition rate of the SDR to the desired output frequency. Because we are operating near the maximum bandwidth of the SDRs, the CIC filters will be generally low-order, thus increasing the aliased signals due to spectral folding. Evidence of this behavior was also seen in the Y-factor noise measurements of the system, which show enhancement towards the outer edges of the spectrum (see Figure 4.37 compared to Figure 4.24).

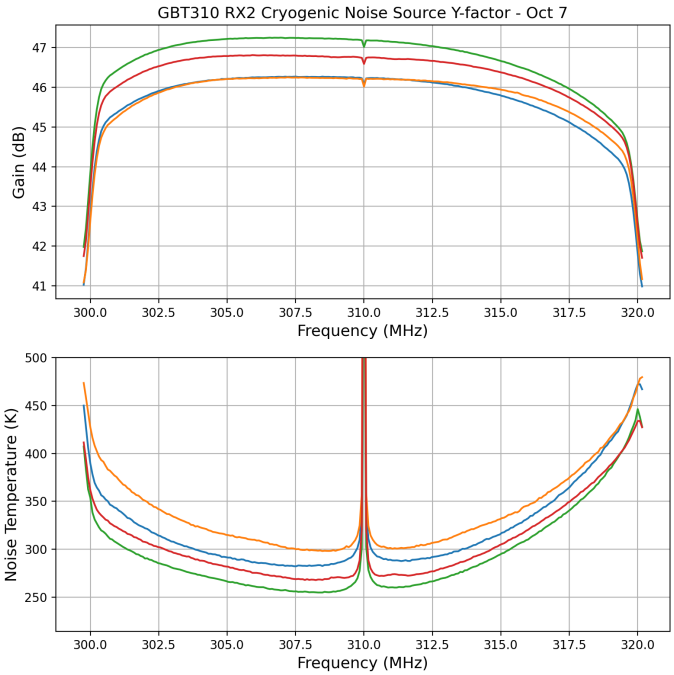

Figure 4.37: GBT310 Reference Y-factor Calibration

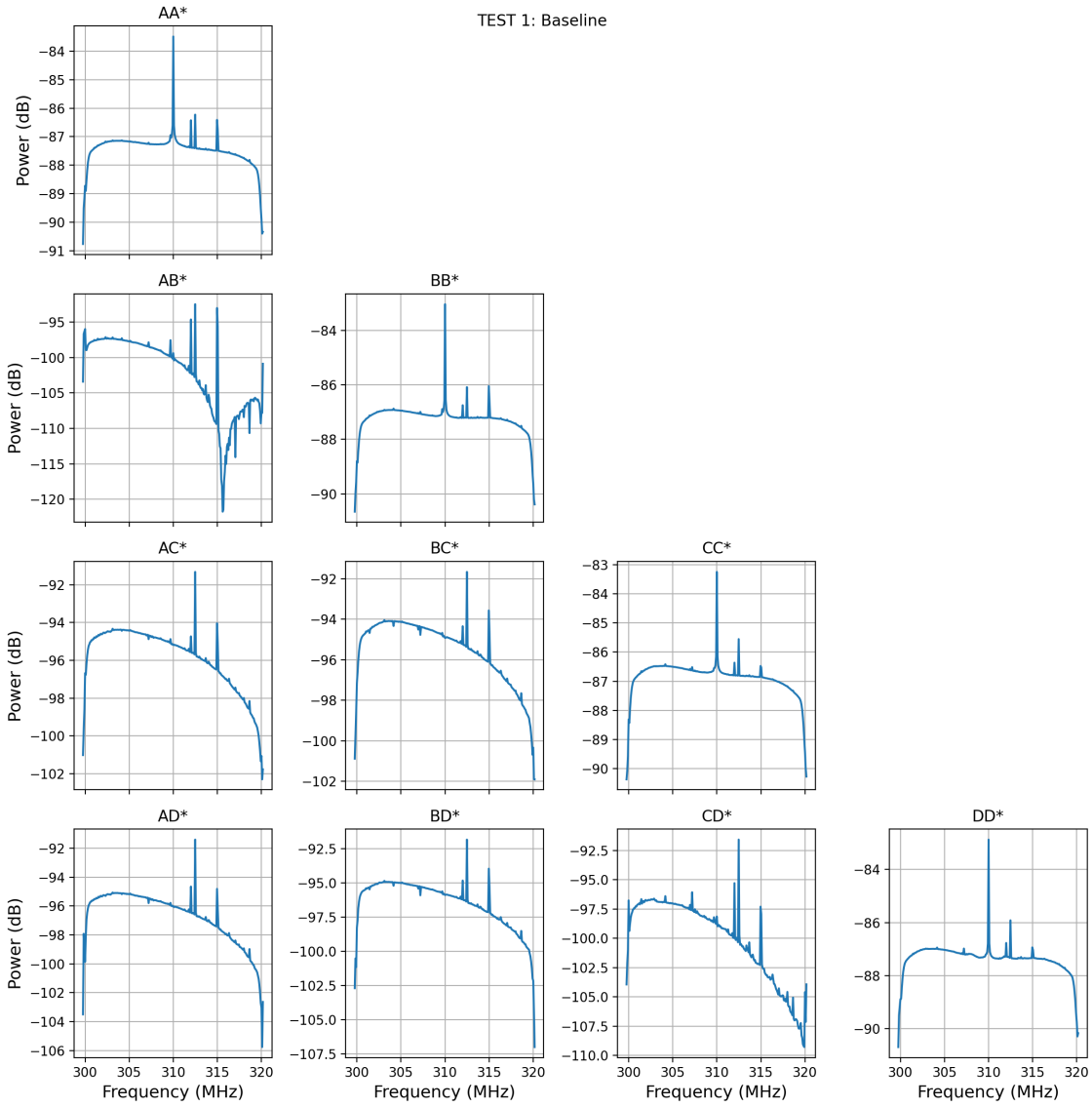

Figure 4.38: GBT310 Commissioning: Observed null in data. Signs of severe common/even-mode contamination

4.10.2 Troubleshooting – Bargaining and Depression

After the marginal results from the first light of the receiver, the goals shifted to localizing the exact root cause of the excess common-mode noise in the system. This included a drawn out troubleshooting campaign with lab and field trials, design and fabrication of new hardware and components, and contemplation. Sub-systems of the receiver were isolated and systematically tested to determine the limiting factors of the GBT310 receiver.

Software Defined Radios vs. Superheterodyne Receivers

After identifying that the SDRs are potentially problematic, an alternative data acquistion system was tested using superheterodyne downconverters (see Appendix A.6), a 4-channel ADC PCI card, and a simple DIY corner reflector antenna. The idea behind this test was to confirm whether or not the acquistion system was to blame for the excess even-mode continuum noise. For these tests, a superheterodyne downconverter was designed using a dual-conversion architecture to maximize image rejection. Additionally, a crude corner reflector antenna was built from hardware store parts (1/2" copper tubing, wood, and metal mesh) for local testing (see Figure 4.39). A two-channel measurement was then performed using the GBT310 Frontend as the first stage, followed by the downconverters and then sampled by a GAGE RazorMax Express 16-bit 4-channel high-speed digitizer at 200 MSPS.

The results of this experiment showed that the system Y-factor measurements were more consistent with those measured from the receiver frontend alone using a standalone Noise Figure Analyzer. This supports the general idea that the SDRs are contributing extra noise. Additionally, when the corner antenna was pointed out of the window, the data produced by this system showed a relatively smooth spectrum without any nulls as before (see Figure 4.39). However, when repeating this test with the original SDR backend, comparable data could be observed. This showed that although the SDRs are partially to blame, they are not the dominant source of the extra common-mode noise.

(a) Alternate GBT310 data acquisition system testing

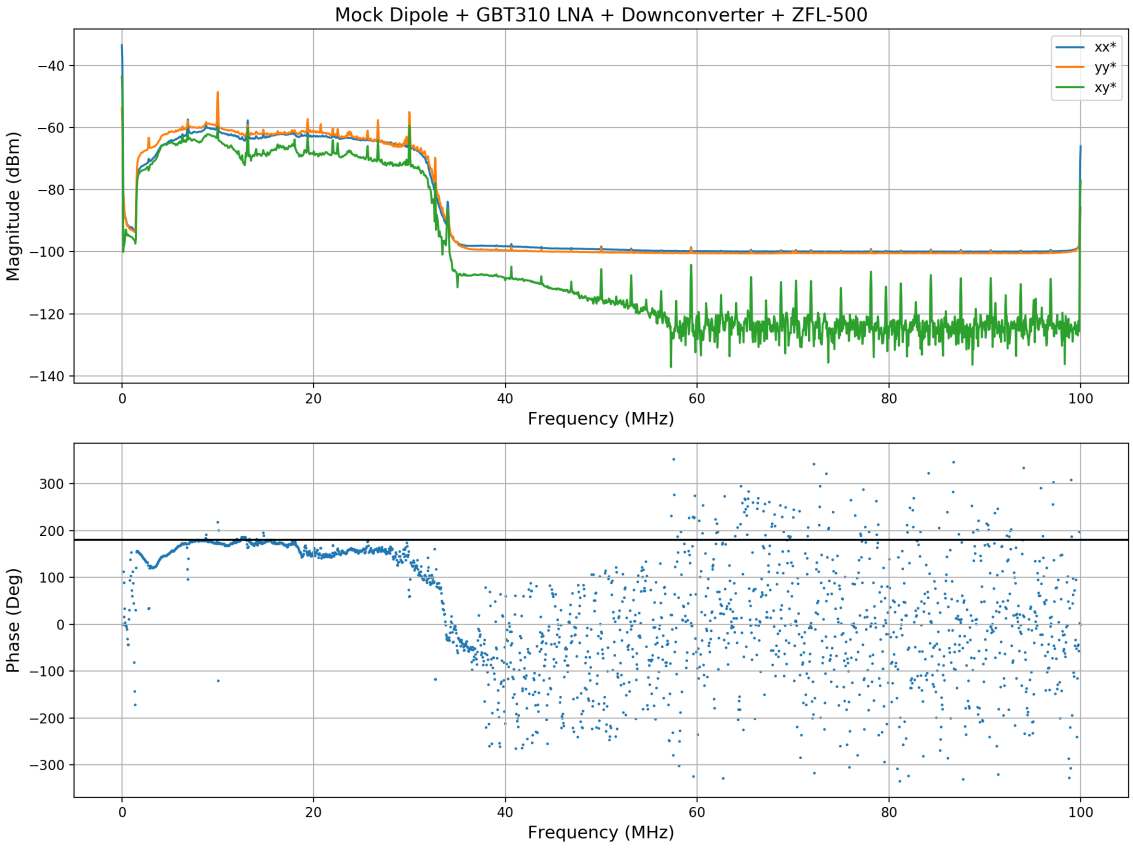

(b) Measured Auto/Cross-Correlations from corner reflector antenna

Figure 4.39: GBT310 Downconverter Testing

BMA Connectors and a New Bulkhead

Having largely ruled out the data acquisition system brought into question the behavior of the feed and frontend receiver, as well as the interface between the two. A new spring-loaded bulkhead assembly was designed and built to rule out the possibility of the BMA connectors not being seated well, which could otherwise produce unwanted reflections (see Figure 4.22). However, while this new bulkhead was an improvement, it did not change the system behavior significantly.

Common-mode Rejection using a Balun

As a fall-back solution, a balun assembly was developed to provide common-mode rejection from signals in the feed by synthesizing the dipoles using a 180° Hybrid Coupler and then splitting the signal into balanced outputs using a center-tapped transformer (see Figure 4.40). To be the least invasive, the balun assembly had to directly interface between the existing receiver and feed hardware, with the primary concern being the crossover of signals from each dipole. However, using this module would reduce the Balanced Correlation Receiver to a conventional Correlation Receiver along with adding about ~ 0.9 dB of ohmic loss that woud greatly reduce the signal-to-noise ratio of the receiver.

The balun assembly was tested with a pair of simple test antennas (the corner reflector and a crossed-dipole antenna) to evaluate the GBT310 system response in a variety of configurations (see figure 4.41) in early October 2023. Comparing the data showed that the test antennas had significantly higher antenna temperatures than the GBT310 feed, which is to be expected due to their crude nature (likely from poor impedance matching, or feedline line losses not included in the calibration solutions used). Curiously, the crossed-dipole using the BCR approach showed a null, while the corner reflector did not. Additionally, the phase behavior was closest to 180° for the crossed-dipole with the balun, follwed by the directly measured corner-reflector, the initial GBT310 data, and then minimially for the direct crossed-dipole measurements. Only the balun with the corner-reflector showed strong sinusoidal phase fluctuations across the band. This could be due to poor impedance matching, different excitation modes of the antenna structure, feedline lengths, and cross-coupling. However, using the balun appeared to be a promissing compromise, as it demonstrated the expected smooth amplitude and phase behavior.

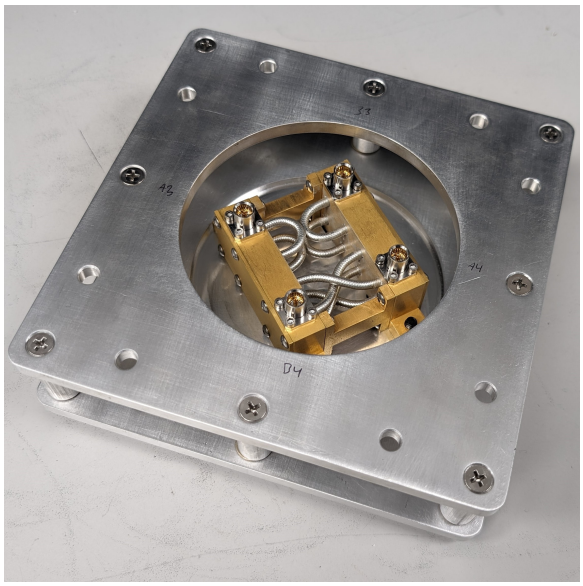

Figure 4.40: GBT310 Balun Assembly

Figure 4.41: GBT310 receiver driftscan measurements with and without the balun assembly using a pair of janky homebuilt antennas with balanced-outputs (a corner reflector dipole and a cross-dipole). NRAO CDL parking lot, Oct 2, 2023

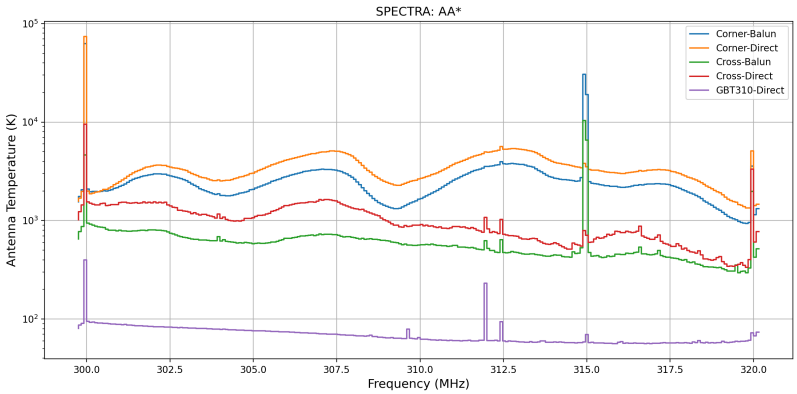

(a) Auto-Correlated Effective Antenna temperature

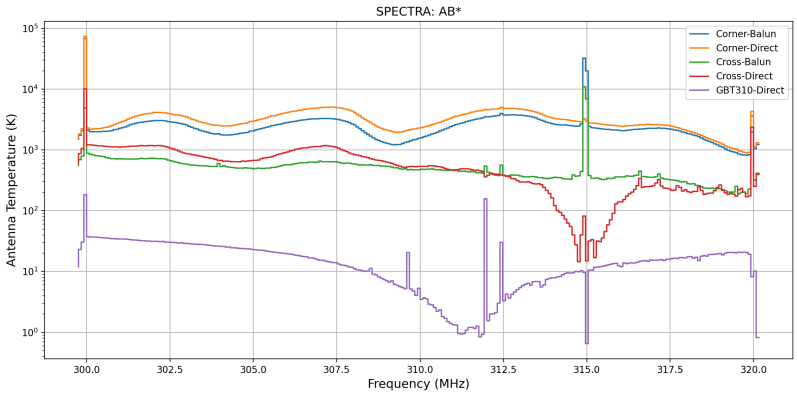

(b) Cross-Correlation Effective Antenna temperature

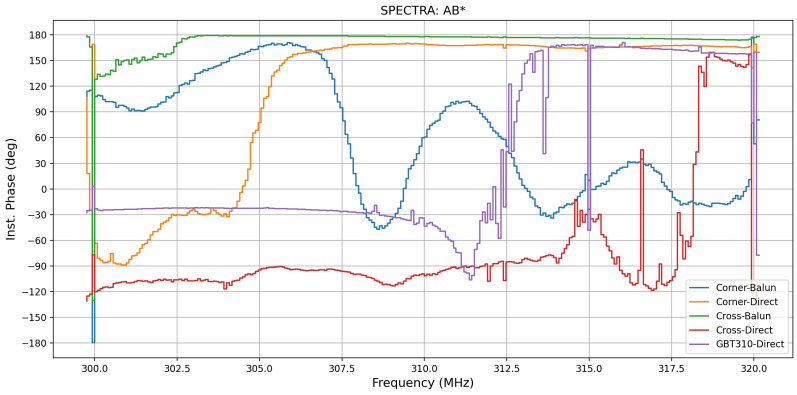

(c) Cross-Correlation Phase

Figure 4.42: Results from the parking lot tests of the GBT310 receiver and balun using the crude corner/crossed-dipoles compared to the prior field measurements (GBT310-Direct). The balun data appears smooth accross the full spectrum in both amplitude and at the correct phase (180°), while the direct BCR configuration shows a null only with the cross-dipole.

4.10.3 A Glimmer of Hope – Acceptance

After the long drawn-out lab troubleshooting campaign, further driftscans with the full receiver system at GBO were performed during mid- to late November 2023. These observations spanned approximately 2 days with the primary intent to evaluate the balun versus the initially proposed BCR configuration.

The first test used the new balun assembly to form the dipole and split the signal back into two balanced outputs. This allowed the system backend to be configured identically for the following BCR configuration tests. At first glance, the data in Figure 4.43 (top) show repeating features that are aligned when the brightest portion of the Galactic plane is overhead (LST $\sim$ 19 hrs), and are roughly stable accross frequency between an LST span from 12-24 hrs. However, from 0-12 hrs LST, the data behave erratically and show strong frequency dependent scaling. Additionally, the phase of the data was primarily 0° rather than the 180° noise expected from the splitter, thus the data were offset into negative temperatures. This is reminiscent to the observed noise superposition due to the power splitter in the calibration module, with an apparent offset of $\sim$ 150K (approximately the noise temperature of the frontend receiver).

The BCR configuration tests immediately followed to see how it compared to the balun measurement, while keeping everything elese identical. The data from the BCR configuration in Figure 4.44 (bottom) showed the observed null feature as expected. However, observing over multiple days revealed that it also tracked the peak of the Galactic plane! Furthermore, for the highest frequencies, the data and model were almost dead-on. Another interesting detail is that the temperature difference between frequencies was roughly constant, as opposed to in the balun measurements. This might point towards a minimum required noise power to overcome the self-generated noise in the balun configuration, while the BCR configuration has a persistent and frequency dependent common-mode (or out-of-phase) noise contribution.

Comparing the two datasets in Figures 4.43,4.44, 4.45, and 4.46 also reveals that the balun observations were less affected by RFI compared to the BCR configuration. Furthermore, the RFI in the BCR case was predominantly negative (higher common-mode noise) as opposed to the balun case. This may suggest that the common-mode signals in the feed were excited by local RFI.

This shows that the system can, in principle, work. However, more work would be

required to characterize the nature of the extra coherent noise generated within the system or in the feed. The next planned follow-up test to confirm whether the local radiation environment is contributing to the observed common-mode signal within the feed will require deployment on the GBT (scheduled for Summer 2024).

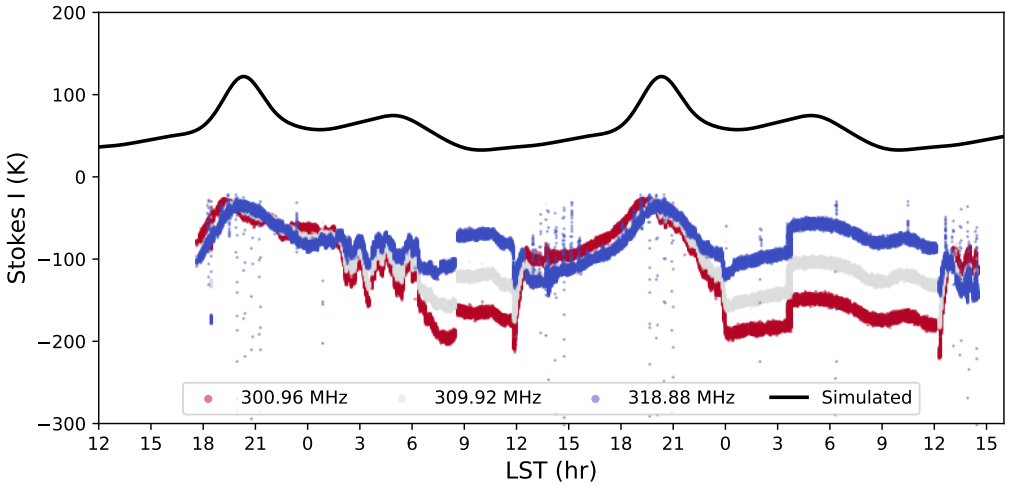

Figure 4.43: Observed Stokes I with the GBT310 and Balun Assembly.

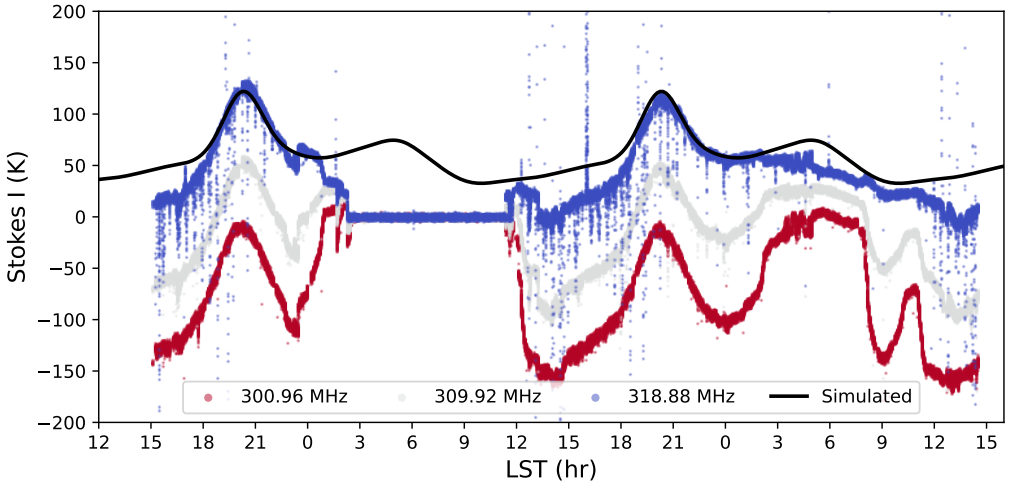

Figure 4.44: Observed Stokes I with the GBT310 in the BCR Configuration.

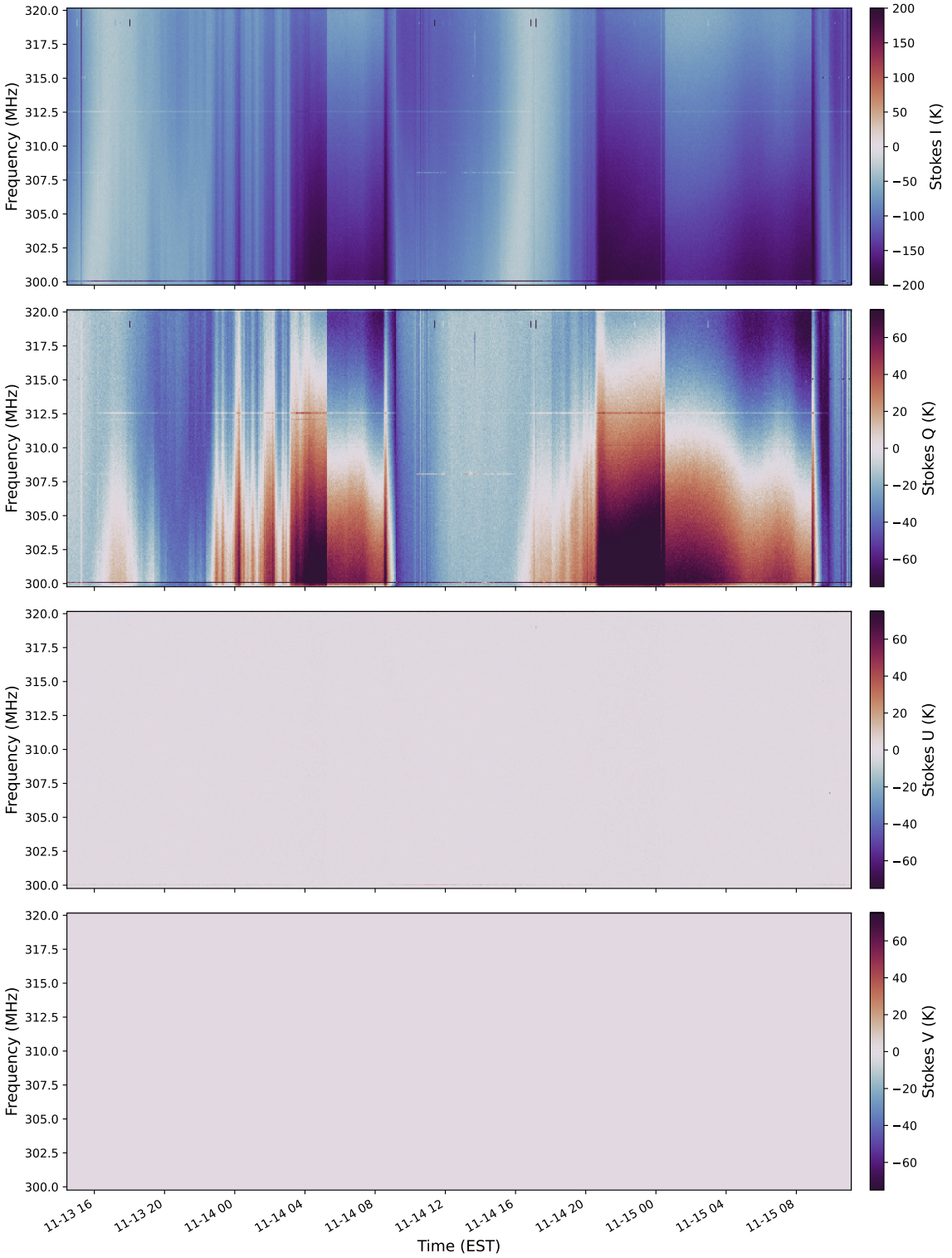

Figure 4.45: GBT310 Stokes Waterfall Plots

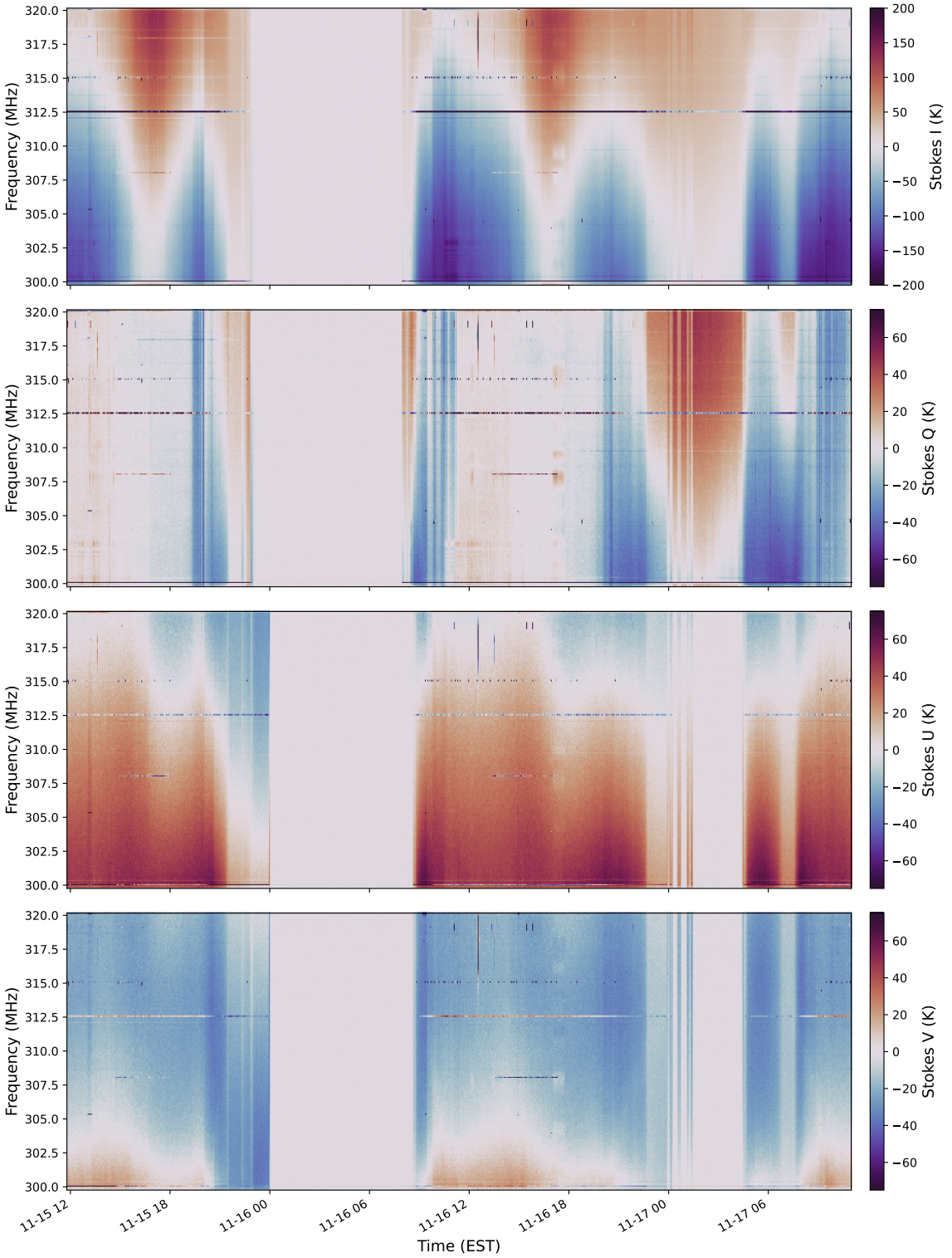

Figure 4.46: GBT310 Stokes Waterfall Plots

4.11 Discussion and Conclusion

This work presented the continuing efforts of fielding the highly optimized GBT310 receiver intended for a 310 MHz absolutely calibrated, zero-level map of the diffuse radio emission for the Northern hemisphere. The experimental nature of the balanced correlation receiver design and the physically large size of the high-edge taper feed required significant effort and time to develop and test. However, the development process allowed us to better understand the important device specifications for such a new receiver design and to explore the practical limitations thereof.

Part of this effort was the design, fabrication, and testing of a full end-to-end GBT receiver system. This included: a "breakable" feed structure designed to gracefully handle potential collisions without damaging the GBT structure; an integrated frontend receiver system with custom low-noise amplifiers, calibration sources, data acquistion system, and monitoring and controls hardware; and a real-time spectrograph and backend data processing software. However, during this development, a potentially fundamental limitation was discovered that is yet to be fully resolved at the time of writing.

During ground commissioning, the observed cross-correlation spectra required for the BCR approach showed unexpected frequency and time structure. This was determined to be due to common-mode continuum noise that was in superposition with the expected differential-mode signal from the dipoles, the sum of which can produce a null in amplitude, where the signal contributions are close in amplitude but 180° out-of-phase. Troubleshooting experiments indicated that this is primarily an issue with the feed structure and the interfacing with the frontend receiver, which has no inherent common-mode rejection. Thus, the common-mode signals could be generated by radial fields within the feed, potentially due to the leaky cavity of the short backfire antenna design. Additionally, the feedline assembly may allow for coaxial modes along the optical axis, inducing common-mode noise. Alternatively, it could be due to the finite coupling between adjacent and opposing monopoles that fundamentally limits the operation of a BCR approach by creating spurious signals from either self-generated noise from the receiver input or from the sky.

Although these issues are difficult to isolate with the current system, an on-telescope measurement is planned to determine if controlling the incident radiation applied to the feed could also control the modes within the feed. Additionally, a

higher-frequency (at a few GHz) test set-up with an echoic chamber may be necessary to systematically study the BCR receiver and evaluate the short backfire antenna or similar antenna structures that may inherently support undesired even/common-modes. The current observations provide a sliver of hope that the GBT310 receiver and the BCR approach can be made to function as expected.

Chapter 5

Summary and Future Work

5.1 Dynamically Induced Polarization

Dynamically Induced Polarization (DIP) offers a unique observational method for 21-cm experiments using broad-beam dipole antennas, because it provides additional constraints to the spatial anistropic foreground sky (Nhan et al., 2017, 2019). Such DIP observations help isolate terms within the beam-weighted sky because the cosmological 21-cm signal is expected to be isotropic and unpolarized on large scales, which in general, do not excite the symmetrical polarization leakage terms of a real antenna. I've shown how the relative alignment and dynamics of the antenna-sky system (e.g., the rotation of Earth, sweeping a zenith pointed beam through the sky once per sidereal day, or a rotating spacecraft in orbit) would further modulate the response of the system. This produces a set of characteristic waveforms or patterns in both total power and the three Stokes polarization quantities (I, Q, U, and V) that can be used in conjuction with singular value decomposition (SVD) based signal extraction methods (Tauscher et al., 2018b, 2020). These would have great constraining power compared to single polarization 21-cm experiments because more information is retained.

However, knowledge of the physical system is required including the response of the instrument and antenna beam, environmental coupling and obstructions, radio propagation effects, broadband knowledge of the sky brightness and intrinsic polarization, and more. Although the instrument and antenna may be simulated or otherwise empirically constrained, the in-situ behavior of the system may not be practically mea-

sureable, especially when including effects of soil, obstructions, scattering, or other environmental effects. Additionally, ionospheric and tropospheric conditions fluctuate on short timescales, which would cause atmospheric radio propagation effects to also fluctuate. Finally, knowing the foreground is of the utmost importance, as suggested by the observational results from the HB-CTP, since spatially variable spectral indices and intrinsic polarization readily impose systematic errors for all 21-cm experiments due to the degenerate nature of the measurement. The outcome of this experiment motivated the subsequent work included in my thesis, the design of a new radiometer architecture for improved stability and absolute polarimetric measurements, and the creation of a new absolutely calibrated zero-level map of the low-frequency radio sky. However, the utility of these projects extends beyond the field of 21 cm experiments.

5.2 Balanced Correlation Receivers

The novel Balanced Correlation Receiver (BCR) architecture could virtually eliminate gain instabilities (i.e., $1/f$ noise) and average system noise temperature offsets due to its unique method of forming a dipole. The BCR relies entirely on cross-correlation pairs of individual redundant-in-polarization antenna elements (e.g., monopoles of a dipole), while omitting all shared signal-paths such as baluns, transmission lines, or power splitters. The removal of these analog components can help improve the bandwidth and performance of the receiver, and any amplitude and phase variations can be compensated directly in the digital domain, unlike in analog components. I was able to theoretically show how such a recevier could be ideal for precision measurements that require long-term stability (potentially $t_{int} >$ few hours) and low measurement offsets, at the expense of twice the amount of receiver hardware.

However, BCRs are still highly experimental and will require further study. In particular, verifying the digital synthesis of the three predicted half-wave dipole beams is critical. Additionally, determining optimal feed/feedline structures and receiver interfaces for avoiding "multi-mode" excitation of the feed, such as the common-mode continuum noise observed in the GBT310 BCR, is necessary. I will be continuing the development of the BCR concept and will publish my work once the theoretical predictions are thoroughly explored by experimental measurements.

5.3 A 310 MHz Absolute Map

I was fortunate to become a core team member in the effort to create a new large-area, low-frequency ($\sim$ 300 MHz), absolutely calibrated zero-level map of the radio sky in late 2018 (PI – Jack Singal). Such a map would provide vital information and constraints for nearly all Galactic phenomena that manifest in the diffuse radio emission. Furthermore, it would be a timely contribution to the field, especially for ongoing experiments and observations of weak astrophysical signals such as the CMB or the cosmological 21-cm signal, which are observed through the bright and complex Galactic foreground.

To meet the scientific goals of this survey, a purpose-built receiver was required, specifically optimized for maximimum stability and minimal measurement uncertainty. As part of this effort, a complete end-to-end prime focus GBT receiver system was designed and implemented following the novel balanced correlation receiver concept. This included a custom high-taper feed, RF receiver and calibration hardware, monitoring and control circuitry, and data acquisition and signal processing software. This development is currently in the final stages of testing and commissioning. However, the BCR design has proven difficult to implement in practice and is showing signs of the coherent superposition of broadband noise sources, including the expected sky signal along with common-mode contamination.

My immediate future goal for the GBT310 receiver is on-telescope commissioning during Summer 2024 in preparation for the first science observations. These tests will help verify the deployment strategy and safety of the oversized custom feed at the prime focus of the GBT and also whether a controlled radiation environment will suppress the common-mode noise contamination observed during the ground commissioning tests. Secondary goals include incremental improvements of the backend receiver system that would replace the SDRs with a superheterodyne downconverter system and a four-channel, high-speed analog-to-digital-converter, along with a refinement of the software and controls of the system. Additionally, higher-frequency mockup tests of the BCR approach that are tied in with the verification of the generic balanced correlation receiver architecture will be necessary. The results of this work will be published upon completion.

Appendix A

Appendices for Chapter 5

A.1 Bending Stress in a Cantilever T-Beam

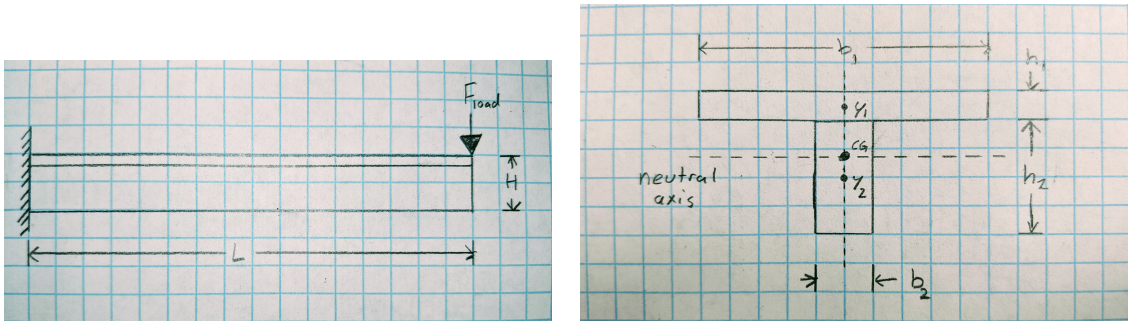

(a) (b)

Figure A.1

When a bending moment M is applied to the end of a cantilever beam, longitudinal stresses will develop following from Hook's Law with the expression (Timoshenko, 1983)

$$\sigma_x = \frac{M_z y}{I_z} \tag{A.1}$$

where σ_x is the longitudinal bending stress, M_z is the transverse bending moment, y is the distance from the neutral axis $\hat{y}$, and I_z is the second moment of area with respect to the neutral axis $\hat{z}$.

We find that the stress is statically determinate and depends only on the cross-section of the beam via I_z. The second moment of area for a T-beam cross-section

can be found by applying the Parallel Axis Theorem (Timoshenko, 1983):

$$\bar{I} = \sum (I_i + A_i d_i^2) \tag{A.2}$$

where I_i is the second moment of area about the *center of gravity* (CG) for each element composing the cross-section, A_i is the area of the element, and d_i is the distance between the elements CG and the net CG of the cross-section. Because the T-beam is symmetric about $\hat{z}$, we can simplify Equation A.2 to be only in terms of displacement in the transverse direction $\hat{y}$:

$$\bar{I} = \sum (I_i + A_i |y_i - \bar{y}|^2) \tag{A.3}$$

Thus, we can treat the T-beam used in the design as two rectangular elements each with a second moment of area:

$$I_i = \frac{bh^3}{12} \tag{A.4}$$

where b is the base length, and h is the height. The CG of the cross-section can be found using

$$\bar{y} = \frac{\sum A_i y_i}{\sum A_i} = \frac{b_1 h_1 (h_1/2) + b_2 h_2 (h_1 + h_2/2)}{b_1 h_1 + b_2 h_2} \tag{A.5}$$

The center of gravity for a T-beam cross-section will not coincide with the centroid. Thus, we must consider the height above (y_1) and below (y_2) the CG to evaluate the maximum tensile and compressive strength for the outermost longitudinal fibers:

$$(\sigma_t)_{max} = \frac{M_z y_1}{\bar{I}}, \quad (\sigma_c)_{max} = -\frac{M_z y_2}{\bar{I}} \tag{A.6}$$

where $(\sigma_t)_{max}$ is the max tensile stress, and $(\sigma_c)_{max}$ is the max compressive stress.

A.2 Finite Element Analysis Trials

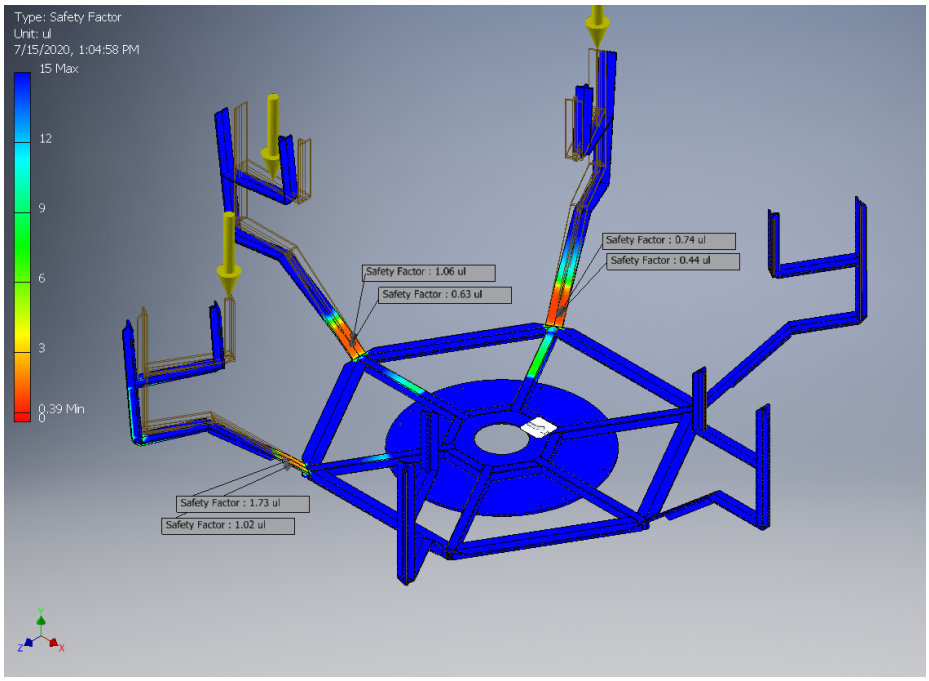

Figure A.2: GBT310 FEA static analysis for axial collision with 100 lbf point loads

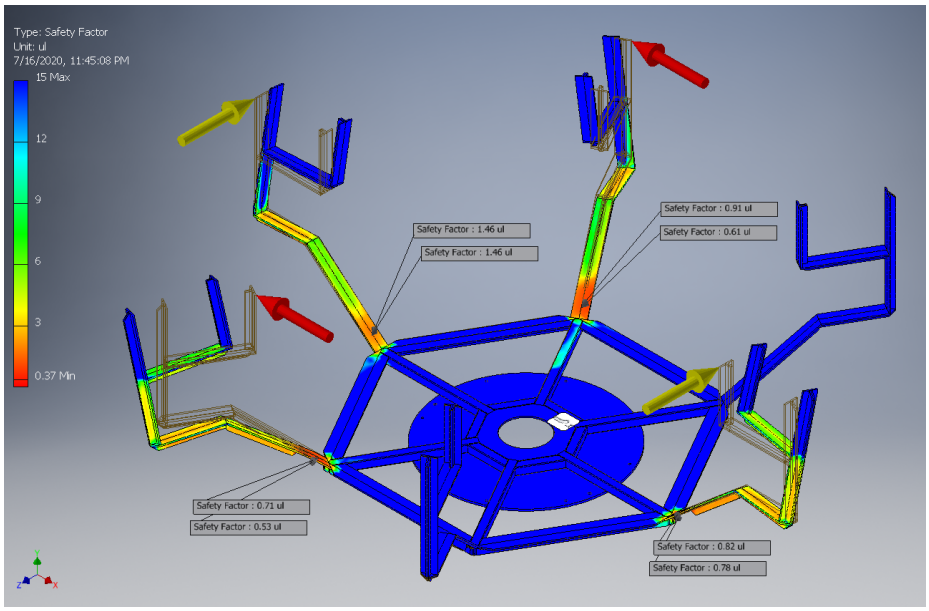

Figure A.3: GBT310 FEA static analysis for lateral collision with 100 lbf point loads

A.3 Vibration Modes of the GBT 310 MHz Feed

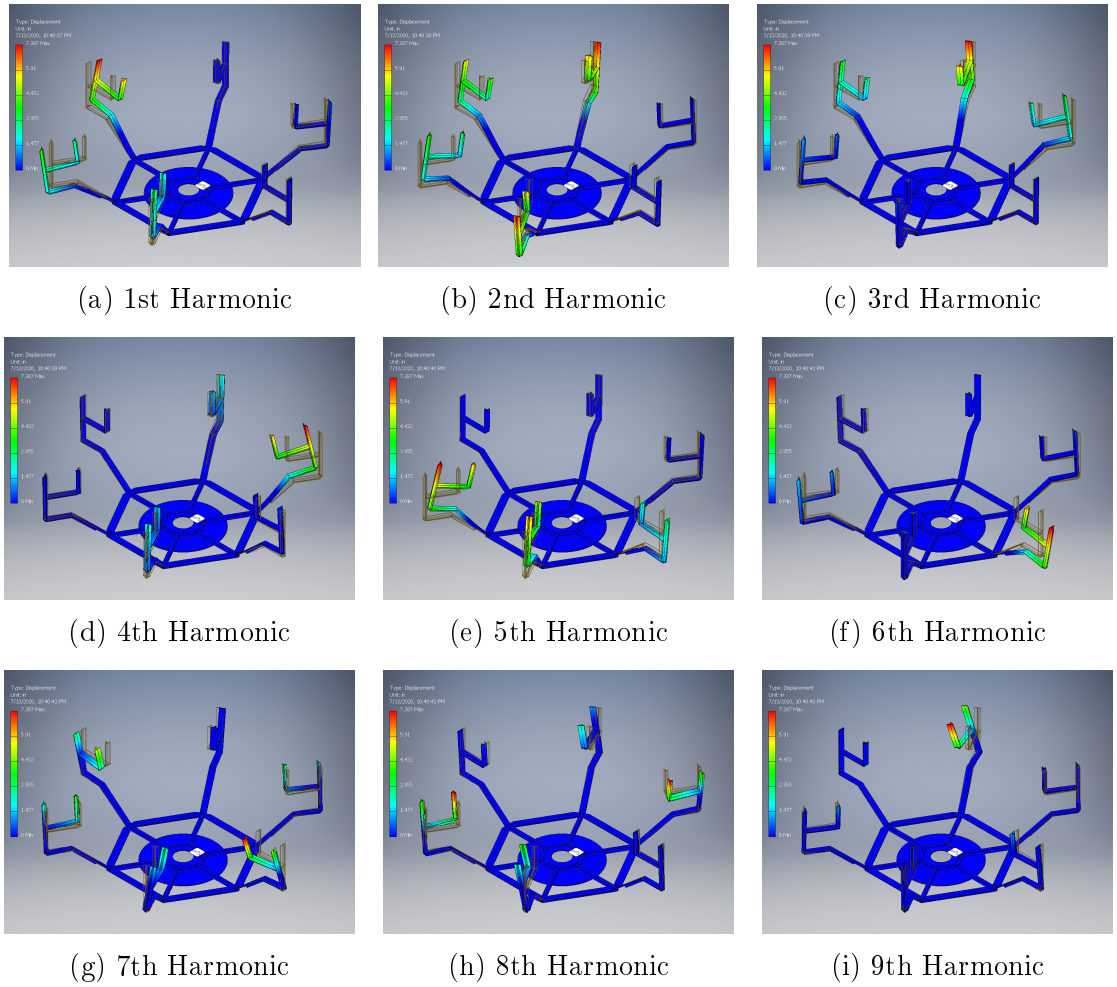

(a) 1st Harmonic (b) 2nd Harmonic (c) 3rd Harmonic

(d) 4th Harmonic (e) 5th Harmonic (f) 6th Harmonic

(g) 7th Harmonic (h) 8th Harmonic (i) 9th Harmonic

Figure A.4: Simulated modal shapes for the antenna frame.

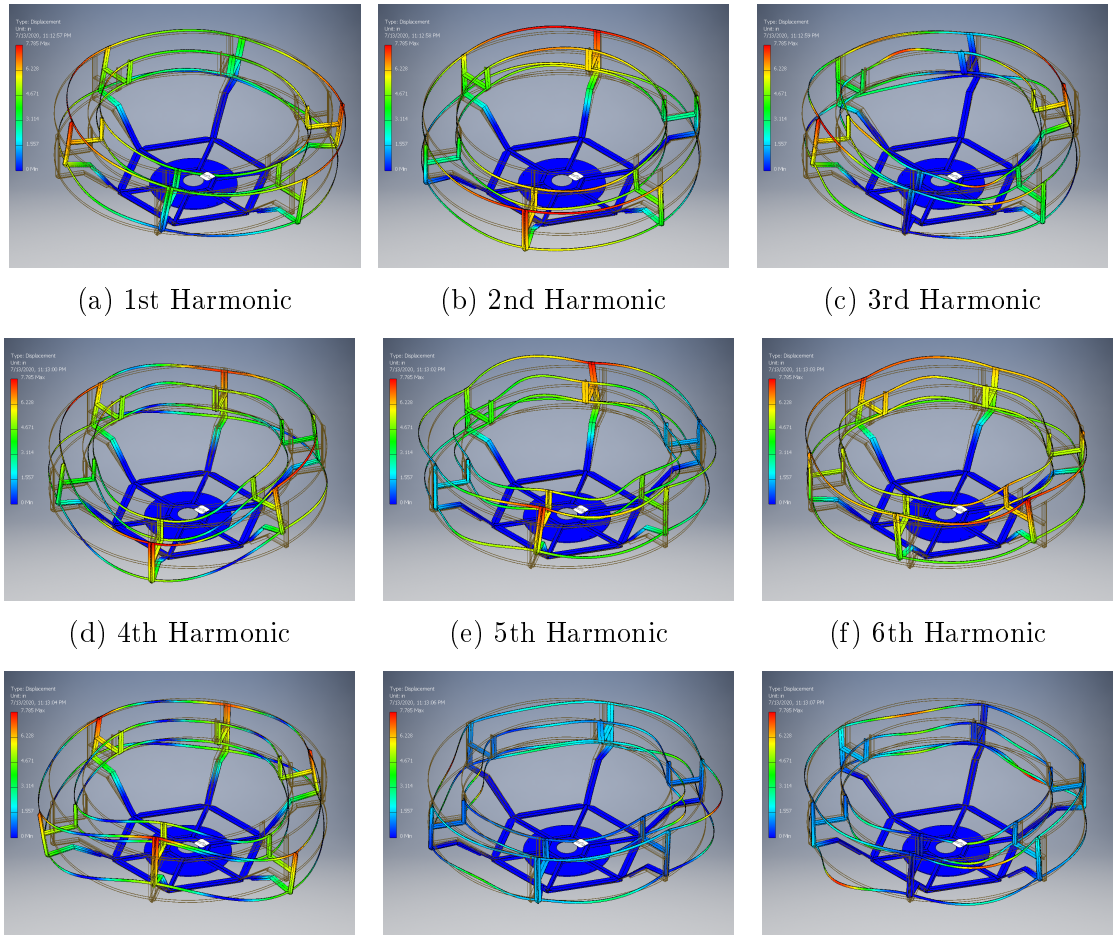

(a) 1st Harmonic (b) 2nd Harmonic (c) 3rd Harmonic

(d) 4th Harmonic (e) 5th Harmonic (f) 6th Harmonic

(g) 7th Harmonic (h) 8th Harmonic (i) 9th Harmonic

Figure A.5: Simulated modal shapes for the antenna frame and mesh reflector.

A.4 Calibrations

A.4.1 The Y-Factor Method

The Y-Factor method is a standard procedure for measuring the equivalent noise temperature of an amplifier by applying two matched loads (i.e., impedanced matched) at two significantly different equivalent noise temperatures (Pozar, 2012). Typically, a room-temperature 50Ω termination or resistor is used as the cold source, while a controlled noise generator (such as a noise diode) is used to produce excess noise, expressed as the excess noise ratio (ENR):

$$\mathrm{ENR(dB)} = 10\log_{10}\left(\frac{T_g - T_0}{T_0}\right) \tag{A.7}$$

where T_g and T_0 are the equivalent noise temperature of the generator and the matched load at room-temperature, respectively ($T_0 = 290$ K). The noise power N available at the output of an amplifier, or any two-port network, can be written as

$$N = Gk_B\Delta\nu(T_{in} + T_e) \tag{A.8}$$

where G, $\Delta\nu$ and T_e are, respectively, the gain, bandwidth, and additive equivalent noise temperature of the network, while $k_B \approx 1.381 \times 10^{-23}\,\mathrm{J}\cdot\mathrm{K}^{-1}$ is the Boltzmann constant, and T_g is the input noise from the generator. By providing two different known input noise sources to the network the Y-factor can be computed:

$$Y = \frac{N_{hot}}{N_{cold}} = \frac{T_{hot}^{ref} + T_e}{T_{cold}^{ref} + T_e} > 1 \tag{A.9}$$

The Y-factor can then be used to solve for the networks additive noise-temperature T_e:

$$T_e = \frac{T_{hot}^{ref} - YT_{cold}^{ref}}{Y - 1} \tag{A.10}$$

and the gain G directly from the input and output noise temperatures/powers:

$$G = \frac{N_{hot}^{out} - N_{cold}^{out}}{N_{hot}^{ref} - N_{cold}^{ref}} = \frac{T_{hot}^{out} - T_{cold}^{out}}{T_{hot}^{ref} - T_{cold}^{ref}} \tag{A.11}$$

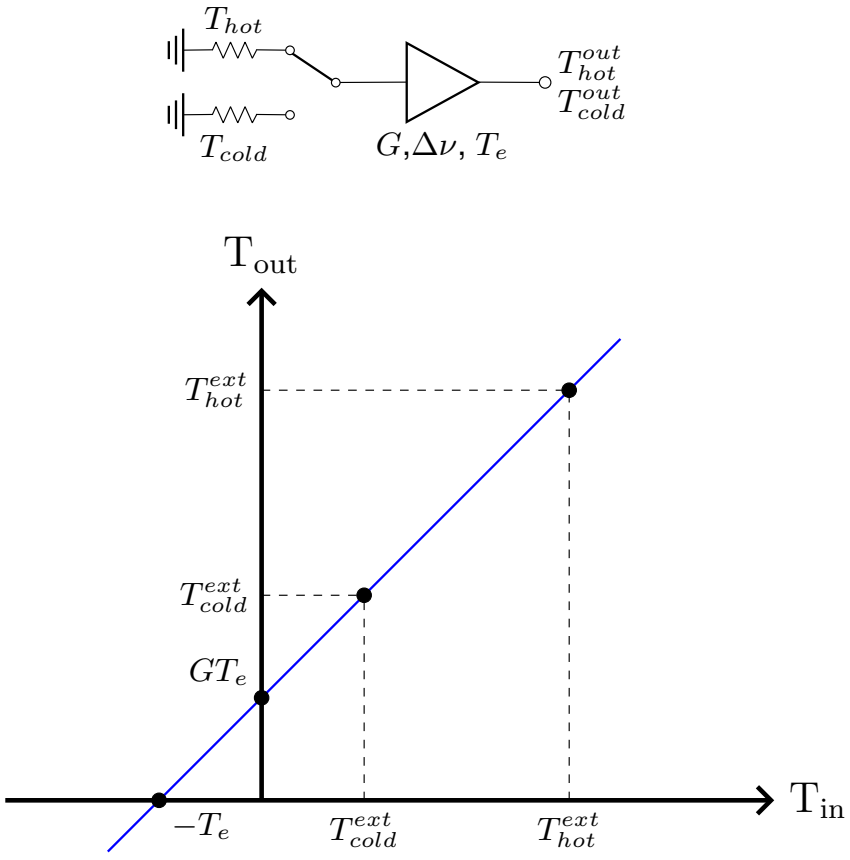

Figure A.6: The Y-Factor Method

A.5 A Discrete Low-Noise BJT Cascode Amplifier

A.5.1 Design

The cascode amplifer, comprised of a common-emitter (CE) and common-base (CB) transistor pair, is a common circuit configuration used to increase the bandwidth, reverse-isolation, and linearity compared to the simpler CE amplifier (Motchenbacher & Connelly, 1993; Gray, 2001). The bandwidth of a CE amplifier will generally be limited by the capacitive feedback that exists between the input (base) and output (collector), which form a low-pass filter with the source and load impedance. This is refered to as the Miller effect, which magnifies the parasitic capacitance (C_{CB}) between the collector and base of a BJT (Bipolar Junction Transistor) by the gain (g_m) of the CE amplifier and follows the relation $C_M = C_{CB}(1 + g_m)$. However, the cascode configuration minimizes this high-frequency feedback path because the voltage gain of the first-stage CE transistor is near unity. This is due to the low-input resistance of the second-stage CB transistor, which provides isolation for the following CB amplifier stage that does not suffer from the Miller effect. Thus, the cascode amplifier can not only achieve greater bandwidths, but also significantly greater reverse-isolation simplifying input and output matching.

A discrete cascode low-noise amplifier (LNA) was desiged for the second iteration of the GBT 310MHz frontend receiver system. This LNA was optimized to improve the input and output return loss and the reverse-isolation, after concerns about the first GBT310 LNA were identified during testing. The new cascode LNA was designed from discrete components using Keysight's *Advanced Design System* (ADS) physical circuit modeling program, using custom and vendor part models (see Figure A.8). The design was based around a pair of Infineon BFR380F high-linearity low-noise silicon NPN RF bipolar transistors, chosen for their low bias current and voltage along with a favorable Γ_{opt} at 310 MHz. These transitors were self-biased using a resistive feedback network along with inductive emitter degeneration on the CE-stage for improved input/output matching, stability, and linearity. The biased CE-CB transistors were accompanied by largely identical input/output matching networks that were implemented as 2nd-order LC bandpass filters. These matching networks provided both a low-loss impedance transformation from 50Ω to Γ_{opt} and Γ_{out}, along with a restriction of the operating frequency range centered around 310 MHz. Finally,

a low-value shunt capacitor between the CE-CB transmission was required to prevent the high-frequency oscillations that were observed in the complete amplifier chain by safely terminating signals > 1 GHz before amplification by the CB-stage. Although this was potentially a sub-optimal solution, it ensured unconditional stability at the expense of a slight increase in the noise figure and a reduction in gain.

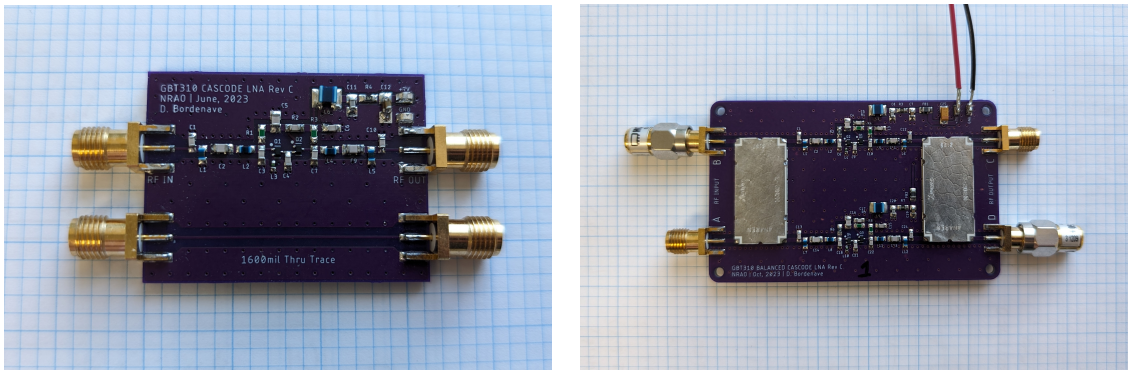

(a) Single-Ended (b) Balanced

Figure A.7: Custom 150-450 MHz Cascode Low Noise Amplifiers.

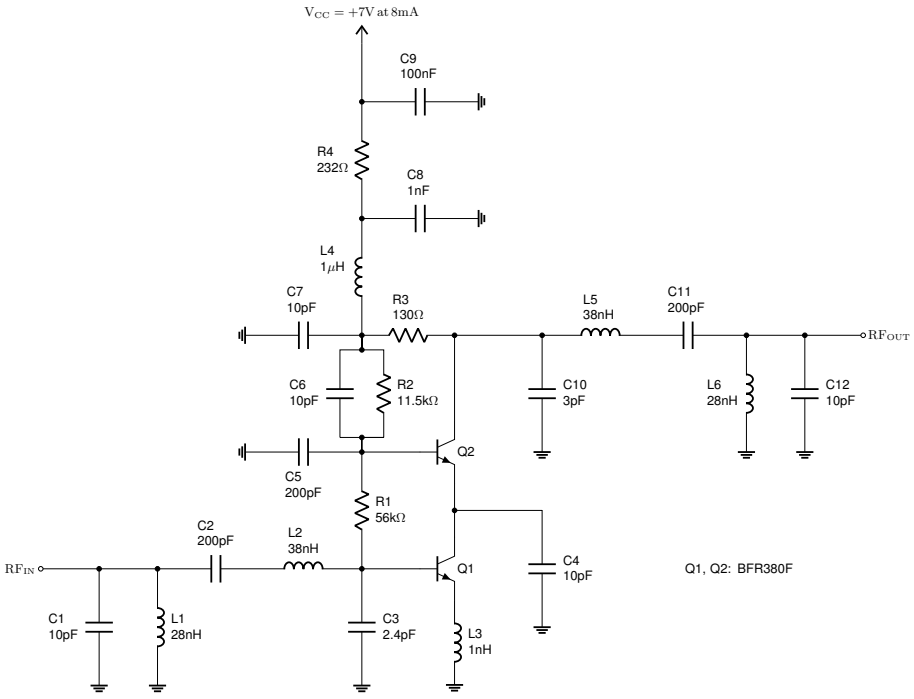

Figure A.8: Schematic of the custom low-noise cascode amplifier for 150-450 MHz

A.5.2 Single-Ended Performance Characteristics

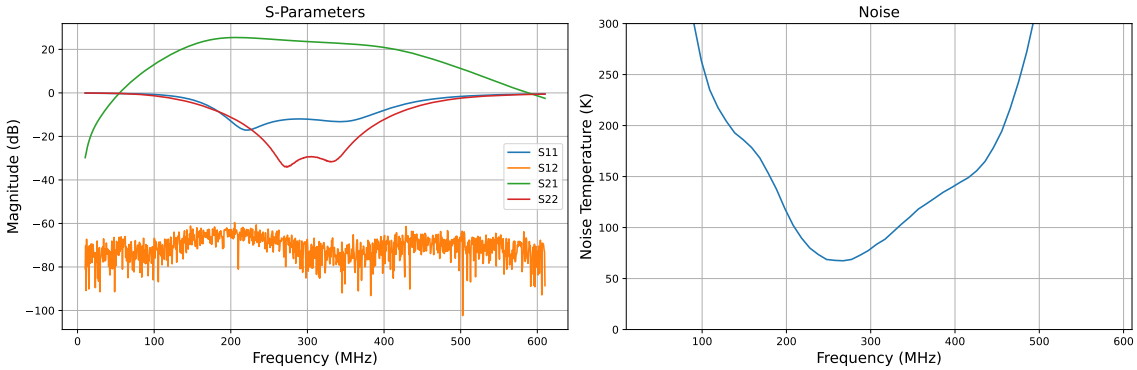

Figure A.9: S-parameter and noise temperature measurements for the Cascode LNA in the single-ended configuration

Parameter	Condition (MHz)	Min.	Typ.	Max.	Units
Frequency Range		200		400	MHz
DC Voltage			7		V
Current			8		mA
Gain	200-400	20.9	23.59	25.46	dB
	250-350	22.64	23.63	24.73	dB
Input Return Loss	200-400	-17.13	-12.92	-7.95	dB
	250-350	-13.80	-12.60	-11.97	dB
Output Return Loss	200-400	-34.08	-23.98	-11.19	dB
	250-350	-34.08	-30.38	-24.61	dB
Reverse Isolation	200-400	-93.27	-72.26	-59.59	dB
	250-350	-92.90	-72.38	-63.08	dB
Noise Figure	200-400	0.91	1.22	1.70	dB
	250-350	0.91	1.10	1.4	dB

Table A.1: Single-Ended Cascode LNA Performance Characteristics.

A.5.3 Balanced Amplifier Performance Characteristics

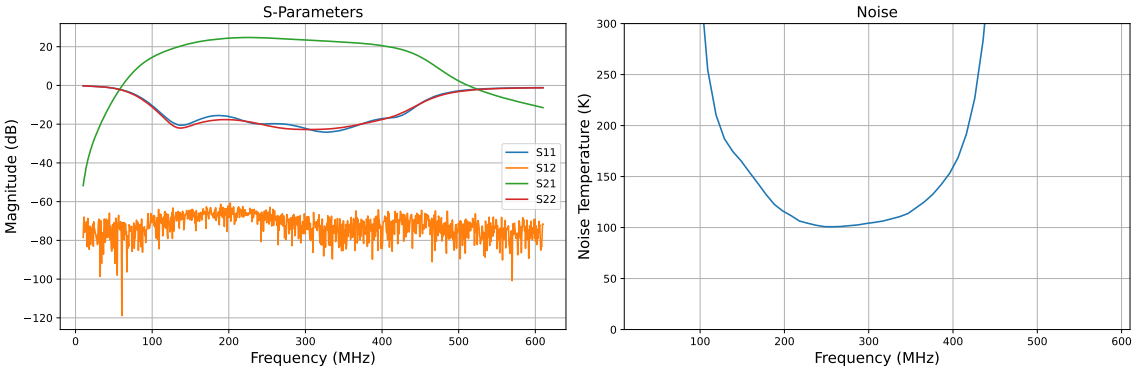

Figure A.10: S-parameter and noise temperature measurements for the cascode LNA in the balanced amplifier configuration

Parameter	Condition (MHz)	Min.	Typ.	Max.	Units
Frequency Range		100		450	MHz
DC Voltage			7		V
Current			8		mA
Gain	100-450	14.52	21.91	24.76	dB
	250-350	22.41	23.48	24.52	dB
Input Return Loss	100-450	-24.15	-18.68	-9.37	dB
	250-350	-24.15	-21.97	-19.72	dB
Output Return Loss	100-450	-22.82	-19.18	-9.41	dB
	250-350	-22.82	-22.27	-20.71	dB
Reverse Isolation	100-450	-89.74	-70.76	-60.71	dB
	250-350	-89.62	-73.05	-62.89	dB
Noise Figure	100-450	1.30	1.75	3.58	dB
	250-350	1.30	1.35	1.44	dB

Table A.2: Balanced Cascode LNA Performance Characteristics.

A.6 Low-Noise Block Downconverter

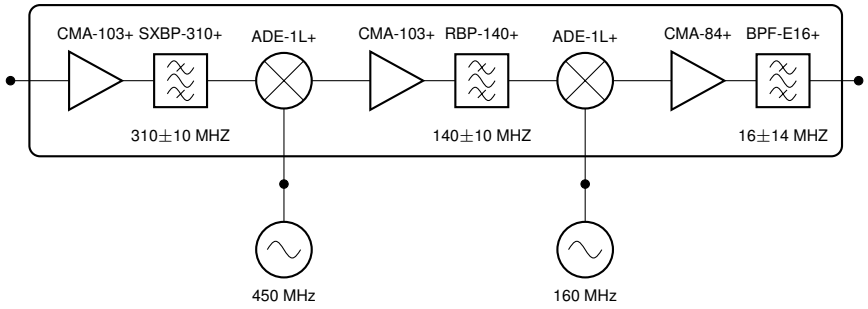

Figure A.11: GBT310 Superheterodyne Downconverter Block Diagram

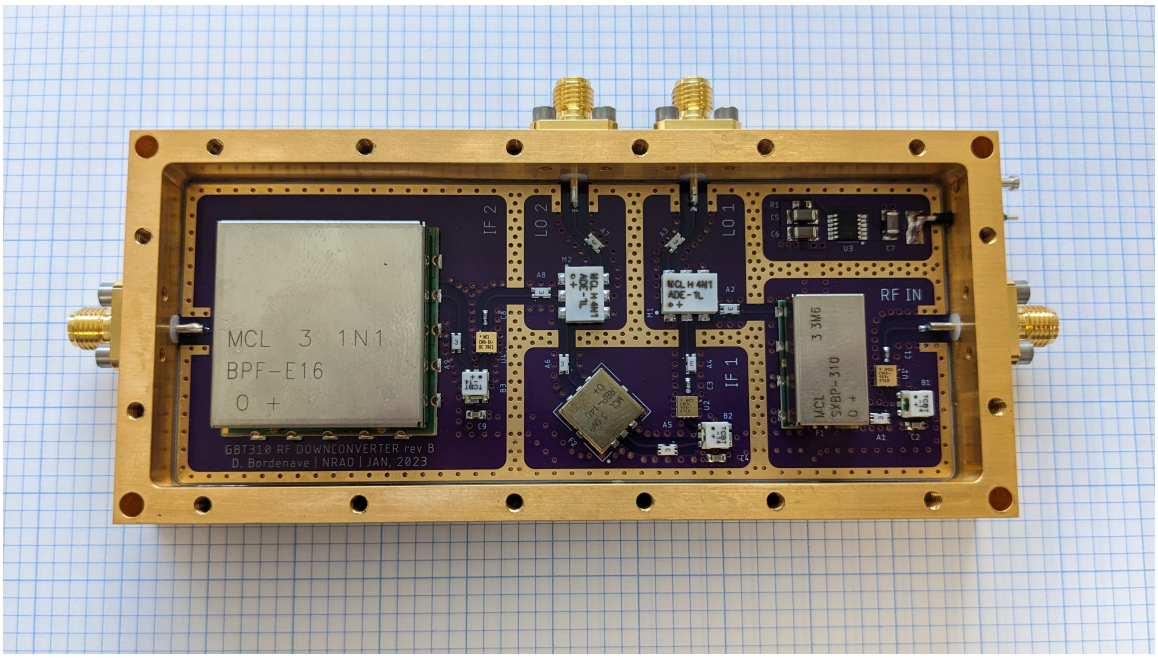

Figure A.12: GBT310 Superheterodyne Downconverter Assembly

References

Bailey, D. K. 1948, Terrestrial Magnetism and Atmospheric Electricity, 53, 41, doi: 10.1029/TE053i001p00041

Barkana, R. 2016, Physics Reports, 645, 1, doi: 10.1016/j.physrep.2016.06.006

Bassett, N., Rapetti, D., Tauscher, K., et al. 2021, The Astrophysical Journal, 923, 33, doi: 10.3847/1538-4357/ac1cde

Bernardi, G., McQuinn, M., & Greenhill, L. J. 2015, The Astrophysical Journal, 799, 90, doi: 10.1088/0004-637X/799/1/90

Bernardi, G., de Bruyn, A. G., Brentjens, M. A., et al. 2009, Astronomy and Astrophysics, 500, 965, doi: 10.1051/0004-6361/200911627

Bernardi, G., de Bruyn, A. G., Harker, G., et al. 2010, Astronomy and Astrophysics, 522, A67, doi: 10.1051/0004-6361/200913420

Bersanelli, M., Bensadoun, M., de Amici, G., et al. 1994, \textbackslashapj, 424, 517, doi: 10.1086/173910

Bersanelli, M., Mandolesi, N., Butler, R. C., et al. 2010, Astronomy and Astrophysics, 520, A4, doi: 10.1051/0004-6361/200912853

Biermann, P. L., Nath, B. B., Caramete, L. I., et al. 2014, Monthly Notices of the Royal Astronomical Society, 441, 1147, doi: 10.1093/mnras/stu541

Bittner, J. M., & Loeb, A. 2011, Journal of Cosmology and Astroparticle Physics, 2011, 038, doi: 10.1088/1475-7516/2011/04/038

Boithias, L. 1987, Radio wave propagation, rev. and updated edn. (London: North Oxford Academic)

Born, M., & Wolf, E. 2019, Principles of optics, seventh anniversary edition, 60th anniversary of first edition, 20th anniversary of seventh edition edn. (Cambridge, United Kingdom: Cambridge University Press)

Bowman, J. D., & Rogers, A. E. E. 2010, Nature, 468, 796, doi: 10.1038/nature09601

Bowman, J. D., Rogers, A. E. E., & Hewitt, J. N. 2008, The Astrophysical Journal, 676, 1, doi: 10.1086/528675

Bowman, J. D., Rogers, A. E. E., Monsalve, R. A., Mozdzen, T. J., & Mahesh, N. 2018, Nature, 555, 67, doi: 10.1038/nature25792

Bowman, J. D., Cairns, I., Kaplan, D. L., et al. 2013, Publications of the Astronomical Society of Australia, 30, e031, doi: 10.1017/pas.2013.009

Bradley, R. F., Tauscher, K., Rapetti, D., & Burns, J. O. 2019, The Astrophysical Journal, 874, 153, doi: 10.3847/1538-4357/ab0d8b

Budden, K. G. 1988, The propagation of radio waves: the theory of radio waves of low power in the ionosphere and magnetosphere, 1st edn. (Cambridge [England] ; New York: Cambridge University Press)

Burn, B. J. 1966, Monthly Notices of the Royal Astronomical Society, 133, 67, doi: 10.1093/mnras/133.1.67

Coc, A., & Vangioni, E. 2017, International Journal of Modern Physics E, 26, 1741002, doi: 10.1142/S0218301317410026

Condon, J. J., & Ransom, S. M. 2016, Essential radio astronomy, Princeton series in modern observational astronomy (Princeton: Princeton University Press)

Condon, J. J., Cotton, W. D., Fomalont, E. B., et al. 2012, The Astrophysical Journal, 758, 23, doi: 10.1088/0004-637X/758/1/23

Datta, A., Bradley, R., Burns, J. O., et al. 2016, The Astrophysical Journal, 831, 6, doi: 10.3847/0004-637X/831/1/6

DeBoer, D. R., Parsons, A. R., Aguirre, J. E., et al. 2017, Publications of the Astronomical Society of the Pacific, 129, 045001, doi: 10.1088/1538-3873/129/974/045001

Dicke, R. H. 1946, Review of Scientific Instruments, 17, 268, doi: 10.1063/1.1770483

Dowell, J., & Taylor, G. B. 2018, The Astrophysical Journal, 858, L9, doi: 10.3847/2041-8213/aabf86

Ehrenspeck, H. 1965, Proceedings of the IEEE, 53, 1138, doi: 10.1109/PROC.1965.4119

Evans, J. V., & Hagfors, T. 1968, Radar astronomy. https://ui.adsabs.harvard.edu/abs/1968raas.book.....E

Fang, K., & Linden, T. 2016, Journal of Cosmology and Astroparticle Physics, 2016, 004, doi: 10.1088/1475-7516/2016/10/004

Fixsen, D. J., Kogut, A., Levin, S., et al. 2011, \textbackslashapj, 734, 5, doi: 10.1088/0004-637X/734/1/5

Fornengo, N., Lineros, R. A., Regis, M., & Taoso, M. 2014, Journal of Cosmology and Astroparticle Physics, 2014, 008, doi: 10.1088/1475-7516/2014/04/008

Frigo, M., & Johnson, S. G. 2005, Proceedings of the IEEE, 93, 216

Friis, H. 1944, Proceedings of the IRE, 32, 419, doi: 10.1109/JRPROC.1944.232049

Fujimoto, K. 1964, IEEE Transactions on Microwave Theory and Techniques, 12, 203, doi: 10.1109/TMTT.1964.1125785

Furlanetto, S. R. 2006, Monthly Notices of the Royal Astronomical Society, 371, 867, doi: 10.1111/j.1365-2966.2006.10725.x

Gray, P. R., ed. 2001, Analysis and design of analog integrated circuits, 4th edn. (New York: Wiley)

Greenhill, L. J., & LEDA Collaboration. 2015, 225, 403.07. https://ui.adsabs.harvard.edu/abs/2015AAS...22540307G

Hamaker, J. P. 2000, Astronomy and Astrophysics Supplement Series, 143, 515, doi: 10.1051/aas:2000337

Hamaker, J. P., & Bregman, J. D. 1996, Astronomy and Astrophysics Supplement Series, 117, 161. https://ui.adsabs.harvard.edu/abs/1996A&AS..117..161H

Hamaker, J. P., Bregman, J. D., & Sault, R. J. 1996, Astronomy and Astrophysics Supplement Series, 117, 137. https://ui.adsabs.harvard.edu/abs/1996A&AS..117..137H

Harker, G. J. A., Pritchard, J. R., Burns, J. O., & Bowman, J. D. 2012, Monthly Notices of the Royal Astronomical Society, 419, 1070, doi: 10.1111/j.1365-2966.2011.19766.x

Haslam, C. G. T., Klein, U., Salter, C. J., et al. 1981, åp, 100, 209

Haslam, C. G. T., Salter, C. J., Stoffel, H., & Wilson, W. E. 1982, Astronomy and Astrophysics Supplement Series, 47, 1. https://ui.adsabs.harvard.edu/abs/1982A&AS...47....1H

Haykin, S. S. 1996, Adaptive filter theory, 3rd edn., Prentice Hall information and system sciences series (Upper Saddle River, N.J: Prentice Hall)

Hills, R., Kulkarni, G., Meerburg, P. D., & Puchwein, E. 2018, Nature, 564, E32, doi: 10.1038/s41586-018-0796-5

Hogenauer, E. 1981, IEEE Transactions on Acoustics, Speech, and Signal Processing, 29, 155, doi: 10.1109/TASSP.1981.1163535

Hooper, D., Belikov, A. V., Jeltema, T. E., et al. 2012, Physical Review D, 86, 103003, doi: 10.1103/PhysRevD.86.103003

Howell, T. F., & Shakeshaft, J. R. 1966, Nature, 210, 1318, doi: 10.1038/2101318a0

Hwang, Y.-J., Lin, C.-C., Srikanth, S., et al. 2019, in 2019 URSI Asia-Pacific Radio Science Conference (AP-RASC), 1–4, doi: 10.23919/URSIAP-RASC.2019.8738400

Jansky, K. G. 1933, Nature, 132, 66, doi: 10.1038/132066a0

Jishnu Nambissan, T., Subrahmanyan, R., Somashekar, R., et al. 2021, Experimental Astronomy, 51, 193, doi: 10.1007/s10686-020-09697-2

Johnson, J. B. 1928, Physical Review, 32, 97, doi: 10.1103/PhysRev.32.97

Johnson, R. C., & Jasik, H., eds. 1993, Antenna engineering handbook, 3rd edn. (New York, NY: McGraw-Hill)

Jonas, J. L., Baart, E. E., & Nicolson, G. D. 1998, Monthly Notices of the Royal Astronomical Society, 297, 977, doi: 10.1046/j.1365-8711.1998.01367.x

Jordan, E. C., & Balmain, K. G. 1968, Electromagnetic waves and radiating systems, 2nd edn., Prentice-Hall electrical engineering series (Englewood Cliffs, NJ: Prentice-Hall)

Kelley, M. C. 2009, The earth's ionosphere: plasma physics and electrodynamics, second edition edn., International geophysics series No. volume 96 (Amsterdam Boston Heidelberg London New York Oxford Paris San Diego San Francisco Singapore Sydney Tokyo: Academic Press)

Keshner, M. 1982, Proceedings of the IEEE, 70, 212, doi: 10.1109/PROC.1982.12282

Klopfenstein, R. 1956, Proceedings of the IRE, 44, 31, doi: 10.1109/JRPROC.1956.274847

Kogut, A. 2012, The Astrophysical Journal, 753, 110, doi: 10.1088/0004-637X/753/2/110

Kogut, A., Fixsen, D. J., Levin, S. M., et al. 2011, The Astrophysical Journal, 734, 4, doi: 10.1088/0004-637X/734/1/4

Kraus, J. D. 1988, Antennas, 2nd edn., McGraw-Hill series in electrical engineering Radar and antennas (New York, NY: McGraw-Hill)

—. 1991, Electromagnetics, 4th edn. (New York: McGraw Hill)

Kraus, J. D., & Tiuri, M. 1966, Radio astronomy (New York: McGraw-Hill)

Lin, C.-C., Hwang, Y.-J., & Srikanth, S. 2012, in 2012 Asia Pacific Microwave Conference Proceedings, 1346–1348, doi: 10.1109/APMC.2012.6421915

Machin, K., Ryle, M., & Vonberg, D. 1952, Proceedings of the IEE - Part III: Radio and Communication Engineering, 99, 127, doi: 10.1049/pi-3.1952.0033

Madau, P., Meiksin, A., & Rees, M. J. 1997, The Astrophysical Journal, 475, 429, doi: 10.1086/303549

Maeda, K., Alvarez, H., Aparici, J., May, J., & Reich, P. 1999, åps, 140, 145, doi: 10.1051/aas:1999413

Massobrio, G., & Antognetti, P. 1993, Semiconductor device modeling with SPICE, 2nd edn. (New York: McGraw-Hill)

Mertens, F. G., Mevius, M., Koopmans, L. V. E., et al. 2020, Monthly Notices of the Royal Astronomical Society, 493, 1662, doi: 10.1093/mnras/staa327

Mirocha, J., Furlanetto, S. R., & Sun, G. 2017, Monthly Notices of the Royal Astronomical Society, 464, 1365, doi: 10.1093/mnras/stw2412

Monsalve, R. A., Rogers, A. E. E., Bowman, J. D., & Mozdzen, T. J. 2017, The Astrophysical Journal, 835, 49, doi: 10.3847/1538-4357/835/1/49

Morgan, M. A., Fisher, J. R., & Boyd, T. A. 2010, IEEE Transactions on Microwave Theory and Techniques, 5617324, doi: 10.1109/TMTT.2010.2086510

Motchenbacher, C. D., & Connelly, J. A. 1993, Low-noise electronic system design (New York: Wiley)

Nguyen, H., Dawson, J. R., Miville-Deschênes, M.-A., et al. 2018, The Astrophysical Journal, 862, 49, doi: 10.3847/1538-4357/aac82b

Nhan, B. D., Bordenave, D. D., Bradley, R. F., et al. 2019, The Astrophysical Journal, 883, 126, doi: 10.3847/1538-4357/ab391b

Nhan, B. D., Bradley, R. F., & Burns, J. O. 2017, The Astrophysical Journal, 836, 90, doi: 10.3847/1538-4357/836/1/90

Nita, G. M., & Gary, D. E. 2010, Monthly Notices of the Royal Astronomical Society: Letters, 406, L60, doi: 10.1111/j.1745-3933.2010.00882.x

Nyquist, H. 1928, Physical Review, 32, 110, doi: 10.1103/PhysRev.32.110

Ohmori, S., Miura, S., Kameyama, K., & Yoshimura, H. 1983, IEEE Transactions on Antennas and Propagation, 31, 644, doi: 10.1109/TAP.1983.1143099

Orhaug, T., & Waltman, W. 1963, National Radio Astronomy Observatory Publications, 1, 179. https://ui.adsabs.harvard.edu/abs/1963NRAOP...1..179O

Orlando, E. 2018, Monthly Notices of the Royal Astronomical Society, 475, 2724, doi: 10.1093/mnras/stx3280

Pacholczyk, A. G. 1970, Radio astrophysics: nonthermal processes in galactic and extragalactic sources, A series of books in astronomy and astro-physics (San Francisco: W. H. Freeman and Comp)

Parsons, A. R., Backer, D. C., Foster, G. S., et al. 2010, The Astronomical Journal, 139, 1468, doi: 10.1088/0004-6256/139/4/1468

Patra, N., Subrahmanyan, R., Raghunathan, A., & Udaya Shankar, N. 2013, Experimental Astronomy, 36, 319, doi: 10.1007/s10686-013-9336-3

Pauliny-Toth, I. I. K., & Shakeshaft, J. R. 1962, Monthly Notices of the Royal Astronomical Society, 124, 61, doi: 10.1093/mnras/124.1.61

Pawsey, J. L., McCready, L. L., & Gardner, F. F. 1951, Journal of Atmospheric and Terrestrial Physics, 1, 261, doi: 10.1016/0021-9169(51)90001-3

Penrose, R. 1955, Proceedings of the Cambridge Philosophical Society, 51, 406, doi: 10.1017/S0305004100030401

Philip, L., Abdurashidova, Z., Chiang, H. C., et al. 2019, Journal of Astronomical Instrumentation, 8, 1950004, doi: 10.1142/S2251171719500041

Piepmeier, J. R., Long, D. G., & Njoku, E. G. 2008, IEEE Transactions on Geoscience and Remote Sensing, 46, 516, doi: 10.1109/TGRS.2007.909597

Planck Collaboration, Adam, R., Ade, P. A. R., et al. 2016, Astronomy and Astrophysics, 594, A10, doi: 10.1051/0004-6361/201525967

Pozar, D. M. 2012, Microwave engineering, 4th edn. (Hoboken, NJ: Wiley)

Pritchard, J. R., & Loeb, A. 2010, Physical Review D, 82, 023006, doi: 10.1103/PhysRevD.82.023006

Rapetti, D., Tauscher, K., Mirocha, J., & Burns, J. O. 2020, The Astrophysical Journal, 897, 174, doi: 10.3847/1538-4357/ab9b29

Reich, P., & Reich, W. 1986, Astronomy and Astrophysics Supplement Series, 63, 205. https://ui.adsabs.harvard.edu/abs/1986A&AS...63..205R

Roger, R. S., Costain, C. H., Landecker, T. L., & Swerdlyk, C. M. 1999, Astronomy and Astrophysics Supplement Series, 137, 7, doi: 10.1051/aas:1999239

Schottky, W. 1918, Annalen der Physik, 362, 541, doi: 10.1002/andp.19183622304

Singal, J., Kogut, A., Jones, E., & Dunlap, H. 2015, The Astrophysical Journal, 799, L10, doi: 10.1088/2041-8205/799/1/L10

Singal, J., Stawarz, Ł., Lawrence, A., & Petrosian, V. 2010, Monthly Notices of the Royal Astronomical Society, 409, 1172, doi: 10.1111/j.1365-2966.2010.17382.x

Singal, J., Fixsen, D. J., Kogut, A., et al. 2011, The Astrophysical Journal, 730, 138, doi: 10.1088/0004-637X/730/2/138

Singal, J., Haider, J., Ajello, M., et al. 2018, Publications of the Astronomical Society of the Pacific, 130, 036001, doi: 10.1088/1538-3873/aaa6b0

Singal, J., Fornengo, N., Regis, M., et al. 2023, Publications of the Astronomical Society of the Pacific, 135, 036001, doi: 10.1088/1538-3873/acbdbf

Singh, S., Subrahmanyan, R., Udaya Shankar, N., et al. 2017, The Astrophysical Journal, 845, L12, doi: 10.3847/2041-8213/aa831b

—. 2018, The Astrophysical Journal, 858, 54, doi: 10.3847/1538-4357/aabae1

Singh, S., T., J. N., Subrahmanyan, R., et al. 2021, On the detection of a cosmic dawn signal in the radio background, arXiv. http://arxiv.org/abs/2112.06778

Sklar, B. 2009, Digital communications: fundamentals and applications, 2nd edn. (Upper Saddle River, NJ: Prentice Hall PTR)

Smith, S. W. 1997, The scientist and engineer's guide to digital signal processing, 1st edn. (San Diego, Calif: California Technical Pub)

Sokolowski, M., Tremblay, S. E., Wayth, R. B., et al. 2015, Publications of the Astronomical Society of Australia, 32, e004, doi: 10.1017/pasa.2015.3

Srikanth, S., & Behrens, G. 2007, in 2007 IEEE Antennas and Propagation Society International Symposium, 3684–3687, doi: 10.1109/APS.2007.4396338

Steiger, W. R., & Warwick, J. W. 1961, Journal of Geophysical Research, 66, 57, doi: 10.1029/JZ066i001p00057

Stutzman, W. L., & Thiele, G. A. 1998, Antenna theory and design, 2nd edn. (New York: J. Wiley)

Subrahmanyan, R., & Cowsik, R. 2013, The Astrophysical Journal, 776, 42, doi: 10.1088/0004-637X/776/1/42

Sun, X. H., Reich, W., Waelkens, A., & Enßlin, T. A. 2008, Astronomy and Astrophysics, 477, 573, doi: 10.1051/0004-6361:20078671

Surnis, M. P., Joshi, B. C., McLaughlin, M. A., et al. 2018, Monthly Notices of the Royal Astronomical Society, 478, 4433, doi: 10.1093/mnras/sty1301

Tasse, C., Shimwell, T., Hardcastle, M. J., et al. 2021, Astronomy & Astrophysics, 648, A1, doi: 10.1051/0004-6361/202038804

Tauscher, K., Rapetti, D., & Burns, J. O. 2018a, Journal of Cosmology and Astroparticle Physics, 2018, 015, doi: 10.1088/1475-7516/2018/12/015

—. 2020, The Astrophysical Journal, 897, 175, doi: 10.3847/1538-4357/ab9b2a

Tauscher, K., Rapetti, D., Burns, J. O., & Switzer, E. 2018b, The Astrophysical Journal, 853, 187, doi: 10.3847/1538-4357/aaa41f

Taylor, G. B., Ellingson, S. W., Kassim, N. E., et al. 2012, Journal of Astronomical Instrumentation, 1, 1250004, doi: 10.1142/S2251171712500043

Tello, C., Villela, T., Torres, S., et al. 2013, Astronomy & Astrophysics, 556, A1, doi: 10.1051/0004-6361/20079306

Timoshenko, S. 1983, Strength of materials, 3rd edn. (Malabar, Fla.: Krieger Pub. Co.)

van Bemmel, I. 2007, Ionosperic limits for LOFAR and SKA, doi: 10.22323/1.052.0012

van Haarlem, M. P., Wise, M. W., Gunst, A. W., et al. 2013, Astronomy and Astrophysics, 556, A2, doi: 10.1051/0004-6361/201220873

Vedantham, H. K., Koopmans, L. V. E., de Bruyn, A. G., et al. 2014, Monthly Notices of the Royal Astronomical Society, 437, 1056, doi: 10.1093/mnras/stt1878

Vernstrom, T., Scott, D., Wall, J. V., et al. 2014, Monthly Notices of the Royal Astronomical Society, 440, 2791, doi: 10.1093/mnras/stu470

Voytek, T. C., Natarajan, A., Jáuregui García, J. M., Peterson, J. B., & López-Cruz, O. 2014, The Astrophysical Journal, 782, L9, doi: 10.1088/2041-8205/782/1/L9

West, J. L., Landecker, T. L., Gaensler, B. M., Jaffe, T., & Hill, A. S. 2021, The Astrophysical Journal, 923, 58, doi: 10.3847/1538-4357/ac2ba2

Wouthuysen, S. A. 1952, The Astronomical Journal, 57, 31, doi: 10.1086/106661